

0523

## REPORT DOCUMENTATION PAGE

Public reporting burden for the collection of information is estimated to average 1 hour per response, including the gathering and certifying the data needed, and completing and reviewing the collection of information. Send comments concerning this burden estimate or any other aspect of the collection of information, including suggestions for reducing this burden, to Washington Headquarters Services, One Devil's Highway, Suite 1204, Arlington, VA 22202-4302, and to the Office of Management and Budget, Paperwork Reduction Project 0704-0143.

1. AGENCY USE ONLY (Leave blank)		2. REPORT DATE February 1997	3. REPORT TYPE AND DATES COVERED Final Report Feb. 15, 1994-Feb. 14, 1997
4. TITLE AND SUBTITLE <b>TRANSPORT AND INTERFACIAL KINETICS IN MULTIPHASE COMBUSTION SYSTEMS</b>		5. FUNDING NUMBERS PE - 61102F PR - 2308 SA - BS G - F49620-94-1-0143	
6. AUTHOR(S) Principal Investigator: Daniel E. Rosner		8. PERFORMING ORGANIZATION REPORT NUMBER	
7. PERFORMING ORGANIZATION NAME(S) AND ADDRESS(ES) Yale University High Temperature Chemical Reaction Engineering Laboratory Department of Chemical Engineering PO Box 208286 YS, New Haven, CT 06520-8286 USA		10. SPONSORING/MONITORING AGENCY REPORT NUMBER 19971021 178	
9. SPONSORING/MONITORING AGENCY NAME(S) AND ADDRESS(ES) AFOSR/NA 110 Duncan Avenue, Suite B115 Bolling AFB DC 20332-0001		11. SUPPLEMENTARY NOTES	
12a. DISTRIBUTION/AVAILABILITY STATEMENT Approved for public release; distribution is unlimited		12b. DISTRIBUTION CODE	
13. ABSTRACT (Maximum 200 words)  A 3-year program of research oriented toward the formation/transport of combustion-generated particles is summarized. Using thermophoretic sampling/TEM image analysis techniques, both inorganic (alumina) and carbonaceous soot aggregates have been shown to exhibit quantitatively similar morphologies. A thermophoresis-based method for measuring absolute local soot volume fractions, $f_v$ , in flames has been successfully implemented (in both co-flow and counterflow laminar diffusion flames). Called Thermocouple Particle Densitometry (TPD), it exploits the laws governing thermocouple response to thermophoretic soot deposition, as first suggested by Eisner and Rosner in 1985. This method is independent of (often unknown) soot optical properties, unbiased with respect to soot morphology and size distribution, and yields spatially resolved $f_v$ -values directly even at low soot concentrations (below 0.1 ppm). Accordingly, while neither "instantaneous" or "non-intrusive", it is especially applicable to spatially non-uniform and/or lightly sooting laminar steady flames. Ancillary studies of the transport properties of soot aggregates, and particle impaction on cylinders in high-speed crossflow are also described/document among the 30 cited references emerging from this program(Section 5).			
14. SUBJECT TERMS Soot morphology, aggregated particles, particle mass transport, thermophoresis, sintering, Brownian diffusion, chemical vapor deposition, particle sampling, nano-particle formation/restructuring in flames, deposition rate theory		15. NUMBER OF PAGES 38	
16. PRICE CODE			
17. SECURITY CLASSIFICATION OF REPORT Unclassified	18. SECURITY CLASSIFICATION OF THIS PAGE Unclassified	19. SECURITY CLASSIFICATION OF ABSTRACT Unclassified	20. LIMITATION OF ABSTRACT UL

# TRANSPORT AND INTERFACIAL KINETICS IN MULTIPHASE COMBUSTION SYSTEMS

Principal Investigator: Prof. Daniel E. Rosner

## 1. INTRODUCTION

The performance of aircraft gas turbine engines under sooting conditions and/or ramjets burning slurry fuels (leading to oxide aerosols and deposits), depends upon the formation and transport of small particles of complex morphology, often in non-isothermal combustion gas boundary layers (BLs). Aggregate formation / transport are also important in chemical reactors used to synthesize/process aerospace materials, including turbine blade coatings, optical waveguides, ceramic precursor powders,...). Accordingly, this 3 year research program was directed toward providing chemical propulsion system engineers with rational new predictive techniques to deal with particle formation-transport-deposition phenomena, accounting for significant non-spherical particle morphology effects. An interactive experimental/theoretical approach has been used to gain an understanding of performance-limiting mass/energy transfer-phenomena at or near interfaces. This included the development and exploitation of laboratory diffusion flame burners and new (thermophoresis-based) soot diagnostic/characterization techniques (Sections 2,5). Resulting experimental data, together with the predictions of asymptotic theories, were used to propose and verify *rational engineering correlations* for future design/optimization.

## 2. RESEARCH ACCOMPLISHMENTS

The most important results obtained under Grant AFOSR F49620-94-1-0143 during the period: **Feb. 15, 1994-Feb. 14, 1997** can be broadly divided into the subsections below. Since our techniques and results are so thoroughly documented in our archival publications (Section 5) and previous Annual Reports, this Final Report provides only a brief overview.

### 2.1. SEEDED LAMINAR COUNTERFLOW DIFFUSION FLAME EXPERIMENTS: FORMATION, COAGULATION, TRANSPORT AND STABILITY OF COMBUSTION-GENERATED PARTICLES

Particles produced during combustion processes frequently become aggregates of much smaller "primary" spherules, partially 'fused' due to high temperatures. Consequently, the resulting aggregates can differ in morphology and size according to the flame conditions under which they are generated and 'processed'. Since particle morphology and aggregate transport properties are interrelated (Tandon and Rosner, 1996), it is important to understand not only aggregate formation but also their *morphological evolution* in flames. We have carried out experimental investigations of the morphological evolution of flame-generated aggregates at low particle volume fractions ( $O(10^{-1}$  ppm)) in a well-defined/characterized laminar non-premixed combustion environment.  $\text{Al}_2\text{O}_3$  particles synthesized in a  $\text{Al}(\text{CH}_3)_3$  (TMA)-seeded atmospheric pressure laminar counterflow diffusion flame fueled with  $\text{CH}_4/\text{O}_2/\text{N}_2$  are used as the model material/combustion system (Xing, *et.al.*, 1996). Experiments include laser light scattering (LLS) and thermophoretic sampling/Transmission Electron Microscope (TEM) techniques (Koylu, *et.al.*, 1995). Aggregate morphology was characterized in terms of spherule ("grain") size, aggregate size, aggregate shape and fractal structure. Additionally, the effects of temperature and TMA concentration on particle sizes and morphology were also investigated systematically and interpreted based on parallel theoretical studies. LLS signals and typical TEM images clearly illustrated particle/aggregate size and morphology evolution as a result of two competing processes, with *coagulation* increasing aggregate sizes, and *sintering* reducing aggregate surface areas. Mean spherule diameters were found to be in the range of only 13 to 40 nm, increasing with increasing temperature and with TMA concentration. Mean aggregate sizes reached a maximum near a local temperature of only 1250 K and increased with TMA seed level. Perhaps most interesting, the final products were compact spherical particles resulting from complete 'collapse' of the aggregates, apparently as a result of surface diffusion rather than surface energy-driven "viscous flow". These results were shown to be compatible with the characteristic times governing each of the participating "unit" rate processes (Xing, *et.al.*, 1996). More comprehensive quantitative predictions are

underway for multi-phase laminar CDFs and will be part of our follow-on AFOSR research program. The experimental and theoretical methods developed and illustrated here will find applications in controlling the synthesis of valuable nano-powders, and facilitate rational extensions into the domain of *turbulent* non-premixed combustors generating desired or inadvertent ultrafine particles.

## 2.2 IMPLEMENTATION OF THERMOCOUPLE PARTICLE DENSITOMETRY (TPD)

Thermocouple Particle Densitometry (TPD) is a convenient, inexpensive and robust method for measuring absolute and local soot volume fractions,  $f_v$ , in flames first suggested by Eisner and Rosner in 1985. Based on the laws governing thermocouple response to *thermophoretic soot deposition*, this method has now been successfully implemented in both axisymmetric co-flowing laminar diffusion flames as well as CDFs (McEnally *et.al.*, 1997). Since it yields spatially resolved  $f_v$ -values directly and can easily measure low soot concentrations, TPD is especially applicable to spatially non-uniform and/or lightly sooting flames. To further evaluate the method, TPD soot volume fractions (ppm) were recently measured in several laminar non-pre-mixed flames. In methane and ethylene counterflow flames the TPD results agreed to within experimental error with laser extinction measurements we performed in the same flames. In axisymmetric methane and ethylene co-flowing flames the shape of TPD  $f_v$  profiles also agreed well with published de-convoluted laser extinction measurements in similar flames. However, soot volume fractions inferred from mass deposition were systematically somewhat larger than laser *extinction* results in the lower portion of an ethylene co-flowing diffusion flame, and throughout a methane co-flowing flame, probably due to deposition of visible-light-transparent particles with masses of several thousand amu, known to be present in such flames. This implies that TPD could prove useful in future studies of the significance of these "invisible" soot precursors.

## 2.3 MORPHOLOGY OF FLAME-GENERATED 'SOOT' AGGREGATES

We have developed/tested/exploited practical image-analysis methods for inferring the fractal characteristics of thermophoretically sampled aggregates based on their projected (2-D) images (Koylu *et.al.*, 1995).

Based on our investigation of over 3000 electron microscope images of soot aggregates from a variety of laminar and turbulent *hydrocarbon*-fueled flames we have found (Neimark *et.al.*(1996)) that their scaling properties *cannot* be characterized solely using the now-familiar *mass fractal dimension*,  $D_f$ . Rather, the *asymmetric* properties of flame-generated soot evidently require the introduction of *longitudinal* ( $[(1+H)/2] \cdot D_f$ ) and *transverse* ( $[(1+H)/2H] \cdot D_f$ ) exponents, where  $D_f=1.75$  and  $H=0.91$ . In this sense combustion-generated soot aggregates should apparently be regarded as *self-affine* rather than self-similar. Moreover, widely employed diffusion-limited cluster-cluster aggregation (DLCCA-) models, while undeniably providing a useful first approximation, are unable to accurately describe these aggregate populations not only with respect to  $H \neq 1$  but also with respect to lacunarity (pre-exponential factor; see Koylu *et.al.*(1995)). This statistically significant asymmetry may prove to be important for predicting essential *transport and radiative properties* of suspended aggregates.

## 2.4 THEORY OF TRANSPORT, RESTRUCTURING, AND RADIATIVE TRANSPORT PROPERTIES OF FLAME-GENERATED AGGREGATES

The ability to reliably predict transport properties and morphological stability of *aggregated* flame-generated *particles* (carbonaceous soot,  $\text{Al}_2\text{O}_3$ ,  $\text{SiO}_2$ ,...) is important in chemical propulsion and refractory materials fabrication applications. We have developed efficient methods to anticipate coagulation, restructuring, and ultimate deposition rates of suspended populations of such particles in combustion systems, as well as laws needed to interpret laser-based soot diagnostics. In one asymptotic limit large 'fractal' aggregates are treated using a spatially variable, effective porosity pseudo-continuum model (see, *e.g.*, Rosner and Tandon (1994) and Tandon and Rosner(1996)). Indeed, the competition between restructuring kinetics and coagulation kinetics determines the observed size of the apparent "primary" particles comprising soot particles (Xing and Rosner, 1996), as well as the "collapse" of surface area observed in some high temperature systems. These studies, together with our methods to predict interactions between aggregates and their surrounding *vapor* environment (interactions which can lead to

primary particle growth, or (for carbonaceous soot in the presence of oxidizing species burn-out) are now available to be incorporated into our laminar CDF structure modelling (Xing et.al.,1997). This work will also facilitate rational extensions into the uncharted domain of turbulent non-premixed combustors generating ultrafine particles, via extended flamelet models.

## 2.5 PARTICLE FORMATION AND TRANSPORT IN LAMINAR BOUNDARY LAYERS AND MIXING LAYERS

Because of the implications for depositing thin solid films (Rosner, Collins,1994) and soot layers we also investigated particle formation in laminar boundary layers and deposition near hot solid surfaces, leading to 'mixed' particle plus vapor deposition ("co-deposition", see Tandon and Rosner, 1996; Castillo and Rosner, 1996). These phenomena also occur when fuel-rich vapors 'impinge' on hot solid surfaces, as in gas turbine combustors. We have developed a promising rational approach to predict the self-consistent *deposit roughness* as well as deposition rate in such circumstances (Tandon and Rosner (1996).

## 2.6 PARTICLE IMPACTION ON CYLINDRICAL TARGETS; EROSION BEHAVIOR OF CERAMIC OR METAL TARGETS IN HIGH-SPEED ABRASIVE STREAMS

We have exploited our earlier correlations for *inertial impaction* using an *effective Stokes number* to calculate: a) particle deposition rates on cylindrical targets, including *rebound* behavior (Rosner and Tandon, 1995a) and b) the relation between the particle size distribution of *deposited* particles and the particle size distribution of the *mainstream* suspension (Rosner and Tandon, 1995b)

By capturing with simple formulae the essential features of available *erosion yield* experiments, we have developed an efficient method to predict local and total surface *erosion rates* for metal or ceramic targets of simple geometry exposed to a 'polydispersed' population of abrasive particles suspended in a high-speed mainstream (Rosner et.al. (1995), Kho et.al. (1995), Khalil and Rosner(1996)). Our earliest methods/results (*loc. cit.*) were deliberately limited to small relative changes in body shape to allow for arbitrary Stokes numbers. We then relaxed this assumption for the limiting (worst-) case of rectilinear erodent particle trajectories. The interface was assumed to recede normal to itself at the rate determined by the local particle impaction frequency, angle-of-incidence and velocity (Rosner and Khalil (1996)). The normalized "body" radius  $R(\theta, \tau)$  at polar angle  $\theta$ , and dimensionless exposure time  $\tau$  was found to satisfy an interesting first-order nonlinear PDE. Illustrative results were obtained comparing the erosion rate behavior of initially circular targets of a *ceramic* and a *metal* by numerically solving this PDE using the "method of lines". Calculated interface positions revealed "nose blunting" for the erosion of *ceramic* targets in a uniform erodent-carrying stream. In contrast, "nose-sharpening" occurred for *metal* targets, with the development of an ogive-shaped feature facing upstream. Our methods can be used to calculate/correlate the erosion behavior of targets of other important aerodynamic shapes, including spheres, cones,..... These methods/results will allow aerospace design engineers to anticipate erosion behavior in a variety of particle-laden flow environments, and provide guidance on tolerable particle loadings, required maintainence frequencies, and materials selection.

## 3. ADMINISTRATIVE INFORMATION: PERSONNEL, PRESENTATIONS, APPLICATIONS, TECHNOLOGY TRANSFER

The following sections summarize some pertinent facets of the abovementioned Yale HTCRE Lab/AFOSR three year research program of management interest:

### 3.1 Research Personnel

Our present results (Sections 2 and 5) are due to the contributions of the individuals listed in Table 3.1-1, which also indicates the role of each researcher. It will be noted that, in addition to the results themselves, this program has simultaneously contributed to the research training of my PhD students J. Collins, P. Tandon, and Y. Xing, who are now be in an excellent position to make future contributions to technologies oriented toward air-breathing chemical propulsion, and/or high-tech aerospace materials processing.

Table 3.1-1 Summary of *Research Participants<sup>a</sup>* on AFOSR Grant: F49620-94-1-0143:

**TRANSPORT PHENOMENA AND INTERFACIAL KINETICS  
IN MULTIPHASE COMBUSTION SYSTEMS**

Name	Status <sup>a</sup>	Principal Research Activity <sup>b</sup>
Castillo, J.L.	Res. Vis.	x-port props. of aggregates
Collins, J.	PDRA	chemical vapor deposition
Farias, T.	Res. Vis.	radiative props. of aggregated soot
Garcia-Ybarra, P.	Res. Vis.	x-port props. of aggregates
Khalil, Y.F.	Res. Assoc.	erosion of ceramics
Kho, T.	GRA(MS)	CV-Deposit density correlation
Konstandopoulos, A.G.	Res. Vis.	deposition rate theory
Koylu, U.O.	PDRA	thermophoretic sampling/image analysis
McEnally, C.	PDRA	thermophoresis-based soot diagnostics
Neimark, A. V.	Vis. Fac.	fractal morphology of aggregates
Rosner, D.E.	PI	program direction-dep. theory/exp
Tandon, P.	GRA,PDRA	x-port props. of aggregates
Xing, Y.	GRA	particle prod/char. in CDFs
Vaidya, D.	PDRA	simultaneous coag. + restructuring

<sup>a</sup> PDRA=Post-doctoral Research Asst  
PI = Principal Investigator

GRA= Graduate Research Assistant (PhD unless designated MS)  
<sup>b</sup> See Section 5 for specific references cited in text (Section 2)

### 3.2 Cooperation with US Industry

While the research summarized here was supported by AFOSR under Grant AFOSR 94-1-0143, the Yale HTCRE Laboratory has also been the beneficiary of continuing smaller grants from U.S. industrial corporations, including groups within ALCOA, GE, DuPont, Union Carbide (now Advanced Ceramics Corp.) and Shell, as well as the feedback and occasional advice of principal scientists/engineers from each of these corporations and Combustion Engineering-ABB and Textron. We appreciate this level of collaboration, and expect that it will accelerate inevitable applications of our results in areas relevant to their technological objectives (see, also, Section 3.4, below).

Periodically our results are picked up and used by aerospace industrial contractors. As mentioned below and included in my September 1996 report as a formal "Technology Transition", a variant of our recent method to correlate/predict the density of vapor deposited graphite, BN,...(Kho,*et.al.*,1995, Section 5.1) is being used by Advanced Ceramics Corp. (M. B. Dowell, *et.al.*) to guide the selection of production conditions in their CVD reactors. Another such transition based on the PhD research of J. Collins, 1995 is also taking shape and will be reported in due course.

### 3.3 External Presentations, Research Training

Apart from the *ca.* 24 publications itemized in Section 5.1, and the 5 submitted papers now in print (Section 5.2) verbal accounts of our research on soot diagnostic techniques, soot morphology and transport, particle and vapor deposition dynamics, and erosion were presented on some 32 occasions over this reporting period, including invited presentations at the US Corporations: DuPont, ALCOA, and PPG, and at each of the annual AIChE, AAAR and MRS meetings. As noted below, the present 3 year AFOSR program has also led to some 120 citations under the PI's name: Rosner, D.E. in *Science Citation Index*.

This research program also involved completion of the PhD dissertation research of Joshua Collins and Pushkar Tandon, and will be the basis of the PhD dissertation of Yangchuan Xing, expected to defend his work in September of this year.

### **3.4 Applications of Yale-HTCRE Lab Research Results, Including Technology Transfer**

It has been gratifying to see direct applications of some of this generic AFOSR-supported particle and vapor mass transfer research in more applications-oriented investigations reported in recent years. Indeed, *the writer would appreciate it if further examples known to the reader can be brought to his attention*. As a result of the present 3 year AFOSR program, over one hundred citations under the PI's name: Rosner, D.E. have appeared in *Science Citation Index*.

We communicated a Sept. 1996 *Technology Transition* which was a variant of our recent method to correlate/predict the density of vapor deposited graphite, BN,...(Kho,*et.al.*,1995). This correlation is being used by Advanced Ceramics Corp. (M. B. Dowell, *et.al.*) to guide their selection of CVD reactor operating conditions. It should also be applicable in the field of diamond film deposition.

While the work described in McEnally *et.al.*, 1997, has the potential of leading to a thermocouple-based instrument/software package for determining local soot volume fractions and temperatures in laminar flames (based on the laws of soot particle thermophoresis, completely independent of particle optical properties, and applicable to very low soot volume fractions), we have no immediate plans to pursue the patent/licencing implications. Our most recent demonstration that thermophoretic theory combined with TEM-grid information can provide local soot volume fractions as well as all required morphological information (Koylu *et. al.*, 1997; Section 5.2), is expected to have a significant influence on soot research worldwide, especially since the optical properties of "young" soot are poorly known.

Of course, in combustion fundamentals research, many groups (*e.g.*, Dobbins *et.al.* (Brown U.), Faeth *et.al.* (U. Mich.), Katz *et al.* (J. Hopkins U.)) are now utilizing "thermophoretic sampling" techniques to exploit the size- and morphology-insensitive capture efficiency characteristics proven in our AFOSR research (Sections 2.1, 2.3). Our earlier thermophoretic studies (*e.g.*, Gomez and Rosner, 1993) have also led to an appreciation of the associated systematic corrections needed in particle velocimetry, as well as the important role that particle stagnation plane location plays in powder synthesis flames.

Our AFOSR-supported research on *soot deposition rates* from flowing laminar or turbulent combustion gases is now also the basis of a collaborative AGARD-NATO supported program with IST-Lisbon (Profs. M. G. Carvalho, T. Farias), and was applied earlier by Aerojet Corp. to develop (NASA support) a model for application to rocket chambers and nozzles. Extensions to jet engine nozzles have been made by M.T. Nys at Pratt & Whitney Engine Business in W. Palm Beach FL. Applications of our AFOSR and DOE-supported research (on the correlation of inertial impaction by cylinders in crossflow) recently made by the National Engineering Laboratory (NEL) of Glasgow and somewhat similar to those reported earlier by the Combustion R&D groups at MIT, Sandia-Livermore CRF and Penn State U, are now being taken up by VTT-Energy/Aerosol Technology Group, in Finland.

For calculating suspended particle concentrations along trajectories outside of aircraft (involved in atmospheric sampling), or inside of CVD reactors, A. S. Geller and D. J. Rader of Sandia-Albuquerque have adopted a method developed in our earlier AFOSR work (Fernandez de la Mora, 1981), and recently applied in our own studies of particle motion in laminar boundary layers with streamwise curvature (Konstandopoulos and Rosner, 1995). Some of this work may also be useful in future sampling studies of condensation nuclei emerging from stratospheric aircraft.

Earlier work at MIT, PSI and Sandia CRF had incorporated our rational correlation of *inertial particle impaction* (*e.g.* a cylinder in cross-flow) in terms of our *effective Stokes number* (see, *e.g.* Rosner and Tandon, 1995a,b). Now our correlations of deposition by simultaneous thermophoresis and inertia are being used in the interpretation of heat exchanger fouling data in Grenoble, France.

In the area of multicomponent *vapor* deposition in combustion systems our discussion in the 26th *Comb. Symposium* of the paper of Steinberg and Schofield (Re: alkali salt deposition experiments) cites our earlier relevant work and may lead to future extensions. Another of our discussions in the 26th *Comb. Symposium* pertains to the potentially important role of temperature "jump" phenomena (see, *eg.*, Rosner and Papadopoulos, 1996) in the CARS temperature experiments of Bertagnolli and Lucht on the growth of diamond films using combustion techniques.

Fruitful *opportunities* for the further application of our recent research on the morphology/transport properties of combustion-generated particles and "non-Brownian" convective mass transfer for particles and vapors now exist in many of the programs currently supported by the US Air Force, as well as civilian sector R&D. This includes mass transfer and fouling aspects of fuel-coolant breakdown upstream of high pressure aircraft gas turbine combustors.

#### 4. CONCLUSIONS

The ability to reliably predict the transport properties and stability of *aggregated* flame-generated *particles* (carbonaceous soot,  $B_2O_3$ ,  $Al_2O_3$ , ...)<sup>†</sup> is important for many technologies relevant to the U.S.A.F., especially jet engine and ramjet combustor design. Indeed, realistic soot morphology is not yet even a part of chemically complex sooting *laminar* flame models, and the computational methods used to include coagulation dynamics (*e.g.*, "moment" or "sectional" finite-difference) methods do not lend themselves to this next step. Also, some properties needed to correctly interpret the results of recently introduced laser diagnostics applied in research on soot formation/suppression (*e.g.*, laser-induced incandescence (LII)) are not yet available. In this AFOSR program (94-1-0143) considerable experimental and theoretical progress along these lines has been made (Section 2) and reported (Section 5). These experimental techniques, together with closely coupled theoretical calculations of particle birth/dynamics in counterflow diffusion flames and mixing/boundary layers, are leading to a valuable understanding of combustion-generated ultra-fine particles, including their evolution/deposition dynamics in turbulent high pressure systems.

<sup>†</sup>Finely divided boron- and aluminum-based fuel additives for performance enhancement lead to non-carbonaceous "soots" in many air-breathing and rocket combustor situations. Moreover, trace inorganics in petroleum-based fuels, or in the air breathed for combustion likewise lead to submicron inorganic aerosols affecting system performance, including jet-engine contrail formation in the stratosphere. In this AFOSR program we have shown that soot aggregates from a wide variety of organic and inorganic combustion systems exhibit interesting and mechanistically significant morphological similarities (Rosner, 1996, Koylu *et.al.*, 1995, Xing *et.al.*, 1996)

#### 5. REFERENCES

##### 5.1 PUBLICATIONS WHICH APPEARED\* BASED ON GRANT AFOSR 94-1-0143

- Castillo, J.L. and Rosner, D.E., "Role of High Activation Energy Homogeneous Chemical Reactions in Affecting CVD Rates and Deposit Quality for Heated Surfaces", *Chemical Engineering Sci.* **51** (24) 5325-5340 (1996)
- Collins, J., **Effects of Homogeneous Reaction on the Chemical Vapor Deposition of Titanium Dioxide**, PhD Dissertation, Yale University-Graduate School, Dept. Chemical Engineering, 1994
- Farias, T.L., Koylu, U.O., and Carvalho, M.G., "Effects of Polydispersity of Aggregates and Primary Particles on Radiative Properties of Simulated Soot", *J. Quant. Spectros. Radiat. Transfer* **55** (3) 357-371 (1996)
- Gokoglu, S.A., Stewart, G.D., Collins, J., and Rosner, D.E., "Numerical Analysis of an Impinging Jet Reactor for the CVD and Gas Phase Nucleation of Titania", *Mat. Res. Sympos. Proc.* Vol. **335**, 171-176 (1994)
- Khalil, Y. F. and Rosner, D.E., "Erosion Rate Prediction and Correlation Technique for Ceramic Surfaces Exposed to High-Speed Flows of Abrasive Suspensions", *WEAR* **201**, 64-79 (1996)

\*Reproduced (with Form 298) in Section 6; all other archival papers have been included in our previous Annual Reports on this Grant.

- Kho, T., Collins, J. and Rosner, D. E., "Development, Preliminary Testing, and Future Applications of a Rational Correlation for the Grain Densities of Vapor-Deposited Materials" *J. Materials Sci.*, **30** 3440-3448 (1995)
- Konstandopoulos, A.G. and Rosner, D.E., "Inertial Effects on Thermophoretic Transport of Small Particles to Walls With Streamwise Curvature---I. Theory, *Int. J. Heat Mass Transfer* (Pergamon) **38** (12) 2305-2315 (1995)
- Konstandopoulos, A.G. and Rosner, D.E., "Inertial Effects on Thermophoretic Transport of Small Particles to Walls With Streamwise Curvature---II. Experiment, *Int. J. Heat Mass Transfer* (Pergamon) **38** (12) 2317-2327 (1995)
- Koylu, U.O. and Faeth, G.M., "Spectral Extinction Coefficients of Soot Aggregates From Turbulent Diffusion Flames", *J. Heat Transfer* (ASME) **118** (5) 415-421 (1996)
- Koylu, U.O., Xing, Y., and Rosner, D.E., "Fractal Morphology Analysis of Combustion-Generated Aggregates Using Angular Light Scattering and Electron Microscope Images", *Langmuir* (Amer. Chem. Soc.) **11** (12) 4848-4854 (1995)
- Koylu, U. O., "Quantitative Analysis of *In-situ* Optical Diagnostics for Inferring Particle/Aggregate Parameters in Flames: Implications for Soot Surface Growth and Total Emissivity", *Comb & Flame* **109**, 488-500 (1996)
- Mackowski, D.W., Tassopoulos, M. and Rosner, D.E., "Effect of Radiative Heat Transfer on the Coagulation Dynamics of Combustion-Generated Particles", *Aerosol Sci. Technol. (AAAR)* **20** (1) 83-99, (1994))
- Neimark, A.V., Koylu, U. O., and Rosner, D.E., "Extended Characterization of Combustion-Generated Aggregates: Self-Affinity and Lacunarity", *J. Colloid Int. Sci.*, **180**, 590-597(1996) ¶
- Rosner, D.E. and Tandon, P., "Prediction and Correlation of 'Accessible' Area of Large Multi-particle Aggregates ", *AIChE J.* **40** (7), 1167-1182 (1994)
- Rosner, D.E., Tandon, P. and Konstandopoulos, A.G., "Rational Prediction of Inertially Induced Particle Deposition Rates for a Cylindrical Target in Dust-Laden Streams", *Proc. 1st Int. Particle Technology Forum*, AIChE , Vol. II, 374-381 (1994).
- Rosner, D. E., Tandon, P. , and Labowsky, M.J. , "Rapid Estimation of Cylinder Erosion Rates in Abrasive Dust-Laden Streams: Effects of Erosion Rate Law and Dust Polydispersity on Predicted Local and Total Target Wear", *AIChE J.*,**41**(5) 1081-1098 (1995 )
- Rosner, D.E., Khalil, Y.F. and Tandon, P., "Prediction/Correlation of Erosion Rates and Shape Evolution for Ceramic Surfaces Exposed to Flows of Abrasive Suspensions", *Proc. Fifth World Congress of Chemical Engineering*, AIChE, San Diego,CA, July 14-18, 1996 Paper #112e , Vol. IV, 1013-1018 (1996)
- Rosner, D.E. and Tandon, P., "Rational Prediction of Inertially Induced Particle *Deposition* Rates for a Cylindrical Target in a Dust-Laden Stream" *Chem Eng. Sci.* **50** (21) 3409-3431(1995a)
- Rosner, D. E., Tandon, A.G., and Konstandopoulos, A.G., "Local Size Distributions of Particles Deposited by Inertial Impaction on a Cylindrical Target in Dust-Laden Streams", *J. Aerosol Sci.*,(Pergamon) **26** (8) 1257-1279 (1995b)
- Rosner, D.E. and Papadopoulos, D., "Jump, Slip and Creep Boundary Conditions at Nonequilibrium Gas/Solid Interfaces", *Ind Eng Chem-Res (ACS)* **35**(9) 3210-3222 (1996) ¶
- Tandon, P., and Rosner, D. E., "Translational Brownian Diffusion Coefficient of Large (Multi-Particle) Suspended Aggregates", *Ind Eng Chem-Res (ACS)* **34** 3265-3277(1995)
- Tandon, P., and Rosner, D. E., "Co-deposition on Hot CVD Surfaces: Particle Dynamics and Deposit Roughness Interactions", *AIChE J.* **42** (6) 1673-1684 (1996)
- Tandon P., Transport Theory for Particles Generated in Combustion Environments**, PhD Dissertation, Yale University-Graduate School, Dept. Chemical Engineering, May 1995
- Xing, Y., Köylü Ü. Ö., Tandon P. and Rosner D. E., "Measuring and Modeling the Synthesis and Morphological Evolution of Particles in Counterflow Diffusion Flames", *Proc. Fifth World Congress of Chemical Engineering*, AIChE, San Diego, CA, July 14-18, 1996 Paper #88d, Vol. V, pp 43-48.

Reproduced (with Form 298) in Section 6

Xing, Y., and Rosner, D.E., "Surface Melting of Particles: Predicting Spherule Size in Vapor-Phase Nanometer Particle Formation", Paper#V5.36, MRS Fall 1996 Meeting, Dec. 4, 1996, Boston MA

Xing, Y., Köylü Ü. Ö., and Rosner D. E., "Synthesis and Restructuring of Inorganic Nano-particles in Counterflow Diffusion Flames", *Comb & Flame* **107** 85-102(1996)¶

## 5.2 PAPERS SUBMITTED BASED ON GRANT AFOSR 94-1-0143

Koylu, U.O., McEnally, C.S., Rosner, D.E and Pfefferle, L.D., "Simultaneous Measurements of Soot Volume Fraction and Particle Size/Microstructure in Flames Using a Thermophoretic Sampling Technique", *Comb & Flame* **110** 494-507(1997)

McEnally, C.S., Koylu, U.O., Pfefferle, L.D. and Rosner, D.E., "Soot Volume Fraction and Temperature Measurements in Laminar Non-Premixed Flames Using Thermocouples", *Comb & Flame* **109** 701-720(1997)

Rosner, D.E., "Combustion Synthesis and Materials Processing", *Chemical Engineering Education* (ASEE), Fall 1997 Graduate Issue (ca. November 1997)

Tandon, P., and Rosner, D.E., "Monte-Carlo Simulation of Simultaneous Fractal Particle Aggregation and Restructuring", *J Colloid Interface Sci.* (in press, 1997)

Xing, Y., Rosner, D.E., Koylu, U.O. and Tandon, P., "Morphological Evolution of Oxide Nano-particles in Laminar Counterflow Diffusion Flames--Measurements and Modelling", *AICHE J.* (Special Issue on Ceramics Processing)(in press, Fall 1997); AICHE '97 Mtg., Invited Lecture (Nov. 1997)

\*\*\*\*\*

## LIST OF ABBREVIATIONS

ALS	Angular Light Scattering	BL	Boundary layer
CDF	Counterflow diffusion flame	TEM	Transmission Electron Microscopy
CVD	Chemical vapor deposition	CRF	Combustion Research Facility
CSL	Chemical sublayer	CFD	Computational Fluid Dynamics
D <sub>f</sub>	Fractal dimension	GRA	Graduate research Asst.
G/S	Gas/solid interface	IJHMT	<i>Int. J. Heat/Mass Xfer</i>
LDV	Laser Doppler Velocimetry	LII	Laser-induced incandescence
LLS	Laser light scattering	LTCE	local thermochemequilibrium
PBE	Population Balance Eq.	pdf	Probability density function
PI	Principal Investigator	PSD	Particle size distribution
MRS	Materials Research Society	TMA	Trimethyl aluminum
VS	Visiting Scholar	TPD	Thermocouple Particle Densitometry

## 6. APPENDICES (Complete Papers Published During Period: 2/15/94 -2/14/97 on GRANT AFOSR 94-1-0143; including Form 298 for each)

\*\*\*\*\*

PIADC INFO (cf. Sections 5.1, 6) to follow:

**PIADC INFO (cf. Sections 5.1, 6):**

Name of Journal: *Comb & Flame*

Title of Article: "Synthesis and Restructuring of Inorganic Nano-particles in Counterflow Diffusion Flames"

Authors: Xing, Y., Koylu, U. O., and Rosner, D.E.

Publisher: Combustion Inst. (Pittsburgh PA)

Volume: **107**      Pages: 85-102      Month Published:      Year: (1996)

---

Name of Journal: *Ind. Engrg. Chem- Research*

Title of Article: "Jump, Slip and Creep Boundary Conditions at Non-equilibrium Gas/ Solid Interfaces"

Authors: Rosner, D.E. and Papadopoulos, D.

Publisher: Amer. Chem Soc.

Volume: **35**      Pages: 3210-3222      Month Published: September      Year: (1996)

---

Name of Journal: *WEAR*

Title of Article: "Erosion Rate Prediction and Correlation Technique for Ceramic Surfaces Exposed to High-Speed Flows of Abrasive Suspensions"

Authors: Khalil, Y.F. and Rosner, D.E.

Publisher: Elsevier

Volume: **201**      Pages: 64-79      Month Published:      Year: (1996)

---

# REPORT DOCUMENTATION PAGE

Form Approved  
OMB No. 0704-0188

Public reporting burden for this collection of information is estimated to average 1 hour per response, including the time for reviewing instructions, searching existing data sources, gathering and maintaining the data needed, and completing and reviewing the collection of information. Send comments regarding this burden estimate or any other aspect of this collection of information, including suggestions for reducing this burden, to Washington Headquarters Services, Directorate for Information Operations and Analysis, 1215 Jefferson Davis Highway, Suite 1204, Arlington, VA 22202-4302, and to the Office of Management and Budget, Paperwork Reduction Project (0704-0188) Washington, DC 20503.

1. AGENCY USE ONLY (Leave blank)	2. REPORT DATE	3. REPORT TYPE AND DATES COVERED	
	1996	Reprint	
4. TITLE AND SUBTITLE <i>v</i>  Synthesis and Restructuring of Inorganic Nano-Particles in Counterflow Diffusion Flames			5. FUNDING NUMBERS
			PE - 61102F PR - 2308 SA - BS G - F49620-94-1-0143
6. AUTHOR(S)  YANGCHUAN XING, ÜMIT Ö. KÖYLÜ,* and DANIEL E. ROSNER			8. PERFORMING ORGANIZATION REPORT NUMBER
7. PERFORMING ORGANIZATION NAME(S) AND ADDRESS(ES)  Yale University High Temperature Chemical Reaction Engineering Laboratory Department of Chemical Engineering PO Box 208286 YS, New Haven, CT 06520-8286 USA			
9. SPONSORING/MONITORING AGENCY NAME(S) AND ADDRESS(ES)  AFOSR/NA 110 Duncan Avenue, Suite B115 Bolling AFB DC 20332-0001			10. SPONSORING/MONITORING AGENCY REPORT NUMBER
11. SUPPLEMENTARY NOTES  COMBUSTION AND FLAME 107: 85-102 (1996) Copyright © 1996 by The Combustion Institute Published by Elsevier Science Inc.			
12a. DISTRIBUTION/AVAILABILITY STATEMENT  Approved for public release; distribution is unlimited		12b. DISTRIBUTION CODE	
13. ABSTRACT (Maximum 200 words)  The formation/growth/coagulation/sintering of flame-generated inorganic aggregates at low particle volume fractions ( $O(10^{-1}$ ppm)) was investigated. $Al_2O_3$ particles synthesized in a $Al(CH_3)_3$ (TMA)-seeded atmospheric pressure counterflow diffusion flame (CDF) fueled with $CH_4/O_2/N_2$ were used as the model material/combustion system. Experimental techniques included thermocouple, laser light scattering (LLS) and thermophoretic sampling/Transmission Electron Microscopy (TEM). Local aggregate morphology evolution was characterized in terms of "primary" particle size, aggregate size, and fractal structure. Additionally, the effects of temperature and TMA concentrations on morphology and size were also investigated systematically in the CDF. Light scattering signals as well as TEM analysis clearly illustrated particle/aggregate size and morphology evolution as a result of two competing processes, with coagulation increasing aggregate sizes, and sintering reducing aggregate surface areas. Mean "primary" particle diameters were found to be in the range of 13-47 nm, increasing with TMA concentration and sampling position (increasing residence time). On the other hand, mean aggregate sizes reached a maximum at about 4 mm above the bottom fuel duct (corresponding to a local temperature of only 1250 K) and increased with TMA seed level. Fractal dimension and fractal prefactor of alumina aggregates with negligible sintering rates were found to be 1.52 and 2.4, respectively. The final products were larger spherical particles with up to 60 nm diameter, resulting from complete "collapse" of the aggregates. These observations were shown to be compatible with our independent evaluation of the characteristic times associated with the participating rate processes in this class of two-phase CDFs. Systematic modification of these characteristic times can be used to control the size and morphology of flame-synthesized particles.			
14. SUBJECT TERMS  nano-particle synthesis, sintering, thermophoretic particle sampling, nano-particle formation/restructuring in flames, Brownian coagulation of aggregates			15. NUMBER OF PAGES 18
			16. PRICE CODE
17. SECURITY CLASSIFICATION OF REPORT Unclassified	18. SECURITY CLASSIFICATION OF THIS PAGE Unclassified	19. SECURITY CLASSIFICATION OF ABSTRACT Unclassified	20. LIMITATION OF ABSTRACT UL

# Synthesis and Restructuring of Inorganic Nano-Particles in Counterflow Diffusion Flames

YANGCHUAN XING, ÜMIT Ö. KÖYLÜ,\* and DANIEL E. ROSNER  
Yale Center for Combustion Studies, Department of Chemical Engineering, Yale University, New Haven,  
CT 06520-8286

The formation/growth/coagulation/sintering of flame-generated inorganic aggregates at low particle volume fractions ( $O(10^{-4}$  ppm)) was investigated.  $Al_2O_3$  particles synthesized in a  $Al(CH_3)_3$ -seeded atmospheric pressure counterflow diffusion flame (CDF) fueled with  $CH_4/O_2/N_2$  were used as the model material/combustion system. Experimental techniques included thermocouple, laser light scattering (LLS) and thermophoretic sampling/Transmission Electron Microscopy (TEM). Local aggregate morphology evolution was characterized in terms of "primary" particle size, aggregate size, and fractal structure. Additionally, the effects of temperature and TMA concentrations on morphology and size were also investigated systematically in the CDF. Light scattering signals as well as TEM analysis clearly illustrated particle/aggregate size and morphology evolution as a result of two competing processes, with coagulation increasing aggregate sizes, and sintering reducing aggregate surface areas. Mean "primary" particle diameters were found to be in the range of 13–47 nm, increasing with TMA concentration and sampling position (increasing residence time). On the other hand, mean aggregate sizes reached a maximum at about 4 mm above the bottom fuel duct (corresponding to a local temperature of only 1250 K) and increased with TMA seed level. Fractal dimension and fractal prefactor of alumina aggregates with negligible sintering rates were found to be 1.52 and 2.4, respectively. The final products were larger spherical particles with up to 60 nm diameter, resulting from complete "collapse" of the aggregates. These observations were shown to be compatible with our independent evaluation of the characteristic times associated with the participating rate processes in this class of two-phase CDFs. Systematic modification of these characteristic times can be used to control the size and morphology of flame-synthesized particles.

## NOMENCLATURE

$a$	"primary" particle radius	$K$	population-averaged collision frequency of aggregates, Eq. 10
$A_s$	projected area of aggregate constant, Eq. 13	$K'$	product of reaction rate constant and water vapor number density
$b$	constant, Eq. 13	$L$	projected maximum length of aggregate
$c$	dimensionless coefficient, Eq. 13	$m$	mass of particles/aggregates
$c_s$	mean thermal speed of gas molecules	$M$	molecular weight
$d_a^*$	area-equivalent diameter, Eq. 1	$n$	number density
$d_p^*$	"primary" particle diameter	$N$	number of "primary" particles in an aggregate
$D$	width-surface/width-grain boundary/volume diffusivity	$N_A$	Avogadro number
$D_f$	fractal dimension	$r$	hard sphere radius of molecule
$I_s$	scattered light intensity	$R$	universal gas constant
$k$	reaction rate constant for bimolecular collisions	$R_o$	area-equivalent radius
$k_a$	correlation coefficient, Eq. 2	$R_g$	radius of gyration
$k_B$	Boltzmann constant	$Re$	Reynolds number
$k_s$	fractal prefactor, Eq. 3	$t$	time
$k_L$	correlation coefficient, Eq. 4	$t_C$	characteristic coagulation time, Eq. 11
		$t_H$	characteristic TMA hydrolysis time, Eq. 8
		$t_{heat,a}$	thermal response time of aggregate

\*Corresponding author.

$t_L$	characteristic coalescence time for liquid particles, Eq. 15
$t_{mom}$	stopping time of aggregate, Eq. 18
$t_R$	characteristic residence time, Eq. 16
$t_S$	characteristic sintering time for solid-like particles, Eq. 14
$t_T$	characteristic heating (cooling) time, Eq. 17
$T$	temperature
$v_z$	vertical velocity ( $z$ -direction)
$V_p$	volume of a primary particle
$x$	horizontal coordinate parallel to the length of the lower burner slot (see Fig. 1)
$y$	horizontal coordinate parallel to the width of the lower burner slot (see Fig. 1)
$z$	vertical height above the lower burner slot (see Fig. 1)

#### Greek Symbols

$\alpha$	projected area exponent, Eq. 2
$\alpha_{mom}$	momentum accommodation coefficient (gas/particle)
$\beta_{ij}$	collision frequency of particles
$\delta$	neck radius
$\phi_p$	particle volume fraction
$\Phi$	equivalence ratio
$\Gamma$	nominal CDF strain rate
$\mu$	viscosity of liquid alumina
$\mu_L$	density of host gas
$\rho_s$	density of alumina particles
$\rho_p$	surface tension for liquid state
$\sigma_L$	surface energy for solid state
$\sigma_s$	width of surface layer
$v$	molecular volume of alumina
$\xi$	reaction probability
$\Psi$	fuel-to-oxidizer momentum flux ratio

#### Subscripts

$a$	aggregate property or area-equivalent property
$A, B$	TMA and $H_2O$ molecules, respectively
$p$	"primary" particle property

Superscripts  
 $(\bar{ })$  mean value over a population

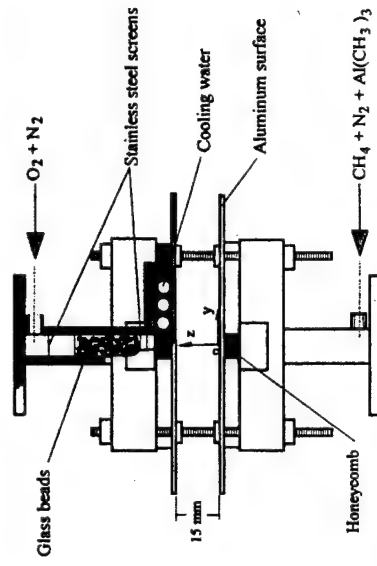


Fig. 1. Schematic of the rectangular counterflow diffusion flame (CDF) burner assembly.

Inorganic particles produced during combustion processes are almost always coagulated due to Brownian motion and often partially sintered due to high temperatures [1–4]. Consequently, the resulting aggregates can be quite different in morphology and size according to the flame conditions under which they are generated and "processed." At low temperatures, particle/aggregate evolution is dominated by coagulation, which leads to tenuously-structured aggregates that can be described using fractal concepts [5, 6]. When the temperature level is sufficiently high to cause sintering, such aggregates may have time to undergo restructuring processes leading to more compact morphologies ( $2 \leq D_f \leq 3$ ). Since the morphology of aggregates and their transport properties are interrelated [7, 8], it is important to understand not only synthesis but also the morphological evolution of aggregates in flames.

In this study, we examine a model laboratory system in which  $Al_2O_3$  aggregates are formed and restructured in a well-characterized locally flat laminar counterflow diffusion flame (CDF). This flame configuration provided access via both laser light scattering (LLS) and thermophoretic sampling probes for Transmission Electron Microscopy (TEM) analysis. Our goal is to demonstrate quantitatively how an understanding and control of the relevant chemical and physical rate processes can be used to generate ultrafine inorganic oxides of tailored size and morphology in such combustion environments.

#### EXPERIMENTAL METHODS

##### Apparatus

###### Burner

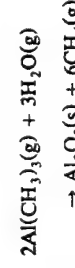
A rectangular counterflow diffusion flame (CDF) burner, similar in dimensions to that first developed by Chung and Katz [9], was constructed as the combustion environment in which ultrafine particles can be generated and modified in a controllable manner. Figure 1 illustrates a schematic of the CDF burner, which consisted of two identical rectangular

higher). The flow rates were controlled using calibrated variable-area flowmeters within 5%. The fuel stream gases (i.e.,  $CH_4$  and  $N_2$ ) were further dried and deoxidized by a gas purifier (Matheson 6412) to remove water vapor and oxygen amounts exceeding 0.5 and 0.1 ppm, respectively.  $CH_4/N_2$  flowing upward and  $O_2/N_2$  flowing downward formed a blue (non-sooting) flame sheet, which was stable and flat with uniform properties across the horizontal planes at fixed vertical directions, i.e., temperature, species concentrations and particle volume fraction were functions of only  $z$ . This one-dimensional feature, as will be discussed later on, makes the CDF burner an attractive configuration, i.e., a well-defined flame environment—for systematic studies of particle formation—evolution in diffusion flames [9].

##### Precursor

Liquid trimethylaluminum (TMA) was used as the precursor material to produce  $Al_2O_3$  (alumina) particles. TMA (Strem Chemicals), containing 97%  $Al(CH_3)_3$  and 3%  $AlH(CH_3)_2$ , was fed into an evaporator using a calibrated syringe (Hamilton 1001, 1 mL), which was controlled by a piston pump (Harvard Apparatus, 55-2226). The evaporator, a Pyrex tube (30 cm long and 3 cm diameter), was maintained at a temperature of 343 K using a heating tape to completely evaporate liquid TMA before being introduced to the burner. TMA reacts with

water vapor to produce alumina according to the following overall reaction:



During the present study, the evaporator was only connected to the fuel stream so that TMA reacted solely with flame-generated water vapor to form nanosized  $\text{Al}_2\text{O}_3$  particles since, as discussed above,  $\text{H}_2\text{O}$  and  $\text{O}_2$  in  $\text{CH}_4/\text{N}_2$  gas stream were eliminated using a purifier before entering the evaporator. Extreme caution must be practiced in handling TMA since it can react with both oxygen and water vapor in room air even at a temperature of 300 K.

#### Instrumentation

##### Thermophoretic Sampling (TS)

Thermophoretic sampling procedures were based on our adaptation of the experimental and theoretical methods established by Dobbin and Megaridis [10] and Rosner et al. [11], respectively. The technique involved quick insertion of a cold sampling surface into the hot flame environment to extract representative organic particles/aggregates using the phenomenon of thermophoresis. The cold surfaces were carbon-supported 400 mesh copper TEM grids with a 3 mm diameter (Electron Microscopy Sciences, CF-H4-spec-Cu). Each grid had a solid square area at the center and a thicker copper arrow from the side toward the center which allowed accurate positioning. The grids were attached onto a circular recess at the tip of a stainless-steel probe. The sampling probe was stored outside the flames with an alignment parallel to the flow field. A double-action pneumatic cylinder with a 51-mm stroke rapidly inserted the probe to the desired sampling position in the CDF. A single probe was inserted into one position at a time to minimize disturbances to the flow field. The special grid type used, together with careful alignment with respect to the flame (using laser light and cathetometer) provided a spatial resolution of about 0.4 mm. The actuation of a four-way valve, determining the insertion, sampling and

retraction times, typically resulted in a total of 100-ms exposure. Sampling times, measured using a translation potentiometer with output recorded on a digital oscilloscope, were selected to be about 70 ms in order that the collected particles/aggregates covered no more than 10% of the TEM grid. Sampling in the CDF was done at the four vertical positions of  $z = 2, 4, 6$  and 8 mm along the burner axis, i.e.,  $x = y = 0$ .

##### TEM and Image Processing

The particles/aggregates extracted from several positions in the CDF burner were subsequently observed using a Zeiss EM-10A Transmission Electron Microscope. The microscope had a point-to-point resolution of 0.3 nm and a maximum magnification of  $2 \times 10^5$ . The procedure to obtain images involved selecting aggregates randomly at relatively low magnifications near the center of our special grids. Aggregates were generally photographed at a magnification of  $4 \times 10^4$  while additional photographs were taken at a magnification of  $1.6 \times 10^5$  for obtaining detailed information regarding individual "primary" particles. The photographs taken at the TEM facility were ultimately digitized using a scanner (Microtek, ScanMaker II G). The digitized images were saved on a personal computer and analyzed with image processing software (Media Cybernetics, Image-Pro Plus). Each pixel on the digitized computer images was represented by a gray level between 0 and 255 together with a pair of coordinate numbers. The TEM images were calibrated by photographing a calibration grid (1134 parallel lines/mm) at each magnification used and by digitizing/analyzing with the same hardware/software. This made it possible to obtain a precise conversion from pixels to nanometers on the digitized images, yielding resolutions of 2 and 0.5 nm/pixel for aggregates and primary particles, respectively.

It should be emphasized that such high image resolution was necessary to accurately identify individual "primary" particles (ca. 20 nm diameter) in aggregates. The TEM measurements included "primary" particle diameters ( $d_p$ ), and projected areas ( $A_p$ ) and maximum lengths ( $L$ ) of aggregates. Experimental uncertainties of these morphological measurements on any

one aggregate/particle were expected to be less than 5%.

##### Laser Light Scattering (LLS)

Preliminary light scattering experiments were also conducted in order to supplement TS/TEM measurements. This involved a 5-W Argon-Ion laser (Coherent, Innova 70) operating at 514.5 nm. The incident beam was first passed through a polarization rotator and then steered by a couple of mirrors towards the burner. The beam, modulated by a light chopper (EG & G, 197) at a frequency of 1200 Hz, was focused at the center of the burner ( $x = y = 0$ ) using a 350 mm focal length lens. This resulted in a waist diameter of 160  $\mu\text{m}$  with a confocal length of 140 mm. The scattered light was collected at 90 degrees using a 125 mm focal length lens, a polarizer, a laser line filter (1 nm bandwidth), and a photomultiplier tube (EMI, 9558B). The apertures in front of the collecting lens and PMT defined a solid angle of 0.2 msr with a 1 mm long sampling volume at 90 degree scattering angle. The signal from the PMT was fed into a lock-in amplifier (EG & G, 5208) to discriminate unwanted photon sources, e.g., flame radiation, room light. The experimental uncertainties (95% confidence interval) of the LLS measurements were estimated to be less than 10%, generally dominated by finite sampling times. Note that light extinction (transmission) measurement was not possible in these TMA-seeded CDFs because alumina particles do not appreciably absorb light, i.e., its refractive index is approximately real.

##### Thermocouple (TC)

Temperatures in the CDF reactor were measured using a Pt/Pt-6% Rh thermocouple in the absence of alumina particles since the seeding of the fuel with particle precursor (TMA) in such small amounts (vapor mole fractions of less than 0.24%) is estimated to affect the thermal field insignificantly (less than 50 K) in the CDF. The TC lead wires were 250  $\mu\text{m}$ , resulting in a junction bead diameter of about 450  $\mu\text{m}$ . These measurements involved insertion of the thermocouple into desired sampling position (along  $z$  axis,  $x = y = 0$ ) and averaging the signal over 10 s. The TC output reading was corrected for radiative heat

transfer losses, which basically included a radiation/convection heat transfer balance assuming negligible heat loss by conduction due to TC assembly alignment with isotherms. Note that the Nusselt number was essentially equal to 2 for this low-velocity ( $\text{Re} < 0.1$ ) flow around the spherical TC bead in the CDF. Additionally, the emissivity of the TC bead was calculated from  $0.1(T/100)^{0.76}$ . Positioning of the TC was accomplished using a cathetometer with better than 0.5 mm accuracy. The experimental uncertainties (95% confidence interval) in temperature measurements were estimated to be generally less than 80 K, largely dominated by possible errors in the above-mentioned systematic radiation corrections (less than 265 K).

#### Flame Conditions

Several flames were tested at the beginning of this investigation; however, only one particularly suitable flame was chosen for a detailed study of the synthesis and restructuring of alumina particles. The experimental conditions for this laminar counterflow diffusion flame are summarized in Table 1. The fuel ( $\text{CH}_4/\text{N}_2$ ) and oxidizer ( $\text{O}_2/\text{N}_2$ ) gas flow rates were adjusted to obtain relatively high fuel-to-oxidizer momentum flux ratio ( $\Psi = 3.5$ ) and small equivalence ratio ( $\Phi = 0.68$ ). The sum of total fuel and oxidizer side exit velocities of 13.1 and 6.5 cm/s divided by the burner separation distance of 15 mm yielded a nominal strain rate of  $\Gamma = 13 \text{ s}^{-1}$  for this CDF. These parameters, as will be discussed in detail in the next section, determine the general flame structure. Briefly, the location of gas stagnation plane is

TABLE I

Flame Conditions			
Fuel Side	Oxidizer Side	Flow Rates* (cm <sup>3</sup> /s)	Flame Parameters
$\text{CH}_4$	$\text{N}_2$	14.8	$\Psi^b$
14.8	79.6	43.5	$\Phi^c$
		3.4	$\Gamma^d$ (s <sup>-1</sup> )
		3.5	0.68
		13	

\* At normal temperature and pressure.  
b Fuel-to-oxidizer momentum flux ( $\rho v^2$ , at burner exits)  
c Equivalence ratio.  
d Nominal strain rate.

controlled by  $\Psi$ , flame location by  $\Phi$ , and residence time and flame temperature by  $\Gamma$ . Additionally, the effect of TMA concentration on the morphological evolution of alumina particles were studied using four different seed levels of 0.2, 0.4, 0.8 and 1.6 mL/h. These pumping rates yielded TMA vapor mole fractions of less than 0.24% entering the burner with the fuel stream, resulting in  $\text{Al}_2\text{O}_3$  particle volume fractions less than 0.3 ppm in the flame. Finally, it is to be noted that the flame conditions were repeatable within 5% from one experiment to another.

## RESULTS AND DISCUSSION

### Flame Structure

Figure 2 shows as-measured and radiation-corrected temperatures as a function of vertical position,  $z$ , in our CDF reactor. Although high temperature gradients (ca. 450 K/mm) were present in the  $z$  direction, it was found that temperature variations in  $x-y$  planes at fixed  $z$  positions were always less than 1% for  $|x| < 32$  mm,  $|y| < 6.5$  mm. This observation, together with similar invariance of scattered signal in  $x-y$  planes, indicated that our flame was indeed flat and stable. As can be seen from Fig. 2, the maximum temperature was about 2270 K in the CDF after a radiation heat loss correction of ca. 265 K. The flame (FL) position, here defined by the location of this peak temperature, was at  $z_{\text{FL}} = 6.3$  mm. The particle stagnation plane (PSP), measured from the fall-off of the light scattering signal, was at  $z_{\text{PSP}} = 8.7$  mm. The gas stagnation plane (GSP) was estimated to be near the particle stagnation plane ( $z_{\text{GSP}} = 8.5$  mm) using  $z_{\text{PSP}}$  and the local  $(dT/dz)/T$  [12]. Under the present test conditions, the general structure of our counterflow diffusion flame is illustrated in Fig. 3, which includes representative gas streamlines, thermophoretic sampling positions, particle and gas stagnation planes as well as flame position. The PSP is relatively close to the top burner exit allowing a larger spatial scale for evolution of alumina particles. In this flame structure, particles formed well below the flame (fuel side) can pass higher temperature regions and ultimately through the flame. Since particles

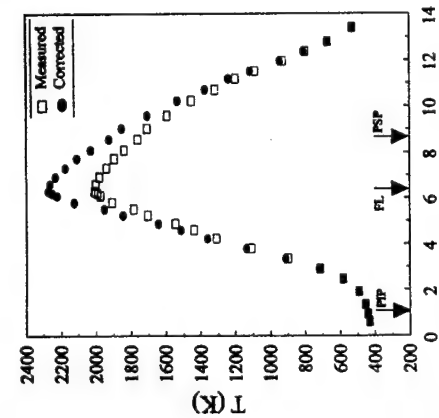


Fig. 2. As-measured and radiation-corrected temperatures as a function of vertical position  $z$  (at  $x = y = 0$ ) in the CDF burner.

cannot cross and flow further upward in the burner beyond PSP, due to a balance of aerodynamic and thermal forces, the relative location of this plane dictates particle synthesis and restructuring processes in CDFs by controlling the temperature-time history of the particles [12–14].

### Overview of Particle Synthesis and Restructuring in CDF

Figure 4 shows typical TEM photographs of alumina particles/aggregates thermophoretically extracted from four different vertical positions in our CDF reactor. Only the images corresponding to 0.8 mL/h TMA seed level (corresponding to a particle volume fraction of ca. 0.3 ppm) are illustrated since the particle/aggregate morphologies for other seeding levels were essentially similar. Note that the magnification for these four images is identical and equal to  $8 \times 10^4$ . Figure 4 clearly demonstrates the evolution of alumina particles as they move from the particle inception plane (PIP) to the particle stagnation plane (PSP). PIP is the location at which the precursor (TMA) first reacts with the water vapor in the

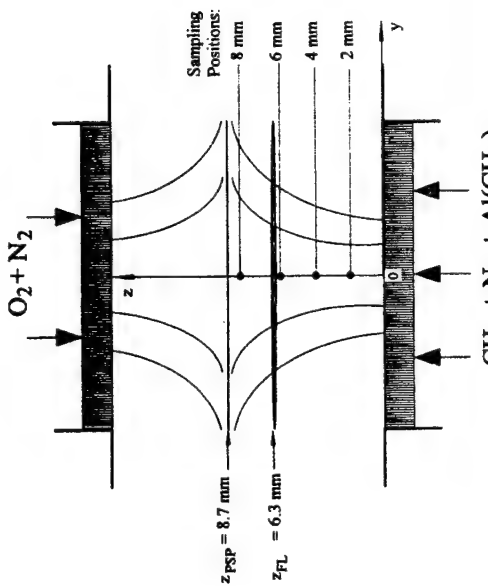


Fig. 3. General structure of the CDF, showing representative flow field, particle stagnation plane (PSP), flame position (FL), and thermophoretic sampling positions.

to more compact particles due to this sintering process. Obviously, the resulting nearly spherical particles are larger than the "primary" particles in the parent aggregates. Sintering and aggregation processes contribute to the net growth of aggregates in opposite directions, i.e., sintering decreases the mean aggregate size,  $\bar{N}$ , whereas aggregation tends to increase  $\bar{N}$ . From  $z = 6$  mm to  $z = 8$  mm, the mixture of particles and aggregates crosses the flame (the highest temperature region) where sintering becomes the dominating mechanism. At the highest position of thermophoretic sampling, mostly single particles coagulate to form polydisperse aggregates with diameters exceeding 50 nm are observed. Beyond this location, particles at most reach the PSP, at which they flow out of the burner. The above stages generally describe how the alumina evolves from small (sub-nanometer) "primary" particles to large aggregates ( $z = 2-4$  mm) and then aggregates to larger particles ( $z = 4-8$  mm) because of the thermal and flow structure of the countercurrent diffusion flame. This is of great importance in many engineering applications in which the objective

is to great importance in many engineering applications in which the objective

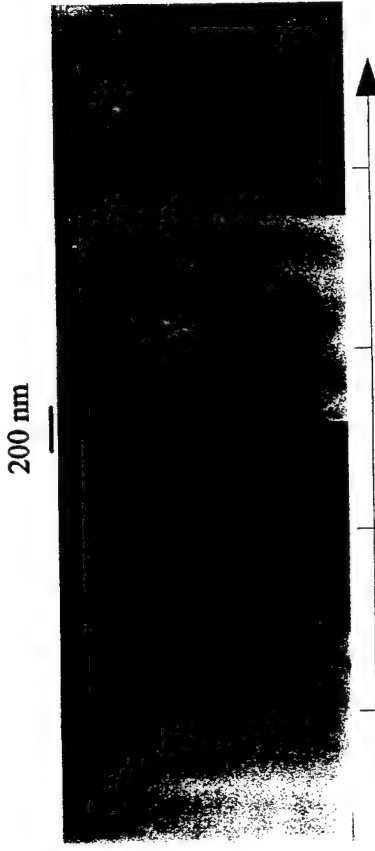


Fig. 4. Typical TEM images of alumina aggregates/particles thermophoretically extracted from four vertical positions in the CDF for 0.8 mL/h TMA concentration.

is to produce particles/aggregates with known size and morphology, in a controllable manner. To illustrate the use of CDF for particle production, the nucleation/growth/aggregation/sintering mechanisms will be quantified by analyzing our TEM and LLS results in detail below. The effect of precursor concentration on the particle/aggregate size and morphology will also be discussed.

#### "Primary" Particle Characteristics

"Primary" particle sizes represented here were measured directly from digitized TEM micrographs by detecting the apparent spherical profiles of the constituent particles near the peripheries of aggregates at relatively high microscope magnifications. When single particles rather than aggregated particles were present due to sintering at high temperatures, measurements of particle sizes simply involved the unambiguous diameters. Particles for a particular sampling condition are represented here by a mean diameter because of the narrow prevailing size distribution. Mean particle diameters,  $\bar{d}_p$ , were obtained by averaging over about 80 obvious particles at the corresponding sampling positions for each precursor concentration. The mean particle diameter as a function

of vertical position in our CDF burner is shown in Fig. 5 for four different TMA seed levels. The locations of the flame (FL) as well as the particle stagnation plane (PSP) are also indicated for reference. Mean "primary" particle diameters were measured to be in the range of

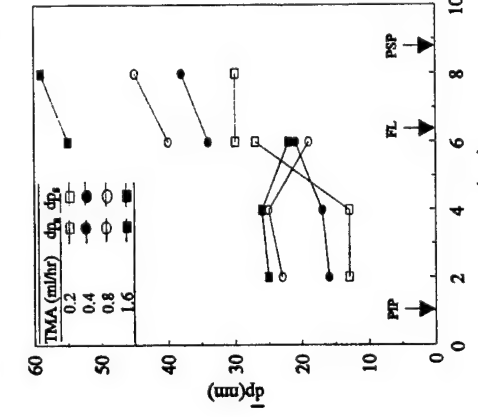


Fig. 5. Mean "primary" particle diameter as a function of vertical position in the CDF for various TMA seed levels.

13–25 nm at  $z = 2$  mm, only about 1 mm downstream of the corresponding particle inception planes (PIP). Generally, the change in particle sizes for a specific precursor seed level was insignificant in low temperature regions, including  $z = 2$  and 4 mm. In this region of the CDF, only aggregated particles were observed so that the  $\bar{d}_p$  results shown in Fig. 5 for these two lowest positions represented mean diameters of particles in aggregates. However, as the thermophoretic sampling location was moved to  $z = 6$  mm, a mixture of single particles and aggregated particles started appearing on TEM grids. The difference in sizes between the unaggregated and aggregated particles were so significant that it was necessary to consider these two diameters separately at 6 mm. Consequently, Fig. 5 includes both mean particle sizes; one due to particles in aggregates,  $\bar{d}_{p_a}$ , and the other due to single (coalesced) particles,  $\bar{d}_{p_s}$ . As can be noticed, the mean diameter of aggregated particles changed slightly from 4 mm to 6 mm, following the similar trend from 2 mm to 4 mm. This observation implies that the growth rate of particles in the absence of sintering is relatively small in this CDF configuration. On the other hand, the mean diameter of single particles increased drastically for all precursor seedings at  $z = 6$  mm, apparently due to sintering effects at high temperatures (this sampling position was the closest to the flame). For example,  $\bar{d}_{p_s}$  was 40 nm, compared with  $\bar{d}_{p_a} = 19$  nm, at 6 mm for 0.8 mL/h TMA concentration. As the mixture of single and aggregated particles passed through the flame, most of the remaining aggregates continued to restructure into spherical forms, minimizing the free energy. Since the final alumina products were mostly compact particles resulting from the complete collapse of the aggregates in such a high-temperature environment, the largest single spherical particles, with mean diameters ranging from 30 to 58 nm, were measured at  $z = 8$  mm in the CDF. It is also to be noted that  $\bar{d}_{p_s}$  increased slightly from  $z = 6$  to 8 mm, which was the closest sampling location to PSP.

The effect of precursor concentration on the mean "primary" particle diameter in this particular CDF environment was also studied by considering four successively doubled TMA

seed levels. As can be seen in Fig. 5, from 0.2 mL/h to 1.6 mL/h of TMA, the mean diameter of particles within aggregates increased almost 100% for the sampling positions of  $z = 2$  and 4 mm. Although coarsening of the aggregates made it somewhat difficult to accurately measure individual profiles of particles in aggregates at the higher position of 6 mm, the results indicated a relatively small variation of  $\bar{d}_{p_s}$  with respect to TMA concentration. However, as a result of sintering,  $\bar{d}_{p_s}$  clearly increased 100% as the TMA seed level was increased 8 times from 0.2 to 1.6 mL/h at this position close to the flame. Moreover, the difference between  $\bar{d}_{p_s}$  and  $\bar{d}_{p_a}$  was higher for higher precursor concentration at  $z = 6$  mm. Finally, similar behavior was observed at 8 mm, where a four fold TMA increase resulted in approximately doubling the final mean diameter of the sintered particles.

#### Aggregate Characteristics

After particles reach certain sizes (ca. 10 nm) at relatively low temperatures in our CDF, size-dependent coalescence becomes too slow and these "primary" particles start forming rationally-structured aggregates. Although the "primary" particles are nearly monodisperse, the variations in aggregate sizes are usually considerable, i.e., they are noticeably polydisperse. Generally, projected areas of aggregates,  $A_a$ , as well as their maximum lengths,  $L$ , can be directly measured from the analysis of TEM images. The area-equivalent diameter,  $d_a$ , is calculated as follows:

$$d_a = \left( \frac{4A_a}{\pi} \right)^{1/2} \quad (1)$$

This length scale,  $d_a$ , is related to the free molecule regime mobility diameter of aggregates and also to the number of particles contained in an aggregate [15–18]. Therefore, area-equivalent diameters were calculated from the measured projected areas following Eq. 1 for 50 to 140 aggregates/particles at each sampling condition during the present investigation.  $d_a$  for alumina produced in the CDF was observed to lie mostly in the range of 20 to

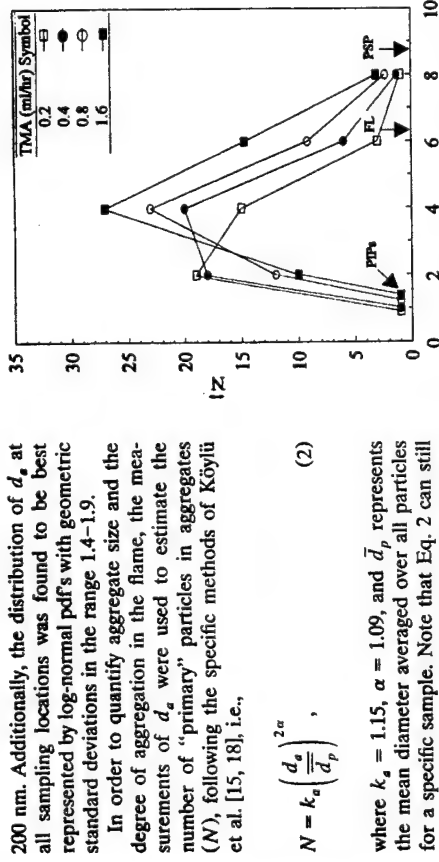


Fig. 6. Mean number of "primary" particles per aggregate as a function of vertical position in the CDF for various TMA seed levels.

200 nm. Additionally, the distribution of  $d_a$  at all sampling locations was found to be best represented by log-normal pdfs with geometric standard deviations in the range 1.4–1.9. In order to quantify aggregate size and the degree of aggregation in the flame, the measurements of  $d_a$  were used to estimate the number of "primary" particles in aggregates ( $N$ ), following the specific methods of Köylü et al. [15, 18], i.e.,

$$N = k_s \left( \frac{d_a}{\bar{d}_p} \right)^{2\alpha}, \quad (2)$$

where  $k_s = 1.15$ ,  $\alpha = 1.09$ , and  $\bar{d}_p$  represents the mean diameter averaged over all particles for a specific sample. Note that Eq. 2 can still be applied in the  $N \rightarrow 1$  limit. The mean number of particles per aggregate ( $\bar{N}$ ), calculated by averaging over 50–140 aggregates per sample, is illustrated as a function of the vertical position in Fig. 6 for the experimental conditions of the present study. Near PIP, aggregation starts presumably from a "burst" of quasi-spherical sub-nanometer single particles. In general, the mean number of particles per aggregate reached maximum values of 15 to 27 at  $z = 4$  mm, after which  $\bar{N}$  decreased monotonically. The increase in  $\bar{N}$  at the beginning is obviously the result of the rapid Brownian-diffusion-driven aggregation process with negligible restructuring. On the other hand, the decrease in  $\bar{N}$  is due to sintering of these larger "primary" particles, accompanied by "coarsening" of the aggregates at sufficiently high temperatures. These two competing mechanisms changed surface areas of aggregates in the opposite directions. The  $z$ -location where  $\bar{N}$  peaks, which depends on the detailed kinetics of aggregation and sintering in any given system, was about 4 mm for the present experiments. Beyond this location, sintering effects became significant compared to aggregation, causing  $\bar{N}$  to approach unity near PSP, at which final alumina products were ejected from the CDF.

Figure 6 also shows the effect of TMA seed level on aggregate sizes. Noticeably, at  $z = 2$  mm,  $\bar{N}$  increased from 10 to 19 as the TMA

gyration,  $R_t$  [5, 6]:

$$N = k_s \left( \frac{2R_t}{\bar{d}_p} \right)^{D_f}, \quad (3)$$

where  $k_s$ ,  $\bar{d}_p$ , and  $D_f$  are the fractal prefactor, mean "primary" particle diameter, and fractal dimension, respectively. It has been recently emphasized that  $k_s$  as well as  $D_f$  must be known in order to properly characterize the structure of combustion-generated fractal-like aggregates [15, 18]. Indeed, more elegant treatment of Neimark et al. [19] demonstrated that the aggregates produced in combustion environments are more precisely described as *self-affine* rather than self-similar objects.

Since the actual three-dimensional radii of gyration of aggregates are not readily available from the projected TEM images, an alternative form of Eq. 3 can be expressed as follows:

$$N = k_s \left( \frac{L}{\bar{d}_p} \right)^{D_f}, \quad (4)$$

where the correlation constant,  $k_L$ , is related to  $k_s$  in Eq. 3 by

$$\frac{k_s}{k_L} = \left[ \frac{(D_f + 2)}{D_f} \right]^{D_f/2}. \quad (5)$$

Equation 5 was the result of the detailed analysis of Ref. 15, in which it was shown that this approximate relationship not only applies to straight chains ( $D_f = 1$ ), disks ( $D_f = 2$ ), and spheres ( $D_f = 3$ ) but also to combustion-generated aggregates with  $D_f = 1.7$  (within 10% accuracy).

Figure 7 illustrates the number of particles in an aggregate as a function of its maximum length (outer diameter) for more than 1000 alumina aggregates thermophoretically extracted from the TMA-seeded CDF. Note that maximum lengths of individual aggregates are normalized by the mean particle diameter associated for each sampling condition. The aggregates shown in Fig. 7 included only those with  $N > 4$  and sampled from  $z = 2$ , 4, and 6 mm so that the ones experiencing significant high temperature sintering were avoided. The least-square fit to this data in the form of Eq. 4

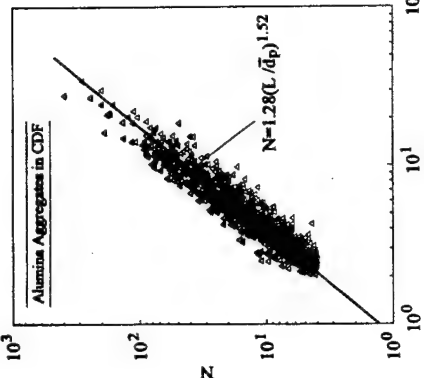


Fig. 7. Number of "primary" particles in an aggregate as a function of its normalized maximum projected length for more than 1000 alumina aggregates (with insignificant sintering) thermophoretically extracted from TMA-seeded CDF burner.

yielded  $D_f = 1.52$  and  $k_L = 1.28$ , which corresponds to  $k_s = 2.4$  using Eq. 5. Therefore, for this population of alumina aggregates in the absence of appreciable sintering, the fractal characteristics are almost insensitive to sampling position and precursor concentration. These results also indicated that the inorganic aggregates with  $D_f < 2$  are similar at different stages of the aggregation process, which can be most likely represented by the cluster-cluster aggregation mechanism. Although the fractal dimension reported here is somewhat lower than 1.7, these  $D_f$  and  $k_s$  values for alumina are in the same ranges as for many other flame-generated materials, including carbonaceous soot [15, 18, 20, 21], suggesting that the fractal characteristics are also relatively insensitive to the material composition of aggregates that are not restructuring due to high temperature coalescence or oxidation. Apparently, in the initial stages of restructuring, alumina aggregates with  $D_f < 2$  underwent changes without appreciable changes in the fractal dimension. However, as these aggregates crossed the flame, moving toward the

PSP, they completely collapsed to form single spherical particles due to significant sintering/coalescence rate process. In this case of compact shapes at  $z = 8$  mm,  $N \rightarrow 1$ , implying  $D_f \rightarrow 3$ . This evolution of the fractal dimension from 1.5 to 3 is mainly the result of two competing process: aggregation and sintering. When the aggregation was rapid enough to dominate sintering ( $z < 6$  mm), the observed aggregates appeared tenuous and exhibited low fractal dimensions ( $< 2$ ). As expected from a cluster-cluster aggregation mechanism, the aggregation process in our CDF increased the aggregate sizes but had little effect on the fractal dimension. However, when the sintering dominated, initially open structures became compact ( $D_f \rightarrow 3$ ) within the high temperature regions of the flame. Note that in this limit of  $N \rightarrow 1$ ,  $k_s = (5/3)^{1/2} = 2.15$  since  $R/d_p = (3/20)^{1/2}$  for a sphere. This implies that although sintering increases the fractal dimension [22], it has relatively small effect on the fractal prefactor.

#### In Situ LLS Evidence of Morphological Evolution

Figure 8 shows the LLS measurements of the present study for three TMA seed levels. The first noticeable feature of Fig. 8 is that the scattered intensity increased with increasing TMA concentration. Noting that, approximately,  $I \propto n^6 d_p^6 N$  [23], this is expected since a change in the precursor level, without considering other effects on morphology, directly corresponds to a change in particle number density. Additionally, as the TMA seed level was increased, PIP moved slightly to higher positions in the flame. This observation, together with the existence of a clear-cut onset of light scattering for each seed level, suggests that the extremely fast reaction of TMA is mainly controlled by the back-diffusion of water vapor produced in the "downstream"  $\text{CH}_4$  combustion reaction.

The scattering results shown in Fig. 8 have

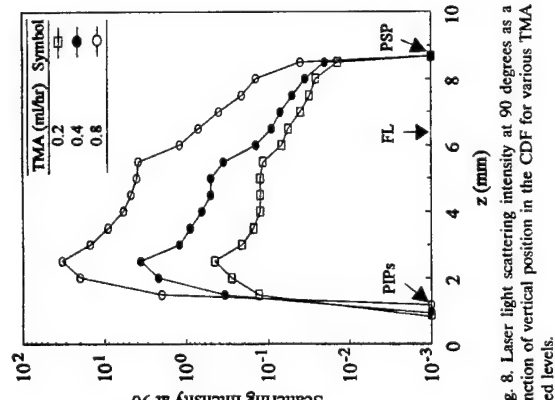


Fig. 8. Laser light scattering intensity at 90 degrees as a function of vertical position in the CDF for various TMA seed levels.

crease in scattering intensity from PIP up to 2.5 mm indicates that "primary" particle as well as aggregate sizes increase in this initial formation step. Moreover, the peak in the scattering intensity at about  $z = 2.5$  mm was relatively insensitive to the precursor seed level. Considering that mean "primary" particle diameter does not change between 2 and 4 mm for a specific TMA level (see Fig. 5), this peak scattering intensity should correspond to a peak in number of primary particles per aggregate at around 2.5 mm. This is consistent with the TEM measurements shown in Fig. 6, which indicates that  $\bar{N}$  increases to a peak at  $z = 4$  mm (note that no thermophoretic sampling was available for  $2 < z < 4$  mm). After  $z = 2.5$  mm, the scattering intensity decreased slightly as a result of decreasing  $\bar{N}$  since sintering started balancing the effect of coagulation. As seen from the plateau region in the light scattering between  $z = 4$  and 5 mm, the competition between coagulation and sintering seemed to reach some kind of equilibrium state at these positions in the CDF. This local level-off in the scattering intensity in Fig. 8 is probably

the result of a compromise between the increase in  $d_p$  and the decrease in  $\bar{N}$ . Beyond  $z = 5.5$  mm, the scattering intensity decreased continuously because of the dominant sintering mechanism at higher positions between flame and PSP. Therefore, a temperature of about 1900 K can be considered sufficient to cause significant collapse of these alumina aggregates. Finally, scattered laser light intensity drops to a molecular level at  $z = 8.7$  mm (PSP) since the final alumina products, with spherical shapes, here exit the CDF burner.

The above *in situ* LLS results clearly track the morphology evolution of alumina from individual particles to aggregates due to coagulation (between PIP and  $z = 2.5$  mm), aggregation (between PIP and  $z = 5.5$  mm), restructuring due to the competition between coagulation and sintering (between  $z = 2.5$  and 5.5 mm), and from aggregates to mostly compact particles due to high-temperature sintering (between  $z = 5.5$  mm and PSP). In the next section these simultaneous processes are discussed in greater detail by considering their relevant characteristic times to obtain a better insight into the synthesis and restructuring of inorganic particles in such flame environments.

#### Restructuring and Characteristic Times

Since many rate processes occur simultaneously in the CDF, consideration of their characteristic times [24] is useful in gaining an understanding of this chemically reacting system. For the system at hand, viz. inorganic particle formation and evolution in CDFs, the following characteristic times are relevant: homogeneous chemical reaction times, coagulation times, coalescence times, flow (residence) time, and aggregate (momentum, heat transfer) response times. In any system in this broad class, these times completely control the size and morphology of the inorganic particles for tailoring the desired final product.

#### Reaction Time

Since the kinetic data for the TMA hydrolysis reaction is not readily available, we apply the bimolecular collision rate theory, assuming hard sphere collisions, to estimate the TMA hydrolysis time ( $t_H$ ). The reaction rate con-

stant,  $k$ , for a bimolecular reaction is given by [25]

$$k = \xi N_A \left[ \left( \frac{8RT}{\pi} \right) \left( \frac{1}{M_A} + \frac{1}{M_B} \right) \right]^{1/2} \cdot (\pi r_A r_B) \quad (6)$$

where subscripts  $A$  and  $B$  represent TMA and  $\text{H}_2\text{O}$ , respectively,  $\xi$  is the reaction probability normally less than unity, and  $r_A, r_B = r_A + r_B$ . In a batch system, the reaction rate is given as  $dn_A/dt = -K' n_A$ , where  $K' = kn_B$ . By neglecting the depletion of  $\text{H}_2\text{O}$ ,  $K'$  can be taken as constant, resulting in the following relationship:

$$\frac{n_A}{n_A(0)} = \exp(-K't). \quad (7)$$

Then the TMA hydrolysis lifetime, here defined as the time when 99% TMA reacts with water vapor, can be expressed

$$t_H = \frac{4.6}{K'}. \quad (8)$$

#### Coagulation Time

The collision frequency of particles with rapid coalescence in the free molecular regime is given by [26]

$$\beta_{ij} = \left[ \left( \frac{8k_B T}{\pi} \right) \left( \frac{1}{m_i} + \frac{1}{m_j} \right) \right]^{1/2} \cdot \pi(r_i + r_j)^2. \quad (9)$$

When the particles are so large as to not coalesce upon collision under given conditions, the above relation must be modified to apply to aggregates [27, 28]. In practice, it is convenient and sufficiently accurate to use the length scale  $R_a$  ( $= d_a/2$ ), easily obtainable from TEM measurements. Additionally,  $R_a$  correlates with the collision radius with a coefficient of the order of unity [16, 17, 27]. Therefore, the collision cross section for aggregates is expressed as  $\pi(R_a + R_g)^2$ . The mass of the aggregate is related to the number of primary particles in the aggregate, i.e.,  $m = N(\rho V_p)$  with the volume of a primary particle being  $V_p = \pi d_p^3/6$ . Substituting these relationships into Eq. 9, and using the population-averaged values, we ob-

For solid-like) particles, surface- or bulk-diffusion may account for their sintering rates.

For the three diffusion models reviewed by Coblenz et al. [31], the following relationship is generalized for the neck growth of two spherical particles at the initial stage:

$$\frac{2}{t_C} = \frac{\rho_p}{Kt_a}, \quad (11)$$

where  $a = d_p/2$ ,  $b = 5$ ,  $b' = 3$  for volume diffusion,  $b'' = 4$  for grain boundary and surface diffusion, and  $c$  is a dimensionless coefficient, which also depends on the sintering processes. If Eq. 13 is formally extrapolated to the later stages, then the characteristic sintering time for two adjacent solid particles,  $t_s$ , can be expressed as:

$$t_s = \frac{RTa'}{cD_{\text{eff}}}. \quad (14)$$

For the coalescence of liquid particles, surface-energy driven Newtonian viscous flow occurs and the following relationship should apply [32]:

$$t_L = \frac{\mu_L d_p}{\sigma_L}. \quad (15)$$

Flow Times  
A local residence time for any non-uniform steady flow system can be defined as  $[v_r \cdot \text{grad}(\ln v)]^{-1}$ , or in our CDF,

$$t_R = \left| \frac{dv_r}{dz} \right|^{-1}, \quad (16)$$

where  $z$  is measured along the flow direction. This can be regarded as the residence time associated with an appreciable fractional change in fluid velocity. Perhaps more significant for temperature dependent processes is the characteristic time

$$t_T = \left| v_r \frac{d(\ln T)}{dz} \right|^{-1}, \quad (17)$$

which is a measure of the local cooling (or heating) rate along the axial streamline.

#### Aggregate Response Times

To assess the ability of aggregates to "track" the above-mentioned changes in gas velocity

and temperature, we also compute the characteristic stopping time,  $t_{\text{mom}}$ ,<sup>a</sup> and associated thermal response time,  $t_{\text{heat}}$ ,<sup>b</sup> [24] both evaluated in the free-molecular limit. According to Ref. 33,  $t_{\text{mom}}$  will be larger than that of each of its primary particles by about the factor  $1.02N^{0.14}$  (for  $D_f \approx 1.8$ ) due to a slight "shielding" effect.<sup>2</sup> Accordingly, we estimate

$$t_{\text{mom}} = \frac{1}{\left( 1 + \frac{\pi \alpha_{\text{mom}}}{8} \right)} \left( \frac{\rho_p}{\rho_g} \right) \left( \frac{a}{c} \right) \times (1.02N^{0.14}), \quad (18)$$

where  $\bar{c}_g$  is the mean thermal speed of background gas molecules. Since the specific heat capacity of the "primary" particles is close to that of the background gas, and the relevant gas/particle thermal accommodation coefficient is unlikely to be much smaller than unity, we can take  $t_{\text{heat}}$ <sup>a</sup> to be comparable to  $t_{\text{mom}}$ .<sup>a</sup> In the following subsection we find that these aggregate response times are less than 1  $\mu\text{s}$  and, hence, smaller than the above-mentioned flow times by some 4 decades. We conclude that, apart from aggregate thermophoretic drift relative to the gas [12], aggregates in this CDF

<sup>a</sup> As found for the accessible area of fractal aggregates [7]. These power laws are only locally valid approximations.

<sup>b</sup> Calculated from the Lennard-Jones size-parameter results.

#### Characteristic Time Map for Particle / Aggregate Formation / Evolution in CDF

While a more detailed theoretical treatment of the structure in our two-phase CDF, including particle morphology evolution, is beyond the scope of the present paper [34], our objective in this section is to elucidate the evolution processes of alumina particles with the help of the above-mentioned characteristic times. In calculating these times, the following assumptions and simplifications, in addition to the ones already discussed in the previous section, are considered to be suitable for the TMA-seeded CDF: (1) TMA hydrolysis is complete; i.e., all TMA reacts with water vapor to form alumina, implying that the "initial" solid volume fraction ( $\phi_p(0)$ ) is known immediately beyond PIP. (2) Some bulk properties are approximately applicable even to "nanosized" particles. The physical data used in our present estimates are summarized in Table 2.

TABLE 2  
Data Used for Estimating Characteristics Times for Alumina Formation/Evolution in CDF

Property	Value	Reference
$\xi$	1	Moore and Pearson [25]
$r_A$	$3.08 \text{ \AA}^b$	Mole and Jeffreys [40]
$r_B$	$1.41 \text{ \AA}^b$	Rosner [24]
$M_A$	$72.09 \text{ g/mol}$	Dyns et al. [41]
$M_B$	$18.02 \text{ g/mol}$	Kingery [42]
$\sigma_A$	$905 \text{ erg/cm}^2$	Coblenz et al. [31]
$\sigma_B$	$2797.24 \text{--} 0.8913T$	Dyns et al. [41]
$\rho_p(t=0)$	$3.97 \text{ g/cm}^3$	Turkdogan [44]
$c$	$2.74 \times 10^{-7} \text{ for a TMA seed level of } 0.8 \text{ mL/h}$	Turkdogan [44]
$D = \omega D_s$	225 for surface diffusion; 120 for volume diffusion	Coblenz et al. [31]
$D = D_c$	$1.89 \times 10^3 \exp(-80523/T) \text{ cm}^2/\text{s}$	Dyns et al. [41]
$v$	$1.36 \times 10^5 \exp(-69401/T) \text{ cm}^3/\text{s}$	Cannon et al. [43]
$\mu_L$	$2.2 \times 10^{-29} \text{ m}^3$	Dyns et al. [41]
$T_{\text{melting point}}(\text{r-Al}_2\text{O}_3)$	$1.12 \times 10^{-4} \exp(13832/T) \text{ Ns/m}^2$	Turkdogan [44]
	2327 K	

<sup>a</sup> Calculated from the stereo structure of TMA.

<sup>b</sup> Calculated from Lennard-Jones size-parameter results.

are strongly coupled to the local gas velocity and temperature.

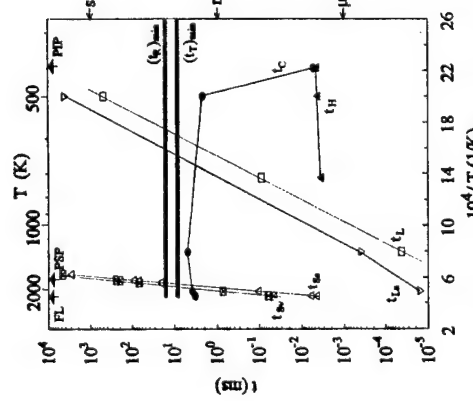


Fig. 9. Characteristic times (log-scale) as a function of reciprocal temperature for elucidating the formation and evolution of alumina particles in the CDF.

lated from Eqs. 16 and 17 using our radiation-corrected TC measurements for temperature and single-phase numerical simulations for axial gas velocity [34]. The minimum values of these flow times were shown in the figure, i.e., the local times were located on or above the crossed lines. As previously stated, aside from the chemical reactions, the physical processes of coagulation and sintering compete with each other. While coagulation depends on temperature with a weak exponent (see Eq. 10), sintering and/or viscous flow processes are more sensitive to local temperature because of the exponential dependence on temperature of the diffusivities and viscosity (liquid). Indeed, this fact motivated our choice of coordinates in Fig. 9.

Sintering times due to surface diffusion ( $t_{ss}$ ) and volume diffusion ( $t_{vv}$ ) for 10 nm primary particles are also plotted in Fig. 9, which indicate for rapidly producing apparently dense ( $D_f \approx 3$ ) spherules of the order of 10 nm, even at temperatures as low as 500 K (see Figs. 2 and 5) from  $\text{Al}_2\text{O}_3$  "monomers" (initially of diameter ca. 0.4 nm) "released" near PIP. Figure 9

cates that they are much larger than other particle-related times up to about 1900 K. The intersections of  $t_c$  with  $t_{ss}$  and  $t_{vv}$  occur at about 2000 K and 1900 K, respectively—temperatures indeed in the range where appreciable  $\text{Al}_2\text{O}_3$ -aggregate restructuring is observed in this CDF. Since the aggregate sintering time should be larger than that of its constituent "grains," the temperature for significant sintering due to condensed-phase processes is expected to be higher for the collapse of aggregates. According to our estimates of the characteristic times for surface energy-driven viscous flow sintering (for 10-nm "primary" particles, and  $D_f = 1.52$  fractal aggregates, shown in Fig. 7) evidence of aggregate restructuring by this mechanism should set in well below 1000 K in this CDF. Why this does not occur is an interesting question which remains for future investigation.

In estimating the viscous sintering rate of alumina aggregates comprised of up to 24 "primary" particles on the average (TMA concentration 0.8 mL/h), we use the simulation results of Tandon and Rosner [8], i.e., the collapse time for aggregates ( $t_{ss}$ ) via viscous sintering is not expected to be sensitive to aggregate size  $\bar{N}$ . Accordingly, we take the ratio of times for aggregate to its initial constituent particles to be about 3.5, corresponding to an aggregate comprising 20 "primary" particles with an initial fractal dimension of 1.5. For comparison, Fig. 9 also shows the sintering time ( $t_s$ ), which scales linearly with "primary" particle size. Thus, immediately after particle inception, even this mechanism of restructuring is too slow, and rapid "monomer" aggregation due to Brownian coagulation is expected up to at least ca. 600 K. (Indeed, from our TEM micrographs, there were few changes in the center-to-center distance of the alumina "primary" particles once they were about 10 nm in diameter at lower temperatures.) What is not yet clear from these studies is the nature (Brownian?), see, e.g., Refs. 37 and 38) of the restructuring process responsible for rapidly producing apparently dense ( $D_f \approx 3$ ) spherules of the order of 10 nm, even at temperatures as low as 500 K (see Figs. 2 and 5) from  $\text{Al}_2\text{O}_3$  "monomers" (initially of diametric amount.

also illustrates that if  $\xi = O(1)$ , the hydrolysis time<sup>3</sup> is very short, and delayed "monomer" release or TMA CVD-particle growth can be considered to have insignificant effect on follow-on particle evolution processes. Moreover, flow times in this flame are high enough to allow the other chemical and physical processes to occur without strong coupling to the local gas dynamics. Thus, the chemistry of TMA hydrolysis (to produce  $\text{Al}_2\text{O}_3$  "monomers") and the dynamical response of all aggregates ultimately produced (by coagulation and restructuring) in this CDF is virtually "instantaneous."

We conclude that this laboratory environment and approach lends itself to a quantitative understanding of interesting flame-synthesized inorganic nanoparticles [39]. Systematic modification of the characteristic times associated with "monomer" formation, aggregate formation/coagulation, and restructuring, and flow can be used to control the size and morphology of such flame-synthesized materials. In our follow-on studies, we will explore a broader range of seedbed flame conditions and examine in greater detail those restructuring and coagulation processes responsible for the observed apparent "primary" particle diameters.

## SUMMARY AND CONCLUSIONS

The morphological evolution of inorganic aggregates due to formation/growth/coagulation/sintering processes in a well-defined laminar flame environment was studied using both ex situ thermophoretic sampling/transmission electron microscope (TEM) and in situ laser light scattering techniques.  $\text{Al}_2\text{O}_3$  particles synthesized in a trimethylaluminum (TMA)-seeded counterflow diffusion flame (CDF) fueled with  $\text{CH}_4/\text{O}_2/\text{N}_2$  were used as the model material/combustion system. Aggregate morphology was characterized in terms of "primary" particle size, aggregate size and fractal structure. The effects of temperature and precursor concentration on particle/aggregate morphology were also investigated systemati-

1. Mean "primary" particle diameters were measured to be in the range of 13 to 47 nm, generally increasing with sampling position (increasing residence time) and with TMA concentration. The final alumina products near the particle stagnation plane (PSP) were mostly single particles with diameters up to 60 nm, resulting from the complete "collapse" of the aggregates.
2. Mean number of particles per aggregate increased from unity near particle inception plane (PIP) to maximum values of 15 to 27 at  $z = 4$  mm, after which  $\bar{N}$  decreased monotonically down to about unity at  $z = 8$  mm near PSP. Generally, an increase in the TMA seed level by 8-fold resulted in an corresponding increase of about 100% in  $\bar{N}$ .
3. Fractal dimension,  $D_f$ , and prefactor,  $k_f$ , values for alumina aggregates with negligible sintering rates were found to be 1.52 and 2.4, respectively, relatively insensitive to both sampling position and TMA seed level in the CDF. The fractal dimension increased to 3 as the aggregates restructured into spherical forms due to sintering/coalescence rate process, which seemed to have relatively small effect on the fractal prefactor.
4. The in situ light scattering measurements provide clear evidence regarding the morphology evolution of alumina from a "burst" of individual particles to aggregates due to rapid Brownian-diffusion-driven coagulation ( $PIP < z < 2.5$  mm), aggregate restructuring due to the competition between coagulation and sintering ( $2.5 \text{ mm} < z < 5.5 \text{ mm}$ ), and from aggregates to mostly larger single (coalesced) particles due to high temperature (ca. 1900 K) sintering ( $5.5 \text{ mm} < z < PSP$ ).
5. The above-mentioned observations are shown to be compatible with our assessment of the characteristic times associated with

<sup>4</sup> Water vapor concentration is assumed to be stoichiometric amount.

<sup>3</sup> Sintering due to grain boundary diffusion is not included since it has a similar form to surface diffusion. Besides, alumina particles synthesized in flames are found to be amorphous [35, 36] so that an ordinary grain boundary characterizing two adjacent different crystal lattices does not exist.

each of these chemical and physical processes. Indeed, these nanoparticles are able to restructure (collapse) by a condensed state diffusion-sintering process despite the fact that the peak flame temperature never reached the equilibrium melting point of crystalline  $\text{Al}_2\text{O}_3$ . However, surface-energy-driven viscous flow restructuring was evidently too slow to prevent "fractal" aggregate formation even between 800 and 1800 K in this TMA-seeded CDF.

*This research was sponsored by AFOSR Grant No. 94-1-0143 with J. M. Tishkoff serving as Technical Monitor; and the Yale High Temperature Chemical Reaction Engineering Laboratory Industrial Affiliates: DuPont and ALCOA. The authors would like to thank D. Atugot for the initial design of experimental apparatus, P. Tandon for his recent computational predictions of CDF structure, and C. S. McEnally for improving the accuracy of our thermocouple measurements of temperature.*

#### REFERENCES

- Ulrich, G. D., and Subramanian, N. S. *Combust. Sci. Technol.*, 17(119-126) (1977).
- Heble, J. J., and Sardam, A. F. *J. Colloid Int. Sci.* 128:348-362 (1989).
- Zachariah, M. R., Chin, D., Semerjian, H. G., and Katz, J. L. *Combust. Flame* 78:287-298 (1989).
- Katz, J. L., and Hung, C.-H. *Combust. Sci. Technol.* 82:169-183 (1992).
- Inaki, R., and Boitet, R. *Aggregation and Fractal Aggregates*, World Scientific, Singapore, 1987.
- Felder, J., *Fractals*, Plenum, New York, 1988.
- Rosner, D. E., and Tandon, P. *AIChE J.* 40:167-1182 (1994).
- Tandon, P., and Rosner, D. E. *Chem. Eng. Comm.*, in press.
- Chung, S.-L., and Katz, J. L. *Combust. Flame* 61:271-284 (1985).
- Ebbines, R. A., and Megaridis, C. M. *Langmuir* 3:254-259 (1987).
- Rosner, D. E., Mackowski, D. W., and Garcia-Ybarra, P. *Combust. Sci. Technol.* 80:87-101 (1991).
- Gomez, A., and Rosner, D. E. *Combust. Sci. Technol.* 89:335-362 (1993).
- Katz, J. L., and Miguel, P. F. *NanoStructured Mater.* 4:551-557 (1994).
- Miguez, P. F., Ph.D. thesis, Johns Hopkins University, 1995.
- Köylü, Ü. Ö., Xing, Y., and Rosner, D. E., *Langmuir* 11:4848-4854 (1995).
- Meakin, P., Dunn, B., and Mulholland, G. W., *Langmuir* 5:510-518 (1989).
- Rogak, S. N., and Flagan, R. C. *Amrod Sci. Tech.* 18:25-47 (1993).
- Köylü, Ü. Ö., Feth, G. M., Faith, T. L., and Carvalho, M. G. *Combust. Flame* 106:621-633 (1995).
- Neimark, A. V., Köylü, Ü. Ö., and Rosner, D. E. *J. Colloid Int. Sci.*, in press.
- Megaridis, C. M., and Dobbins, R. A. *Combust. Sci. Technol.* 71:95-109 (1990).
- Köylü, Ü. Ö., and Feth, G. M., *Combust. Flame* 89:140-156 (1992).
- Schmidt-Ott, A. *Appl. Phys. Lett.* 52:954-956 (1988).
- Köylü, Ü. Ö., and Faith, G. M. *J. Heat Transf.* 116:152-159 (1994).
- Rosner, D. E., *Transport Processes in Chemically Reacting Flow Systems*, Butterworths, Boston, 1986 (1990, third printing).
- Moore, J. W., and Pearson, R. G. *Kinetics and Mechanism*, Wiley, New York, 1981.
- Hidy, G. M., and Brock, J. R. *Dynamics of Aerocolloidal Systems*, Pergamon, New York, 1970.
- Mulholland, G. W., Samson, R. J., Mountain, R. D., and Ernst, M. H. *Energy Fuels* 2:481-486 (1988).
- Masonikas, T., and Friedlander, S. K. *J. Colloid Int. Sci.* 146:495-506 (1991).
- Friedlander, S. K., *Smoke, Dust, and Haze*, Wiley, New York, 1977.
- Kinney, W. D., Bowen, H. K., and Uhlmann, D. R., *Introduction to Ceramics*, Wiley, New York, 1976.
- Coleman, W. S., Dynys, J. M., Cannon, R. M., and Coble, R. L. *Matér. Sci. Res.* 3:141-157 (1980).
- Frenkel, J. J. *J. Phys.* 9:385-391 (1945).
- Cai, J., and Sorenson, C. M., *Phys. Rev. E* 50:3397-3400 (1994).
- Xing, Y., Köylü, Ü. Ö., Tandon, P., and Rosner, D. E., *Fifth World Congress of Chemical Engineering*, Paper No. 802, San Diego, 1996.
- Frenkel, J. J., Juliet, F., Merlandau, P., Teicher, S. J., and Vergnon, P. *J. Colloid Int. Sci.* 39:75-89 (1972).
- Wu, M. K., Wideler, R. S., Steiner, C. K. R., Boris, T., and Friedlander, S. K., *Aerosol Sci. Technol.* 19:327-348 (1993).
- Formenti, M., Juillet, F., Merlandau, P., Tandon, P., and Rosner, D. E., *AAAR Twelfth Annual Meeting*, Paper No. 8D4 (1993).
- Tandon, P., and Rosner, D. E., *J. EC Res.* 34:3265-3277 (1995).
- Zachariah, M. R., and Semerjian, H. G., *AIChE J.* 35:2003-2012 (1989).
- Mole, T., and Jeffrey, E. A., *Organohalogenium Compounds*, Elsevier, Amsterdam, 1972.
- Dynes, J. M., Coble, R. L., Coblenz, W. S., and Cannon, R. M., *Mater. Sci. Res.* 13:391-404 (1980).
- Kluger, W. D., *Property Measurements at High Temperature*, Wiley, New York, 1959.
- Cannon, R. M., Rhodes, W. H., and Heuer, A. H. *J. Am. Ceram. Soc.* 62:46-53 (1980).
- Turdogan, E. T., *Physicochemical Properties of Molten Slags and Glasses*, The Metals Society, London, 1983.

Received 20 September 1995; revised 7 December 1995

# REPORT DOCUMENTATION PAGE

Form Approved  
OMB No. 0704-0188

Public reporting burden for the collection of information is estimated to average 1 hour per response, including the time for reviewing instructions, searching existing data sources, gathering and maintaining the data needed, and completing and reviewing the collection of information. Send comments regarding this burden estimate or any other aspect of the collection of information, including suggestions for reducing this burden, to Washington Headquarters Services, Directorate for Information Operations and Reports, 1215 Jefferson Davis Highway, Suite 1200, Arlington, VA 22202-4302, and to the Office of Management and Budget, Paperwork Reduction Project (0704-0188), Washington, DC 20503.

1. AGENCY USE ONLY (Leave blank)			2. REPORT DATE <b>1996</b>	3. REPORT TYPE AND DATES COVERED <b>Reprint</b>	
4. TITLE AND SUBTITLE <b>Jump, Slip, and Creep Boundary Conditions at Nonequilibrium Gas/Solid Interfaces<sup>†</sup></b>			5. FUNDING NUMBERS  PE - 61102F PR - 2308 SA - BS G - F49620-94-1-0143		
6. AUTHOR(S)  Daniel E. Rosner and Dimitrios H. Papadopoulos			8. PERFORMING ORGANIZATION REPORT NUMBER		
7. PERFORMING ORGANIZATION NAME(S) AND ADDRESS(ES)  Yale University High Temperature Chemical Reaction Engineering Laboratory Department of Chemical Engineering PO Box 208286 YS, New Haven, CT 06520-8286 USA			10. SPONSORING/MONITORING AGENCY REPORT NUMBER		
9. SPONSORING/MONITORING AGENCY NAME(S) AND ADDRESS(ES)  AFOSR/NA 110 Duncan Avenue, Suite B115 Bolling AFB DC 20332-0001			12b. DISTRIBUTION CODE		
11. SUPPLEMENTARY NOTES  <i>Ind. Eng. Chem. Res. 1996, 35, 3210-3222</i>					
12a. DISTRIBUTION/AVAILABILITY STATEMENT  Approved for public release; distribution is unlimited			13. ABSTRACT (Maximum 200 words)  The notion of <i>local</i> (dynamical, thermal, and chemical) <i>equilibrium</i> at fluid/solid interfaces which are the site of interesting <i>nonequilibrium</i> processes has proven useful to engineers for nearly a century and provides the basis for widely used methods described in textbooks on <i>Transport Processes</i> . Indeed, <i>continuity</i> of tangential velocity ("no-slip"), temperature, and species chemical potential are usually treated as "commandments", rather than often-useful approximations! However, in many current and emerging applications this class of approximations becomes unacceptable for easily understood reasons. We illustrate this here for <i>ideal gas/solid interfaces</i> across which, or tangent to, there are nonzero molecular fluxes of momentum, energy, and/or species mass. We make use of the concept of a <i>Knudsen sublayer</i> , at most several gaseous mean-free paths thick, inevitably present adjacent to the solid surface. While many scientific aspects of these phenomena have been known since the earliest studies of J. C. Maxwell (1879), we show that their engineering importance is now such that their understanding should be part of the education of all chemical engineers. Moreover, molecular-level numerical techniques can now be brought to bear to illuminate the nature of these near-interfacial regions, under more realistic nonequilibrium circumstances. Analogous phenomena occur in <i>dense vapor/solid</i> and <i>liquid/solid</i> cases. Such systems, far less well understood theoretically, are characterized by effects which are smaller numerically but which may still be quite exploitable (as for separations (Giddings, 1991; Caldwell, 1988)).		
14. SUBJECT TERMS  boundary conditions, gas/solid interfaces, thermal creep, temperature jump, Knudsen sublayer, accommodation coefficients			15. NUMBER OF PAGES <b>13</b>		
16. PRICE CODE			17. SECURITY CLASSIFICATION OF REPORT Unclassified		
18. SECURITY CLASSIFICATION OF THIS PAGE Unclassified			19. SECURITY CLASSIFICATION OF ABSTRACT Unclassified		
20. LIMITATION OF ABSTRACT UL					

## Jump, Slip, and Creep Boundary Conditions at Nonequilibrium Gas/Solid Interfaces<sup>1</sup>

卷之三

High Temperature Chemical Reaction Engineering Department,  
Chemical Engineering Department,  
Dimitris H. Raptopoulos  
Daniel E. Rosner, and Dimitris H. Raptopoulos

The notion of *local* (dynamical, thermal, and chemical) equilibrium at fluid/solid interfaces which are the site of interesting nonequilibrium processes has proven useful to engineers for nearly a century and provides the basis for widely used methods described in textbooks on *Transport Processes*. Indeed, continuity of tangential velocity ("no-slip"), temperature, and species chemical potential are usually treated as "commandments" rather than often-useful approximations! However, in many current and emerging applications this class of approximations becomes unacceptable for easily understood reasons. We illustrate this here for *ideal gas / solid interfaces* which, or tangent to, there are nonzero molecular fluxes of momentum, energy, and/or species mass. We make use of the concept of a Knudsen sublayer, at most several nanometers thick, inevitably present adjacent to the solid surface. While many scientific aspects of these phenomena have been known since the earliest studies of J. C. Maxwell (1879), we believe that their engineering importance is now such that their understanding should be part of the education of all chemical engineers. Moreover, molecular-level numerical techniques can now be brought to bear to illuminate the nature of these near-interfacial regions, under more realistic nonequilibrium conditions. Analogous phenomena occur in *dense vapor / solid* and *liquid / solid* cases. Such systems, far less well understood theoretically, are characterized by effects which are smaller numerically but which may still be quite exploitable (as for separations

Instrumentation

The continuity of tangential velocity ("no-slip"), temperature, and Gibbs chemical potentials across interfaces between phases is so deeply ingrained in the psyche of engineers that certain pitfalls and missed opportunities are inevitable in dealing with nonequilibrium applications of current importance. This is especially true for either gaseous systems at subatmospheric pressure or systems with small dimensions, on which we focus here. Because of the current importance of "dry" semiconductor processing reactors (for selective etching, chemical vapor deposition local-dosing, ...), and emerging "nanotechnologies" (synthesis and unique properties of solid materials at the atomic or 10 nm scale), it would be prudent for chemical engineers to understand the conditions under which the above-mentioned continuity of tangential velocity, temperature, and Gibbs chemical potentials break down and the engineering consequences thereof. Because  $\text{C}_6\text{H}_6$  appears to have little difficulty with the concept of chemical species' nonequilibrium<sup>1</sup> at gas/catalyst solid interfaces (because very low chemical reaction probabilities are the rule rather than the "exception"),

our examples, starting with the most familiar, will deal with drug reduction, heat transfer reduction, particle thermophoresis (Kroesen et al., 1991), and convection driven by nonisothermal walls in crystal growth amorphous gels (Boerner, 1889; Papadopoulou and Rausch, 1985). In all cases we will emphasize ideal gas systems satisfying the necessary conditions:  $\frac{l_1}{l_2} \gg \frac{n_1}{n_2} \gg \frac{\sigma_1}{\sigma_2} \gg 1$ , where  $l_i$  is the gas molecule mean-free path,  $n_i$  is the gas number density ( $\text{molecules}/\text{cm}^3$ ), and  $\sigma_i$  is the effective molecular diameter. Moreover, we focus on the near-continuum limit in which  $l_i$  is much smaller than the

This paper will be structured as follows. In section 2 we consider the momentum, energy, and mass-transfer consequences of the thin Knudsen sublayer when there is a molecular transport across the interface (i.e., in the direction of the outward normal; Figure 1), associated with the gradient of all field variables in that direction. Section 3 deals with the considerable less familiar case of large deviations from the

© 1998 American Chemical Society

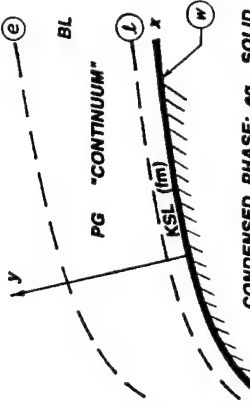


**Figure 1.** Configuration considered and station nomenclature. A boundary layer (BL) and Kondraten sublayer (KSL) adjacent to a solid surface exchanging momentum, energy, and/or species mass with a moving "perfect" (ideal) gas (PG);  $L > \delta$ ;  $\eta - \eta_0 > c$ . Concentration gradients tangent to the surface, outlining old and new approaches to deriving the associated tangential and "creep" velocities. Section 4 describes several instructive applications in which these KSL phenomena have important macroscopic consequences, even in the near-contaminant ( $Kn = L_0/\delta_L \ll 1$ ) limit. Section 5 concludes with necessary generalizations of these results, methods, and the "lessons" to be learned from these "old" and "new" examples.

## 2. Slip and Jump Boundary Conditions:

**Dimensional rules across interfaces**

As indicated above, a troublesome question for most engineering students and designers, and one with which, we believe, they have not been adequately prepared to deal, is the question of when "local equilibrium" can be assumed to prevail at interfaces, even in the presence of nonequilibrium phenomena—*i.e.*, in the presence of nonzero fluxes of tangential momentum, energy, and/or species mass. In most textbooks one finds the usual "commandments" such as the no-slip condition (of classical viscous fluid mechanics) or continuity of temperature between phases, leaving the student with the false impression that these postulates stand on an equal footing with the principles of conservation of mass, momentum, and energy. Corollaries of this confusion are the inability to assess when these commandments will lead one far astray and an inability to deal with nonequilibrium physicochemical situations in which such field variables as the tangential velocity, temperature, and chemical potentials undergo significant jumps across the interface (Roemer, 1976, 1986). We discuss here the types of systems in which such jumps can be expected and how these inevitable jumps depend on the net transport fluxes across, or tangent to, the interfacial region. We acquaint the reader with the important notion that interfaces, like bulk phases, have transport properties and associated transport resistances. We deliberately demonstrate these concepts below in very simple terms for perhaps the best understood interfacial region—air, that comprised of the so-called Knudsen sublayer (with thickness on the order of a few gas mean-free paths) which inevitably exists between a gaseous continuum and an adjacent condensed (*e.g.*, smooth, impenetrable solid) phase continuum. It is hoped that this elementary presentation clarifies the essential points and will facilitate the incorporation of this subject matter in engineering courses on momentum, energy, and/or mass transport.

## **2.1. Jump Conditions at a Gas/Solid Interface**

$$r_{yx} = -\mu \frac{\partial v_i}{\partial y} \quad (2-1)$$

$$d'' = -k \frac{\partial T}{\partial x} = -\frac{c_p}{2} \mu \frac{\partial T}{\partial x} \quad (2-2)$$

卷之三

where  $\eta$  is the gas viscosity ( $(\kappa/(12\pi D))^{\frac{1}{2}}$ ),  $k_T$  is the gas thermal conductivity, and  $D_i$  is the Fick diffusivity for chemical species  $i$  ( $i = A, B, \dots$ , and, for simplicity, we neglect interchemical vapor mass transfer).

2.3. Net Transport across a thin Knudsen Sublayer: The net fluxes across a thin (Knudsen) planar boundary are governed by laws of a different kind (see, e.g., Edwards *et al.*, 1978, who assume  $\alpha = 1$ ):

where  $Z^2$  ( $= (1/4\pi)r^2$ ) is the local flux of all molecules in one direction across each area (e.g., in the "plane") =  $\alpha$ , and the  $\alpha$  values, defined by these equations, describe the nature of the gaseous molecule interactions with the solid surface, i.e.,  $\alpha_1$  = molecule/interface momentum accommodation coefficient ( $0 \leq \alpha_1 \leq 1$ ),  $\alpha_2$  = molecule/interface thermal accommodation coefficient ( $0 \leq \alpha_2 \leq 1$ ),  $\alpha_{\infty}$  = molecule/interface normalizations accommodation coefficient ( $0 \leq \alpha_{\infty} \leq 1$ ). These constants are accessible to measurement and, in some

effective (molar) heat capacity  $C_p - (R/2)$  appearing in eq 2-5. This is a consequence of the fact that the average translational kinetic energy of the molecules crossing each plane  $y = \text{const.}$  is  $2k_B T/2$  per molecule (not  $(3/2)k_B T$ ; see, e.g., Edwards *et al.*, 1979; section 6.6.9) and has interesting consequences when applied to exogenic surface reactions at low densities (Kiel *et al.*, 1984). Equations 2-5, as written, allow for the transport of energy beyond translational—*i.e.*,  $C_p \geq (5/2)R$ , in which case  $\alpha_{\text{in}}$  is an overall effective energy accommodation coefficient. Finally, we remark that eq 2-6 neglects minor complications associated with simultaneous heat transfer.

**2.4. "Matching" the Gas BL to the KSL.** Suppose the Knudsen sublayer is sufficiently thin, or the surface sufficiently flat, that, by conservation, the fluxes\* of tangential momentum, energy, and species mass are the same across the G/KSL and KSL/solid "interfaces". Then, since we can assume the field variables themselves are continuous across  $y = l_f$ , we can write:

$$( -\gamma_y )_G = ( -\gamma_y )_{\text{KSL}} \quad (2-7)$$

$$(q_y')_G = (q_y')_{\text{KSL}} \quad (2-8)$$

$$(J_y)_G = (J_y)_{\text{KSL}} \quad (2-9)$$

Each of the field variables evaluated at  $y = l_f$  (*cf.* eqs 2-4–2-6) can be expressed in terms of its value at (*projected to*)  $y = 0$  via a (truncated) Taylor series:

$$v_i(l_f) = v_i(0^+) + \left(\frac{\partial v_i}{\partial y}\right)_{y=0} l_f + \text{h.o.t.} \quad (2-10)$$

with similar estimates for  $T$  and  $y$ . Combining these relations and solving for the corresponding nonequilibrium jumps, we readily find the local "slip's" (jump) boundary conditions:

$$v_i(0^+) = \left(1 - \frac{1}{2}\alpha_{\text{in},i}\right) \left(2l_f\right) \left(\frac{\partial v_i}{\partial y}\right)_{y=0} \quad (2-11)$$

$$T_y - T(0^+) = \left(1 - \frac{1}{2}\alpha_{\text{in},y}\right) \left(2l_f\right) \left(-\frac{\partial T}{\partial y}\right)_{y=0} \quad (2-12)$$

$$y_{i,*}(0^+) = \left(1 - \frac{1}{2}\alpha'_{i,*}\right) \left(2l_f\right) \left(-\frac{\partial y_i}{\partial y}\right)_{y=0} \quad (2-13)$$

where

$$\alpha'_i = \alpha_i \left(\frac{\gamma+1}{2}\rho_f\right) \quad (2-14)$$

$$\alpha'_{i,*} = Sc_i \left(\frac{m}{m_i}\right)^{1/2} \alpha_{\text{in},i} \quad (2-15)$$

This level of approximation will be sufficient for the following purposes.

**2.4. Conclusions Regarding Discontinuities at the G/S Interface.** It is now instructive to introduce the gaseous boundary layer "slope" thicknesses:  $\delta_{\text{max}}$ ,  $\delta_0$ , and  $\delta_1$ , defined by the analogous expressions:

$$\left(\frac{\partial v_i}{\partial y}\right)_{y=0} = \frac{U - u_i(0^+)}{\delta_{\text{max}}} \quad (2-16)$$

$$Nu = \frac{Nu(0^+)}{1 + \text{const.}Kn_f Nu(0^+)} \quad (2-24)$$

### 2. "Creep" Conditions: Energy and/or Mass Diffusion Fluxes Parallel to Surfaces

Less familiar, but of growing importance, are systems in which appreciable energy and/or mass diffusion fluxes occur parallel to the solid surface.

**3.1. Thermal Creep.** The first example of this type was pointed out as early as 1879 by J. C. Maxwell in explaining both the popular "thermometer" effect and O. Reynolds' experimental observations on nonisothermal "gas blanket" gas flow (*see, e.g.*, Brush and Everitt, 1989). Without a detailed KSL analysis Maxwell demonstrated that, if  $T(x, 0^+)$  is nonuniform along a surface and  $\alpha_{\text{in},i} = 0$ , this must necessarily be associated with a tangential mass-averaged velocity (directed from cold-to-hot) of about:

$$v_i(0^+) = U_{\text{tw}} = (3/4)\nu_f (3 \ln T_{\text{tw}}/\partial x) \quad (3-1)$$

(*see, e.g.*, Kennard, 1938, who comments that "molecules impinging obliquely upon it (the nonisothermal solid surface) strike it with higher average velocity when they come from the hotter region than when they come from the colder, and so are kicked back more strongly by the wall ... with the result that the gas acquires tangential momentum directed toward the hotter side"). Here, as before,  $\nu_f$  is the momentum diffusivity ("kinematic viscosity",  $\mu/\rho$ ) of the gas, approximately given by  $(12/7)\epsilon_f^2 n$ , where  $\epsilon_f$  is the mean thermal speed of the gas molecules. More refined KSL structure analyses based on a linearized Boltzmann equation led to theoretical "creep velocity" results of the same order of magnitude but with the numerical constant  $\nu_f$  replaced by a dimensionless coefficient,  $C_f$ , weakly dependent upon both  $\alpha_{\text{in},i}$  (TMAC) and the nature of the gas intermolecular force law (*see, e.g.*, Kegan, 1973; Loyalka and Cipolla, 1971). The tangential thermal creep velocity ( $C_f$ ) must be added to (or subtracted from) the "asymmetric slip velocity" presented in section 2.2, "particle thermophoresis". The second deals with circulatory flows induced (even in the absence of gravity) in nonisothermal vapor ampules used to grow crystals.

**3.2. Concentration Creep.** The species mass-transfer analog of thermal creep is, as might be expected, associated with concentration gradients along solid surfaces. For binary mixtures this was apparently first pointed out and estimated (for Maxwell molecules and diffuse reflection,  $\alpha_{\text{in},i} = 1$ ) by Kramers and Kistemaker (1943) and subsequently refined by, among others, Loyalka (1971) and Mason and Chapman (1982). These authors provide expressions for the dimensionless diffusional creep coefficient  $C_{12}$ , appearing in:

$$V_i(0^+) = C_{12} D_{12} (\partial \ln Y_i / \partial x)|_{y=0} \quad (3-2)$$

where  $D_{12}$  is the Fick binary diffusion coefficient,  $Y_i$  is the mole fraction of species  $i$ , and, for a given intermolecular force law, we expect

where const. =  $2(1 - (1/2)\alpha)/\alpha$ ,  $\alpha = \alpha_{\text{in},i}$ ,  $\alpha'_i$ ,  $C_f$  is a dimensionless friction factor (Toussaint, 1986),  $Nu$  =  $Nu_{\text{in}}$  for heat or mass transfer, respectively (Roemer, 1986),  $Kn$  is based on the same reference length used in the definition of the nondimensional fluxes:  $C_i$ ,  $Nu_{\text{in}}$ , and  $Nu_{\text{out}}$ , and the superscript (0) pertains to the continuum (no-slip) limit, all other conditions being held constant. Some practical consequences of eqs 2-23 and 2-24 will be taken up in section 4.

Concerning our second point, *early* experimental values of  $\alpha_{\text{in},i}$  (TMAC) and  $\alpha_i$  (EAC) (*see, e.g.*, the survey of Schaaf and Chamber, 1988) indicated that they were close to unity ( $0.78 \leq \alpha \leq 1$ ), undoubtedly because they all pertained to surfaces which were either "rough" contaminated with adsorbed gases, and/or pertained to gas/solid systems which did not have sufficiently disparate molecular weights. However, more recent measurements (Saxena and Foote, 1989) as well as theory (*see, e.g.*, Goodman and Wachtman, 1976), indicate that, for sufficiently smooth, clean solid surfaces struck by much lighter (or heavier) gas molecules,  $\alpha$  values much lower than unity are expected and observed. While the lowest TMAC value inferred from Shieff (1983) gas-in-capillary sound-speed measurements was 0.65 (for He/g on clean Pt), he inferred EAC values as low as about 0.07 for this system. For ca. 60% of NH<sub>3</sub>/He molecules reflecting off Ir(0) decomposition catalyst between 1300 and 2100 K, earlier work in this laboratory (Kiel *et al.*, 1984) indicated values of EAC near  $1/4$ . More dramatically, for the He/H<sub>2</sub>/W(s) system EAC  $\approx 0.01$  (Ahara *et al.*, 1987). Clearly, such systems will exhibit large departures from no-slip, no (temperature) jump behavior, even in the near-continuum ( $Kn_f \ll 1$ ) limit (*see, e.g.*, section 4). Of course, if  $Kn_f$  is not small (*e.g.*, O(1)), these slipup effects will render ordinary continuum estimation practically useless.

In closing this section it should be commented that these "accommodation" coefficients  $\alpha_{\text{in},i}$ ,  $\alpha'_i$ ,  $C_f$ , while normalized in the sense that  $\max \alpha = 1$ , are not what might be called "elementary" (step) rate constants. For one thing they represent averages over molecules which arrive from all directions and at all speeds, according to the prevailing (often, non-Maxwellian) molecular velocity distribution function. Similarly the describing velocity distribution function, or scattered molecules are distributed with respect to direction, velocity, and possibly internal state (*see, e.g.*, Halpern and Roemer, 1978; Mantell *et al.*, 1986). Finally, the "act" of tangential momentum transfer, gas/solid energy exchange, and species mass accommodation (equilibration) are often mechanically complex, involving a sequence of (more-or-less) elementary steps, which may include adsorption, surface migration to singular sites, and activated desorption. This implies that the coefficients  $\alpha_{\text{in},i}$ ,  $\alpha'_i$ , and  $C_f$  cannot be expected to be "constants", but can depend on many variables (besides the solid and gas temperatures) that determine adsorbed molecule populations and surface structure (morphology, ...). Nevertheless, there are many practical problems that can be solved at the level of information of these accommodation coefficients (*see, e.g.*, section 4), and these coefficients are far more accessible to direct measurement than the elementary step rate constants underlying them. One highly idealized way of "interpreting" these  $\alpha$  values, which dates back to Maxwell's time and is computationally easy to implement, is the following: of all incident molecules,

inspection of these analogous equations leads to the following important conclusion:

C1. Whenever the diffusion fluxes of tangential momentum  $-\gamma_y$ , energy  $\gamma'_y$ , and/or species mass  $J_{i,*}$  evaluated at the wall ( $y = 0^+$ ) are nonzero (*i.e.*, whenever there is a departure from strict mechanical, thermal, and/or chemical equilibrium), there must be corresponding non-zero jumps in the associated field variables at the gas/solid interface.

C2. Only when  $2Kn_f/(\alpha(1 - (1/2)\alpha)) \ll 1$  do these jumps become negligible, leading to the often-quoted noslip (jump) conditions. Note that  $Kn_f \ll 1$  is *not* sufficient to neglect such a jump if the corresponding "effective accommodation coefficient", a (eqs 2-14 and 2-15), is itself very small (see sections 3 and 4).

C3. When  $\alpha$  is near unity, then the condition  $Kn_f \ll 1$  ensures approximate local equilibrium. In such cases  $\alpha_{\text{in},i}$  can only be important under rarefied (noncontinuum) BL gas flow conditions.

Regarding the effects of accommodation coefficient and Knudsen number (when  $Kn_f \ll 1$ ) on mass-continuum momentum, energy, and mass-transfer rates, since  $Nu_{\text{in}}(0) = L/\delta_0$ , etc., eqs 2-20–2-22 immediately imply the success of correlations of the simple nondimensional form:

$$C_f = \frac{C_f(0)}{1 + \text{const.}Kn_f Re C_f(0)} \quad (2-23)$$

and

This level of approximation will be sufficient for the following purposes.

**2.4. Conclusions Regarding Discontinuities at the G/S Interface.** It is now instructive to introduce the gaseous boundary layer "slope" thicknesses:  $\delta_{\text{max}}$ ,  $\delta_0$ , and  $\delta_1$ , defined by the analogous expressions:

$$irr = 2(1 - (1/2)\alpha)/\alpha, \alpha = \alpha_{\text{in},i}, \alpha'_i, C_f = 2(1 - (1/2)\alpha)/\alpha, \alpha = \alpha_{\text{in},i}, \alpha'_i, C_f$$

$$Nu = \frac{Nu(0^+)}{1 + \text{const.}Kn_f Nu(0^+)} \quad (2-24)$$

where const. =  $2(1 - (1/2)\alpha)/\alpha$ ,  $\alpha = \alpha_{\text{in},i}$ ,  $\alpha'_i$ ,  $C_f$  is a dimensionless friction factor (Toussaint, 1986),  $Nu$  =  $Nu_{\text{in}}$  for heat or mass transfer, respectively (Roemer, 1986),  $Kn$  is based on the same reference length used in the definition of the nondimensional fluxes:  $C_i$ ,  $Nu_{\text{in}}$ , and  $Nu_{\text{out}}$ , and the superscript (0) pertains to the continuum (no-slip) limit, all other conditions being held constant. Some practical consequences of eqs 2-23 and 2-24 will be taken up in section 4.

Concerning our second point, *early* experimental values of  $\alpha_{\text{in},i}$  (TMAC) and  $\alpha_i$  (EAC) (*see, e.g.*, the survey of Schaaf and Chamber, 1988) indicated that they were close to unity ( $0.78 \leq \alpha \leq 1$ ), undoubtedly because they all pertained to surfaces which were either "rough" contaminated with adsorbed gases, and/or pertained to gas/solid systems which did not have sufficiently disparate molecular weights. However, more recent measurements (Saxena and Foote, 1989) as well as theory (*see, e.g.*, Goodman and Wachtman, 1976), indicate that, for sufficiently smooth, clean solid surfaces struck by much lighter (or heavier) gas molecules,  $\alpha$  values much lower than unity are expected and observed. While the lowest TMAC value inferred from Shieff (1983) gas-in-capillary sound-speed measurements was 0.65 (for He/g on clean Pt), he inferred EAC values as low as about 0.07 for this system. For ca. 60% of NH<sub>3</sub>/He molecules reflecting off Ir(0) decomposition catalyst between 1300 and 2100 K, earlier work in this laboratory (Kiel *et al.*, 1984) indicated values of EAC near  $1/4$ . More dramatically, for the He/H<sub>2</sub>/W(s) system EAC  $\approx 0.01$  (Ahara *et al.*, 1987). Clearly, such systems will exhibit large departures from no-slip, no (temperature) jump behavior, even in the near-continuum ( $Kn_f \ll 1$ ) limit (*see, e.g.*, section 4). Of course, if  $Kn_f$  is not small (*e.g.*, O(1)), these slipup effects will render ordinary continuum estimation practically useless.

In closing this section it should be commented that these "accommodation" coefficients  $\alpha_{\text{in},i}$ ,  $\alpha'_i$ ,  $C_f$ , while normalized in the sense that  $\max \alpha = 1$ , are not what might be called "elementary" (step) rate constants. For one thing they represent averages over molecules which arrive from all directions and at all speeds, according to the prevailing (often, non-Maxwellian) molecular velocity distribution function. Similarly the describing velocity distribution function, or scattered molecules are distributed with respect to direction, velocity, and possibly internal state (*see, e.g.*, Halpern and Roemer, 1978; Mantell *et al.*, 1986). Finally, the "act" of tangential momentum transfer, gas/solid energy exchange, and species mass accommodation (equilibration) are often mechanically complex, involving a sequence of (more-or-less) elementary steps, which may include adsorption, surface migration to singular sites, and activated desorption. This implies that the coefficients  $\alpha_{\text{in},i}$ ,  $\alpha'_i$ , and  $C_f$  cannot be expected to be "constants", but can depend on many variables (besides the solid and gas temperatures) that determine adsorbed molecule populations and surface structure (morphology, ...). Nevertheless, there are many practical problems that can be solved at the level of information of these accommodation coefficients (*see, e.g.*, section 4), and these coefficients are far more accessible to direct measurement than the elementary step rate constants underlying them. One highly idealized way of "interpreting" these  $\alpha$  values, which dates back to Maxwell's time and is computationally easy to implement, is the following: of all incident molecules,

streaming part of the equation with a probabilistic evolution of the more complicated (nonlinear) integral collision term. In these simulations, a collection of "particles" is distributed within the chosen computational domain, each particle corresponding to a large number of actual fluid molecules. Subsequently, particles are allowed to interact according to pre-specified rules. Quantities of interest, such as mass-average velocity, temperature, etc., are calculated by locally averaging the collected statistics. Clearly then, information on the microscopic as well as the macroscopic scale is obtained. Advantages of this method include CPU time linearly related to the total number of computational particles (and this allows total particle numbers in the range between  $10^6$  and  $10^8$ , depending on the resources available) and computational domains with macroscopic dimensions, a prerequisite for practical applications. Although the original formalism is limited to dilute gases where gas molecules have finite cross section but occupy negligible volume, newly developed algorithms allow for a generalization of the DSMC algorithm to account for higher density effects, in particular, the excluded-volume effects of the Enskog theory of dense gases (see Alexander *et al.*, 1986).

More generally, Loyalka and Cipolla (1971) had previously shown that the simple Kramers-Kirkemaker expression was reasonable for  $n = 1$  and  $m_1 \gg m_2$  but that  $C_{11k}$  did not necessarily vanish when  $m_1 = m_2$ . While not explicitly discussed below, Annis and Mason (1975) have shown that this form of result can be readily used to predict the physics of aerosol particles in a spatially nonuniform composition gas mixture—*i.e.*, aerosol particle diffusiophoresis, over a broad range of Knudsen numbers,  $1/m_2^{1/2}$ . Another interesting result is that thermophoresis and diffusiophoresis are not simply "additive"—there is a nonzero coupling term estimated by Annis and Mason (1975) using the "dirty-gas" (disperse mass) limit of Enskog-Chapman theory.

### 3.3. Molecular-Level Numerical Simulation Methods

As we have seen, the discontinuities associated with diffusion forces either series or parallel to solid surfaces in gaseous systems arise from the existence of Knudsen sublayers within which the continuum approximation fails since the length scale characterizing these layers is the local mean-free path. However, as one moves sufficiently far from the boundary (*i.e.*, several mean-free paths away), the continuum approximation becomes valid, so that fluid flow can usually be described by the well-known macroscopic differential balance equations (*e.g.*, Navier-Stokes equations and associated total mass, heat, and species mass balance equations incorporating linear diffusion flux laws). Knudsen sublayer problems have been successfully attacked in the past using analytical/numerical techniques within the framework of the linearized Boltzmann equation for the one-particle distribution function. Unfortunately, mathematical complications call for drastic simplifications for progress to be made. Typically, approximations involve linearization of governing equations (and boundary conditions), one-dimensional geometry, and model kinetic equations (*e.g.*, the BGK linearized collision operator model). The latter limitation has been removed in more recent numerical implementations of such schemes (*e.g.*, Loyalka, 1989). Nevertheless, very useful results have been obtained which, apart from serving their primary purpose, can be invoked as limiting-case benchmarks in validating more general kinetic schemes. With the advent of high-speed computing, attractive alternatives have indeed emerged—particle-level simulation methods.

Microparticle simulations of dilute gases have chiefly been pursued by employing direct simulation Monte Carlo methods, hereafter abbreviated DSMC (Bird, 1994). In DSMC, the governing Boltzmann equation is attached by combining a deterministic treatment of the concentration gradient of a steady-state concentration gradient in a certain direction. Our work (see Papadopoulos, 1996; Papadopoulos and Ronner, 1995, 1996) regarding the effects of thermal creep in enclosure flows often encountered in crystal growth

applications is reviewed in section 4.4. Here we merely mention that such simulations can successfully model two-dimensional geometries of macroscopic dimensions with arbitrary collision dynamics and appreciable gradients irrespective of the flow Knudsen number (*i.e.*, though, the true continuum limit ( $Kn \ll 1$ ) is neither interesting nor computationally attractive). The second of the two major categories of particle simulations, called molecular dynamics (MD), is a deterministic scheme in which the equations of motion governing classical particles are numerically integrated in time. Domain dimensions and integration time steps are inherently limited by the prevailing molecular dimensions and collision times, respectively. The established procedure is to invoke similarity arguments to extract macroscopic behavior from such microscopic simulations. Both liquids and fluid densities corresponding to dense gases can be simulated, but potential pitfalls exist in the simulation of dilute gases where excluded-volume effects are negligible (Bird, 1987). The important question of when the "no-slip" condition is justifiable for dense fluid systems has received well-deserved attention from the MD community. MD simulations of Couette and Poiseuille liquid flows by Koplik *et al.* (1989) have demonstrated that the no-slip condition is established as a consequence of solid surface roughness on the molecular scale. However, at lower fluid densities they reported velocity slip associated with velocity gradients normal to the bounding walls. This slip was also found to be independent of the particular type of flow and well-predicted using analyses based on slip-length arguments. Interestingly enough, the authors proposed that previous theoretical difficulties regarding moving contact lines between two immobile fluids can be remedied by relaxing the no-slip condition in the seemingly singular region. Related studies by Mo and Rosenberger (1990) on the effect of various roughness models on slip conditions suggested the relevance of a Knudsen number based on mean roughness height. Because MD has proven to be a valuable tool in exploring the supercritical fluid regime under equilibrium and near-equilibrium conditions (see, *e.g.*, Kincaid *et al.*, 1992), very likely it can be used to investigate jump and creep phenomena in dense fluid systems near solid boundaries. This task has evidently not been undertaken to date, perhaps because of the above-mentioned difficulties related to velocity-scale resolution and thermal noise.

**4. Applications and Implications**

Some important examples in which slip, jump, and creep phenomena influence macroscopic transport rates even in the near-continuum limit ( $Kn \ll 1$ ) are indicated below.

**4.1. Drag and "Stopping Time" of a Suspended Solid Spherical Particle. For  $Re \ll 1$  near-continuum flow about a solid sphere, Bassett (1986) derived a result equivalent to:**

$$C_{11} = (C_D)_{\text{Stokes}} / C_{\text{slip}} \quad (4-1)$$

where  $(C_D)_{\text{Stokes}} = 24/Re$  is the well-known Stokesian (no-slip) drag coefficient, and  $C_{\text{slip}}$  is the corresponding correction factor ( $> 1$ ) for nonzero slip:

$$C_{\text{slip}} = \frac{1 + 12[(1 - \frac{1}{2}\alpha_{\text{max}})/\alpha_{\text{max}}]Kn_4}{1 + 8[(1 - \frac{1}{2}\alpha_{\text{max}})/\alpha_{\text{max}}]Kn_4} \quad (4-2)$$

Expanding this for small  $Kn_4$  gives

$$C_{\text{slip}} \approx 1 + 4[1 - \frac{1}{2}\alpha_{\text{max}}]/\alpha_{\text{max}}]Kn_4 + \text{h.o.t.} \quad (4-3)$$

Comparison of this result with the functional form of  $C_{\text{slip}}(Kn_4)$  recommended by Millikan (1923) (for the entire Knudsen range), viz.:

$$C_{\text{slip}} = 1 + 2Kn_4[A_1 + A_2 \exp(-A_3/Kn_4)] \quad (4-4)$$

shows that:

$$A_1 \approx 2[(1 - \frac{1}{2}\alpha_{\text{max}})/\alpha_{\text{max}}] \quad (4-5)$$

*i.e.*,  $A_1$  is  $\alpha_{\text{max}}$ -dependent\*, not (necessarily) the constant 1.26 cited in the literature based on Millikan's careful oil drop experiments. Clearly, then, the all-important particle stopping (relaxation) time,  $t_s$  (Friedlander, 1977; Fernández de la Mora and Rosner, 1981, 1982; Rosner, 1986; Konstandopoulos and Rosner, 1995), is given by:

$$t_s = [(\rho_B T/m_p)/(18\rho)]/[C_{\text{slip}}(Kn_4/\alpha_{\text{max}})] \quad (4-6)$$

where the dependence on  $\alpha_{\text{max}}$  is now highlighted. Note that this will affect the familiar "sedimentation" velocity,  $g_p$ , as well as the Brownian diffusion coefficient,  $D_p$ , which, according to Einstein, can be expressed as

$$D_p = [k_B T/m_p]^{1/2}/\rho_p \quad (4-7)$$

Even for, say,  $Kn_4 = 1/10$ , with  $TMAc = 0.05$  (the He- $(gVPh)$  system),  $t_s$  and  $D_p$  are increased by 26% over the Stokesian values.

As a historical note, we remark that the first major engineering applications of "slip-induced drag reduction" in fields of "vacuum" flow system design (now of even greater importance to chemical, mechanical, and electrical engineers because of the solid-state microelectronic industry) and "high"-altitude aerodynamics (Thin, 1948), both subsonic and supersonic. These activities spawned the *Rarefied Gas Dynamics Symposia*, 19 of which proceedings are available covering the period 1958 to the present. In 1965, Kavanagh experimentally verified the success of the  $Nu_2$ -correlation form given by eq 2–24, where  $Nu_2$  is the Nusselt number based on  $T_c - T_s$  and sphere diameter  $d$ , and the dimensionless "constant"  $2(1 - 1/2\alpha_{\text{max}})Kn_4$  was determined by matching the experimental data (see, *e.g.*, Fuchs and Chambre, 1958). The approach of Fuchs and Sutugin (1970), which considers the RSL to be a thermal resistance in series with the continuum "outer" gas layer, as expected, leads to the same result as eq 2–24 in the small  $Kn$  limit. Using the  $\text{General}_{\text{Stokes}}$  code,  $Nu_2$  value leads to startling conclusions; *e.g.*, for a system like  $Hg/Py/W(s)$  with  $\alpha_{\text{max}} \approx 0.005$ ,  $y = 5$ ,  $P_r = 5/6$ , even at  $Kn_4 = 1/10$  the heat-transfer coefficient  $Nu_2$  will be reduced by a factor of about 1/6 (see also, Ahara *et al.*, 1967). For example, on this same basis we expect that many "radiation-corrected" thermocouple temperature measurements in combustion gases (often made using alloys of Pt and/or Ir) are systematically too low because of failure of the investigators to take into account this important "temperature jump" phenomenon.

**4.2. Suspended Particle Thermophoresis in Gases.** Even allowing for slip associated with low  $\alpha_{\text{max}}$ , the Brownian diffusivity (eq 4–7) of suspended aerosol

\*  $\alpha_{\text{max}} = C_{11}(m_1/m_2)^{1/2} / (y_1 + y_2(m_1/m_2)^{1/2})$

where  $C_{11}(m_1/m_2)^{1/2} = 24/Re$  is the well-known Stokesian (no-slip) drag coefficient, and  $C_{\text{slip}}$  is the corresponding correction factor ( $> 1$ ) for nonzero slip.

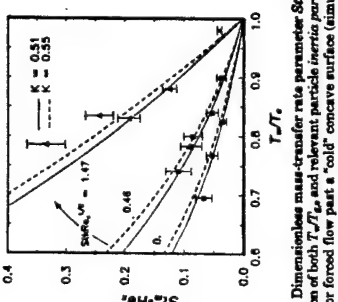


**Figure 8.** Dimensionless mass transfer rate parameter  $Sc/Re_0$  as a function of inertia  $T_e/T_p$  and relevant particle inertia parameter  $Sc/Re_0$  for forced low part a cold concave surface (simulating the pressure side of a combustion turbine blade). Predictions displayed are for estimated values of the dimensionless property parameter  $(\alpha_D)^{1/2}$  for the  $0.86 \mu\text{m}$  diameter particle used. Maximum value (0.65) corresponds to the Waldmann free-molecule limit using  $\alpha_{\text{wall}} = 1$  (after Komandopoulos and Roener, 1986).

sis and inertia "cooperate" to increase cooled wall mass transfer rates (Komandopoulos and Roener, 1986). Figure 2 shows our results for the dimensionless particle mass-transfer rate parameter  $Sc/Re_0$  as a function of both  $T_e/T_p$  and the relevant particle inertia parameter  $Sc/Re_0$  for forced flow past a "cold" concave surface (simulating (apart from turbulence) the pressure side of a combustion turbine blade). Predictions displayed are for estimated values of the dimensionless property parameter  $(\alpha_D)^{1/2}$  for the  $0.86 \mu\text{m}$  diameter particles used, with the maximum value corresponding to the Waldmann free-molecule limit:  $(3/4)N + (\pi/8)\alpha_{\text{wall}}^{-1}$ , evaluated using  $\alpha_{\text{wall}} = 1$ . For larger suspended particles than those used ( $0.86 \mu\text{m}$ ) in these experiments, carried out at  $T_e$  values near 1500 K, the thermophoretically dominated  $Sc/Re_0^{1/2}$  values would be smaller (due to the reduction in  $(\alpha_D)^{1/2}$  for a given  $T_e$ )

$$(\alpha_D)^{1/2} \approx C_1 [1 + (1/2)(k_p/k_p')^{1/2}]^{-1} (Sc_p) \quad (4-8)$$

where  $D_p$  is the corresponding particle Brownian diffusion coefficient ( $4\pi/3$ ), and  $C_1$  ( $\alpha_{\text{wall}}$ ) is the interaction force law defined above. This means that when  $Sc_p$  increases, so does  $(\alpha_D)^{1/2}$ , with the interesting result that the relevant product  $(\alpha_D)^{1/2}$  appearing in eq 4-8 remains a size-independent constant. Accordingly, despite the smallness of  $D_p$  for particles above about 100 nm in diameter, the product  $(\alpha_D)^{1/2}$  remains proportional to  $\alpha_{\text{wall}}^2$  with the factor  $C_1[1 + (1/2)(k_p/k_p')^{1/2}]$ , which will inevitably be smaller for highly conducting particles (silver, diamond,...) than thermal "insulators". Machowski (1990) has applied this method to predict the photophoretic motion of two touching spheres, including unsymmetrical combinations at arbitrary orientations with respect to  $-(\text{grad } T_e)$ , as well as quasi-spherical particle clusters simulating soot aggregates (Roener et al., 1991). From these and related studies it appears that the orientation-averaged  $(\alpha_D)^{1/2}$  written (eq 4-8), is remarkably insensitive to aggregate size and morphology—a result also obtained for swarms of colloidal particles in electrokinetic applications (Acrivos et al., 1990). Moreover, this result provides the theoretical basis for the widely used method of "thermophoretic (soot) sampling" (Dobbs and Megaridis, 1987; Kaphan et al., 1995; Xing et al., 1996a,b). Such sampling is "gentle" enough, relatively unbaised with respect to aggregate size, morphology, and orientation, and associated with adequate capture efficiencies.

In summary, we see that, in all of these cases, the thermal creep velocity associated with tangential temperature gradients is "responsible" for the efficient collection of soot particles (by colder solid targets)

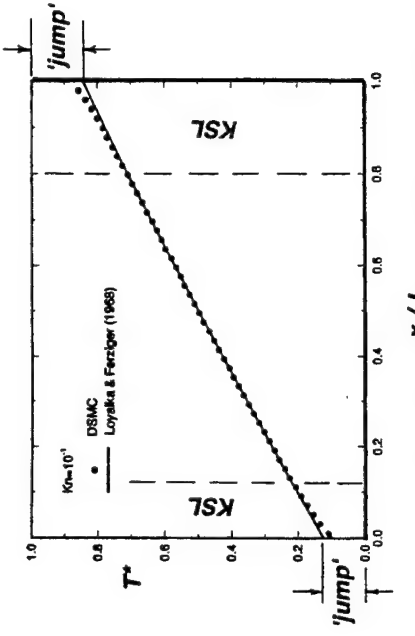


**Figure 3.** Dimensionless temperature vs distance plot for a rarefied gas contained within a one-dimensional gap. The cold wall at  $x/L = 0$  is kept at the relative dimensionless temperature zero and the hot wall at  $x/L = 1$  at unit temperature. The nominal Knudsen number is  $10^{-1}$ . Solid circles represent computational results, whereas the line gives the prediction based on linearized Boltzmann equation theory proposed by Loyalka and Ferriger (1988). The broken lines give an estimate of the local mean-free path (after Papadopoulos, 1996).

sample conditions was comparable to the characteristic diffusional velocity of the pseudo-binary mixture. His estimates showed that even for "Earth-bound" experiments ( $g = 9.8 \text{ m/s}^2$ ) thermal creep-induced flow can cause a nonnegligible effect when compared to buoyancy-induced convection. The fact that the presence of the nonisothermal side walls induces a flow from cold-to-hot implies that, by virtue of total mass conservation, a flow of comparable magnitude will be induced in the opposite direction in the enclosure core region. Consequently, with the help of the end walls, the fluid is forced into a circulatory motion with two counterrotating vortices.

These qualitative and semiquantitative predictions were corroborated in a recent paper by Papadopoulos and Roener, 1996. The authors used a direct simulation Monte Carlo technique (see section 3.3) to compute the gas flow due to side-wall thermal creep in a Cartesian, two-dimensional geometry charged with a monatomic, inertial gas. A temperature gradient predominantly in the direction parallel to the enclosure side walls was imposed on the microscopic level by assigning the velocities of molecules after collision with the solid wall from a local nondrifting Maxwellian, the temperature of which varied linearly between the values assigned at the end walls. The particular implementation followed an algorithm proposed by Steefenov and Corvig-nan (1993) for a hard-sphere gas but is readily modified to account for other, more realistic, molecular interaction potentials (see Bird, 1984). One of the most appealing features of this approach is that its validity is not limited to any specific range of Knudsen numbers, since it is based on the Boltzmann equation. We emphasize that in these simulations thermal creep and temperature jump are directly determined by the simulation, in contrast with their "prescription" in macroscopic formulae.

In Figure 4 we show a vector velocity field for the specific choice of parameters indicated in the figure caption. Indeed, our DSMC simulation successfully captures the vortical structures referred to above. Since

particles is much smaller than the host gas momentum diffusivity. This causes *isothermal* aerosol convective-diffusion problems to be excellent examples of high-Schmidt number mass transfer (see, e.g., Friedlander, 1977; Pernarola de la Mora and Roener, 1991, 1982) with the Brownian diffusion boundary layer embedded well within the momentum (or vorticity) boundary layer. As a consequence, convective-diffusion particle capture efficiencies, or mass-transfer Stanton numbers (Roener, 1986), are quite small, often below  $10^{-3}$  for particles in the super-100-nm diameter range. However, it is now known that simultaneous heat transfer (e.g., particle collection by a solid target, colder than the "dusty" mainstream) dramatically alters this situation because of the efficient collection mechanism of *particle thermophoresis*. For example, one industrially significant application is the collection of doped glass microdroplets in the fabrication of optical waveguide fibers (Walker et al., 1979; Roener and Park, 1989). If one formally writes the local thermophoretic particle drift velocity in the form:

$$\mathbf{V}_p = (\alpha_D D_p) \mathbf{k} - (\text{grad } T_e) \mathbf{T}/T_p \quad (4-8)$$

where  $D_p$  is the corresponding particle Brownian diffusion coefficient ( $4\pi/3$ ), and  $\mathbf{T}$  and  $T_p$  are the dimensionless temperature and particle temperature, respectively, then our attention is properly focused on the dimensionless thermophoretic diffusion factor ( $\alpha_D$ ). Because of the thermal creep velocity induced at the surface of the nonisothermal solid sphere, it is "propelled" through the gas, moving from hot to cold. With this picture Epstein (1929) estimated that in the near-continuum limit:<sup>10</sup>

$$(\alpha_D)^{1/2} \approx C_1 [1 + (1/2)(k_p/k_p')^{1/2}]^{-1} (Sc_p) \quad (4-9)$$

where  $D_p$  is the corresponding particle Brownian diffusion coefficient ( $4\pi/3$ ), and  $\mathbf{T}$  and  $T_p$  are the dimensionless temperature and particle temperature, respectively, that when  $Sc_p$  increases, so does  $(\alpha_D)^{1/2}$ , with the interesting result that the relevant product  $(\alpha_D)^{1/2}$  appearing in eq 4-8 remains a size-independent constant. Accordingly, despite the smallness of  $D_p$  for particles above about 100 nm in diameter, the product  $(\alpha_D)^{1/2}$  remains proportional to  $\alpha_{\text{wall}}^2$  with the factor  $C_1[1 + (1/2)(k_p/k_p')^{1/2}]$ , which will inevitably be smaller for highly conducting particles (silver, diamond,...) than thermal "insulators". Machowski (1990) has applied this method to predict the photophoretic motion of two touching spheres, including unsymmetrical combinations at arbitrary orientations with respect to  $-(\text{grad } T_e)$ , as well as quasi-spherical particle clusters simulating soot aggregates (Roener et al., 1991). From these and related studies it appears that the orientation-averaged  $(\alpha_D)^{1/2}$  written (eq 4-8), is remarkably insensitive to aggregate size and morphology—a result also obtained for swarms of colloidal particles in electrokinetic applications (Acrivos et al., 1990). Moreover, this result provides the theoretical basis for the widely used method of "thermophoretic (soot) sampling" (Dobbs and Megaridis, 1987; Kaphan et al., 1995; Xing et al., 1996a,b). Such sampling is "gentle" enough, relatively unbaised with respect to aggregate size, morphology, and orientation, and associated with adequate capture efficiencies.

In summary, we see that, in all of these cases, the thermal creep velocity associated with tangential temperature gradients is "responsible" for the efficient collection of soot particles (by colder solid targets)

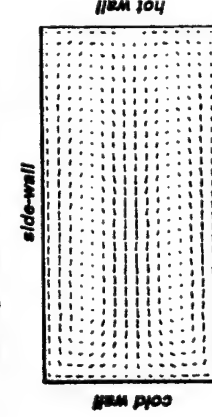


**Figure 4.** Flow field caused by thermal convection in an example of an aspect ratio of 2. Relevant parameters are  $T_{\text{bottom}} = (6K)(\lambda/77)$ ,  $4.5 \times 10^{-5}$ ,  $T_b = 800$  K, and  $\lambda/77 = 0.06$ . Symmetry of the geometry and imposed boundary conditions allow for a reduction of computational cost by a factor of 2. Two vertical rows are established, which are mirror images of each other (after Papadopoulos and Rosner, 1996).

The calculation is for a two-dimensional enclosure, the vertices are essentially rolls that extend in the third direction, with the vorticity vector changing direction across the symmetry plane  $Y = Y_s$  ( $s = 1, 2$ ). It is quite remarkable that without assigning a slip velocity explicitly or implicitly at the boundary and in the complete absence of body forces, convective motion arises merely as a consequence of interactions between molecules and the nonisothermal solid boundaries and between molecules and other molecules, confirming the expectations of Rosner (1988).<sup>4</sup> Put another way, despite the small Knudsen numbers typically associated with these flows ( $0(10)^{-5}$ ), one cannot apply no-slip boundary conditions along the nonisothermal amplitude walls—i.e., the walls drive a significant amount of convection. Incidentally, the approachable statistical scatter appearing in Figure 4 is directly related to the very low Mach number characterizing creeping flow problems. As a result, adequate resolution of small velocity scales requires an increased amount of statistics, which inevitably leads to longer computational execution times. For these reasons, one of the ultimate objectives in performing microscopic simulations is to guide the development of efficient, and accurate, continuum computational schemes (e.g., Machowski et al., 1998; Vrijant and Savino, 1983) based on the more detailed information now becoming available, rather than using DSMC as a routine predictive tool. However, for some applications in which the relevant local Knudsen number is  $O(1)$ , as in embatmospheric pressure CVD/etching reactors, DSMC-type simulations may be "inappropriate" (see e.g., Coronall and Jones, 1993; Barbill, 1995).

## 5. Generalizations and Conclusions

We have emphasized here perhaps the simplest (and least understood) fluid/solid interface, or, the ideal gas/solid crystalline solid interface. Not only is this

engineering importance, as the examples of section 4 demonstrate. Moreover, reasonably direct measurements of the relevant accommodation coefficients can be made using molecular beam/surface science techniques (see e.g., Fenn et al., 1987). However, before turning to dense vapor and true liquid/solid interfaces, it would be misleading to imply that important questions do not remain concerning momentum, energy, and mass exchange at nonequilibrium gas/solid interfaces. In this connection, mention should be made of the ubiquitous complexities of dealing with polyatomic gas mixtures, surfaces which are either partially covered by adsorbed molecules from the vapor phase or rough on many scales (up to and including  $\mu$ ), and very high driving forces (values of the product  $K(\lambda/77)$  which do not satisfy the inequality  $K(\lambda/77) < 1$ ).

For reasons similar to those underlying large "dense vapor" corrections to the ideal gas Newtonian viscosity, Fourier thermal conductivity, and Fick diffusivity, we anticipate large but systematic departures from the above-mentioned slip, jump, and creep results (section 3) as one considers nonequilibrium dense vapor/solid and, ultimately, liquid/solid interfaces. While no rational theoretical formalism (akin to the (binary-collision) Boltzmann equation) is available, theoretical progress in this area will probably come principally via the route of relevant molecular dynamics "computer experiments" focused on the fluid/solid interfacial region (see, e.g., Koplik et al., 1989; Mo and Rosner, 1990). Very likely, the most demanding calculations will pertain to the most subtle effects, so that from an engineering viewpoint, when  $I_c \sim I_s \sim 10$ , and  $\sigma$  become comparable, slip, jump, and creep effects will be small enough that their neglect will (usually) be an acceptable approximation (cf. our examples in section 4).

Regarding physical experiments, as pointed out in our review of thermally-induced particle phoresis (section 4.3), these "thermal creep" boundary condition phenomena determine the readily observed migration rates of suspended small solid particles. This leads to the idea that careful phoresis measurements in a suitably designed microgravity environment (to preclude complications, such as "sedimentation" for particles large enough to sustain large temperature differences and to avoid appreciable Brownian motion) could be used to obtain unambiguous information about the nature of the tangential momentum transfer boundary condition over a broad range of Newtonian fluid densities. This would be especially interesting since present theoretical methods are really valid only in the low-density (ideal) gas limit. To clarify the nature of the BC transition from the Rostrating-Chapman regime to the technologically important but theoretically less tractable case of liquid-like densities (including superparamagnetic polytropic vapors), it is inevitable that high-quality experimental data for carefully selected fluid/solid interfaces will be required. The best environment for obtaining these data, since one can escape buoyancy and sedimentation phenomena, may indeed be the microgravity environment. Of course, there are many other types of sharp transitions that can be fruitfully considered to be "interfaces" separating adjacent continua, other than the fluid/solid (phase) boundaries examined here (Rosner, 1976, 1986; Bremner and Leal, 1982). Extrapolating from the specific but instructive examples we have selected here, it can be said that if the transport properties of any kind of "interfacial region" were known, analogous jump expressions could be derived, as well as the necessary conditions for the neglect of such jumps. Thus, the general situation is seen to be

similar to heat conduction across a composite material. If there is an (unseen) thermal resistance between two adjacent conductors, it will appear that the temperature is discontinuous in going from one conductor to the next. Moreover, the magnitude of this "jump" will increase with the magnitude of the energy flux through the interface. Similarly, when there is species mass transfer across any interface (as in the selective dissolution of gases into metals (e.g., Rosner et al., 1976) or the sublimation of a multicomponent solid), there must be an associated jump in chemical potential, etc. Indeed, gaining a quantitative understanding of the nature of interfacial resistances to transport is an important goal of the science of interfacial chemistry. Fortunately, in many cases of engineering importance, it can be assumed that the "interfacial resistances" are negligible, especially compared to other resistances in series with the interface. Then, and only then, phase equilibrium relationships can be invoked as a locally valid approximation, even in the presence of a net transfer rate. However, as emphasized by our present selection of gas/solid examples (section 4), it is more prudent for the engineer/scientist to view continuity of the relevant field variables across an interface (e.g., tangential velocity, temperature, chemical potential), etc., as a potentially useful approximation rather than a rule comparable in stature to a conservation principle. This viewpoint was expressed well by Standard (1968), perhaps appropriately for concluding this paper: "Only *actual continuity* of a variable when we can prove it to exist".

## Acknowledgment:

It is a honor and a pleasure to be included in this birthday celebration of Eli Ruckenstein's extensive contributions to the fields of physical chemistry and chemical engineering science and to acknowledge Prof. Ruckenstein's occasional but timely guidance (to D.E.R.) over a c. 30 year period. Eli's career-long fascination with (a) interfacial phenomena, (b) simulation methods which establish quantitative relationships between complex convective-diffusion situations and their simple (limiting-case) counterparts, (c) the exploitation of rational asymptotic approximations (especially  $S_c \gg 1$ ), and (d) non-Brownian mechanisms of suspended particulate transport either have proven to be extremely contagious or are remarkably shared by at least one of us (D.E.R.). This particular contribution places our recent research at the Yale University Chemical Engineering Department High Temperature Chemical Reaction Engineering Laboratory (especially in the areas of particulate thermophoresis across combustion gas boundary layers and wall creep-driven flows in microgravity, crystal growth) into the broader historical and pedagogical context of jump, slip, and creep effects at fluid/solid interfaces, including not only ideal gas mixtures but also deca-superionic electrolyte solutions. We are indebted to our sponsors: AFOSR (Grant No. 94-1-0143), NASA, MSAD (Grant No. NAG 3-1654), and the HTCRE Lab, Industrial Affiliates: ALCOA, DuPont, Union Carbide, Praxair, Shell, SCM-Chemicals, General Electric, Babcock and Wilcox, and its publication, possible but also due to its publication, possible. D.E.R. would also like to acknowledge the contributions of all of his co-authors (section 6), Yale faculty colleagues (J. B. Fenn, A. Gomez, and J. Fernandez de la Mora), and former students in helping to shape many of the ideas summarized here. In some sense, this paper can be considered an intellectual "sequel" to his paper *Chem. Eng. Educ.* (ASEE, CHE Div.) 1976, X (4), 190-194 on

boundary/jump conditions and sections 2.6.1 and 4.3 of his book *Transport Processes in Chemical Reacting Flow Systems* (Rosner, 1986). Finally, especially in view of the untimely death of Brown University Prof. A. Marion (Fall 1995), we acknowledge the enormous contributions he made to this general subject, based on his deep understanding of the kinetic theory of gases.

## Nomenclature

$A_i (i=1,2,3)$	= coefficients in $C_{\text{dp}}$ expression, eq 4-4
$c$	= mean molecular thermal speed
$C_p$	= molar heat capacity
$C_f$	= skin friction coefficient (dimensionless); e.g., Rosner, 1986
$C_0$	= drag coefficient (dimensionless)
$C_1$	= thermal creep coefficient
$C_2$	= slip correction factor, eq 4-1
$C_{\text{dp}}$	= concentration creep coefficient, eq 3-2
$C_{\text{so}}$	= fullalene (carbon)
$D_1$	= binary diffusion coefficient
$D_2$	= particle diameter
$G$	= net mass flux through interface
$h$	= specific enthalpy
$h_a$	= stagnation enthalpy; e.g., Rosner, 1996
$j^*$	= species mass diffusion flux vector
$k_B$	= Boltzmann constant
$k_g$	= gas thermal conductivity
$k_p$	= particle thermal conductivity
$M$	= molecular weight
$m$	= species i mole fraction
$M_0$	= Mach number
$Nu$	= Nusselt number; e.g., Rosner, 1986
$n$	= number density
$P_r$	= Prandtl number (momentum/density diffusivity ratio)
$p$	= pressure
$q''$	= energy diffusion flux vector
$R$	= universal gas constant
$S_c$	= Schmidt number; $\sqrt{D_A}/D_g$
$S_t$	= Stanton number; e.g., Rosner, 1986
$S_t$	= particle Stokes number, $(\rho L)/(\mu D)$
$T$	= absolute temperature
$U^*$	= dimensionless temperature, Figure 3
$t^*$	= dimensionless time; eq 4-5
$U'$	= mainstream gas velocity
$v$	= gas velocity
$x$	= distance measured along the wall
$y$	= distance measured normal to the wall
$Y$	= species i mole fraction
$Z$	= dimensionless distance in the vertical direction
$Z^*$	= molecular flux

## Greek Symbols

$\alpha$  = accommodation coefficient

$\delta$  = thermal diffusion factor

$\delta^*$  = boundary layer thickness; Figure 1

$\mu$  = dynamic viscosity

$\nu$  = momentum diffusivity,  $\mu/\rho$

$\rho$  = mass density of mixture

$\sigma$  = molecular diameter

$\tau$  = local shear stress

$\omega$  = species mass fraction

**Subscripts and Superscripts**

$\circ$  = pertaining to the outer edge of the viscous boundary layer; Figure 1

E, G = pertaining to the gas

- Brush, S. G.; Everett, C. W.; Maxwell, Osborne; Reynolds and the Radiometer. *Historical Studies in the Physical Sciences*; University Pennsylvania Press: Philadelphia, PA, 1968; Vol. 1, pp 105–125.**
- Caldwell, K. D. *Field-Flow Fractionation*. *Anal. Chem.* 1988, 60 (17), 989A–971A.
- Castillo, J. L.; Makkowski, D. W.; Rausser, D. E. *Photophoretic Contribution to the Transport of Absorbing Particles Across Combustion Gas Boundary Layers*. *Prog. Energy Combust. Sci.* 1990, 16, 253–260.
- Castillo, J. L.; Garcia-Ybarra, P. G.; Rausser, D. E. *Morphological Instability of a Thermophoretically Growing Deposit*. *J. Cryst. Growth* 1991, 116, 105–126.
- Connell, D. G.; Jensen, K. F. *Modeling of Rarefied CVD Processes at Reduced Pressure and Reduced Dimensions*. *Proc. CVI/II*, Electrochem. Soc. 1993, 93 (2), 57–63. Cf., also: *J. Electrochem. Soc.* 139 (8), 2264–2273.
- Davis, E. J. *Micro-Chemical Engineering: The Physics and Chemistry of the Micro-Particle*. Advances in Chemical Engineering, Academic Press: New York, 1992; Vol. 18, pp 1–94.
- Davis, R. W.; Morris, E. F.; Zechirich, M. R. *J. Cryst. Growth* 1988, 92, 513. See also: Davis, R. W.; Burns, T. J. *Numerical Modeling of Particle Transport in Rotating Disk and Barrel Type CVD Reactors*. AICHE 1986 Meeting, Paper 158e.
- Dobrina, R. A.; Negendank, D. *Morphology Flame-Generated Soot as Determined by Thermophoretic Sampling*. *Langmuir* 1987, 3, 254–259.
- Edwards, D.; Denby, V.; Mills, A. *Thermophoresis—An Introduction to Diffusion, Convection and Radiation*, 2nd ed.; Holt, Reinhardt & Winston: New York, 1978.
- Edwards, D. A.; Brenner, H.; Waas, D. T. *Transport Processes and Rheology*; Butterworth-Heinemann: Stoneham, MA, 1991.
- Espinosa, P. S. *Zur Theorie des Radiometers*. *Z. Phys.* 1929, 54, 637–653.
- Fernandes de la Mora, J. B.; Rausser, R. N. *Measurements of Momentum Accommodation of Gas Molecules at Surfaces*. In *Fundamentals of Gas-Surface Interactions*; Salzburg, H., et al.; Academic Press: New York, 1967.
- Fernandes de la Mora, J.; Rausser, D. E. *Inertial Deposition of Particles Revisited and Extended: A Eulerian Approach to a Traditionally-Lagrangian Problem*. *J. PhysicoChem. Hydrodyn.* 1981, 2, 1–21.
- Fernandes de la Mora, J.; Rausser, D. E. *Effects of Inertia on the Differential Deposition of Small Particles to Spheres and Cylinders at Low Reynolds Numbers*. *J. Fluid Mech.* 1982, 125, 379–395.
- Friedlander, S. K. *Smoke, Dust and Haze—Fundamentals of Aerosol Behavior*; Wiley: New York, 1977.
- Fuchs, N. A. *The Mechanics of Aerosols*; Pergamon: Oxford, UK, 1964.
- Fuchs, N. A.; Subrahmanyam, A. *Highly Turbulent Flow of Particles in Suspensions*. *Trans. Faraday Soc.* 1960, 56, 947–952.
- Alexander, F. J.; Garcia, A. L.; Alder, B. J. *A Consistent Boltzmann Algorithm*. *Phys. Rev. Lett.* 1986, 56, 6212–6215.
- Alexander, J. *Colloid Transport by Interfacial Forces*. *Annu. Rev. Fluid Mech.* 1989, 21, 61.
- Ansari, B. K.; Mason, R. A. *Theory of Thermophoresis of Spherical Aerosol Particles*. *Aerosol Sci.* 1975, 6, 105–117. See also: Ansari, B. K. *J. Chem. Phys.* 1972, 57 (7), 562.
- Bailey, T. J. *Low Density Gas Modelling in the Micro-electronics Industry*. In *Rarefied Gas Dynamics*. Proceedings of the 19th International Symposium, Oxford, July 1984; Harvey, J.; Lord, G., Eds.; Oxford University Press: Oxford, U.K., 1986; pp 611–620.
- Bergenov, S.; Chernyav, V. *Thermophoresis of Spherical Particle in a Rarefied Gas: Numerical Analysis Based on the Model Kinetic Equations*. *Phys. Fluids* 1986, 44, 107–119.
- Bird, G. A. *Direct Simulation of the Incompressible Navier-Stokes Problem*. *Prog. Astronaut. Aerona.* 1976, 51, 323–333.
- Bird, G. A.; Rausser, D. E. *Prediction and Rotational Correlation of Thermophoretically Reduced Particle Mass Transfer to Hot Surfaces Across Laminar or Turbulent Forced-Convection Gas Boundary Layers*. *Chem. Eng. Commun.* 1986, 44, 107–119.
- Cooper, A.; Rausser, D. E. *Thermophoretic Effects on Particles in Counterflow Laminar Diffusion Flames*. *Combust. Sci. Technol.* 1983, 39, 385–392.
- Goldschmidt, S. A.; Wachman, H. Y. *Dynamics of Gas-Surface Scattering*. Academic Press: New York, 1976.
- Halperin, B.; Rausser, D. E. *Chemical Energy Accommodation at Catalyst Surfaces: Flow Reactor Studies of the Association of Nitrogen Atoms on Metals at High Temperatures*. *J. Chem. Soc., Faraday Trans. 1* 1978, 74, 1883–1912.
- Kamotani, Y.; Ostreich, S.; Pine, A. *A Thermocapillary Convection Experiment in Microgravity*. *J. Heat Transfer* 1986, 108, 611–618.
- Kennard, E. H. *Kinetic Theory of Gases*; McGraw-Hill: New York, 1938.
- Kiehl, J.; Halperin, B. H.; Rausser, D. E. *Chemical and Physical Energy Accommodation in the Metal Surface-Catalyzed Decomposition of Hydrazine Vapor*. *J. Phys. Chem.* 1984, 88, 4622–4627.
- Kincaid, J. M.; Li, Y.; Heifield, B. *Nonequilibrium Molecular Dynamics Calculations of the Thermal Diffusion Factor*. *Fluid Phase Equilibr.* 1992, 76, 113–121.
- Koren, M. N. *Molecular Gas Dynamics*. *Annu. Rev. Fluid Mech.* 1978, 6, 383–404.
- Koren, M. N. *Non-Normal-Stokes Gas Dynamics and Thermal Stress Phenomena*. Proceedings of the 16th International Symposium Rarefied Gas Dynamics; Tuessner, Stuttgart, Germany, 1986; Vol. 1, pp 15–24.
- Konstantopoulos, A. G.; Rausser, D. E. *Inertial Effects on Thermophoretic Transport of Small Particles to Walls with Steady-State Curvature*. *Int. J. Heat Mass Transfer* 1985, 28 (12), 2305–2315 (Part I); 2317–2327 (Part II).
- Koplik, J.; Banavar, J.; Williamson, J. F. *Molecular Dynamics of Fluid Flow at Solid Surfaces*. *Phys. Fluids* 1989, 1, 781–794.
- Kovil, U. O.; Xiang, Y.; Rausser, D. E. *Diffusion Effects on Interfacial Mass Transport Rates*. *PhysicoChem. Hydrodyn.* 1980, 1, 169–186.
- Rausser, D. E. *Mass Transfer Across Combustion Gas Thermal Boundary Layer*. *Energy Mass and Momentum Transport: The Treatment of Jump Conditions at Phase Boundaries and Fluid-dynamic Discontinuities*. *Chem. Eng. Educ.* 1976, 7 (4), 190–194.
- Rausser, D. E. *Thermal (Soret) Diffusion Effects on Interfacial Mass Transport Rates*. *PhysicoChem. Hydrodyn.* 1980, 1, 169–186.
- Rausser, D. E. *Mass Transfer Across Combustion Gas Thermal Boundary Layer: Power Production and Materials Processing Implications*. *Advances in Fire and Combustion Systems*; HTFD 46; ASME: New York, pp 5–8. See also: Proc. Symp. High Temp. Lamp Chem. Electrochem. Soc. 1986, 86–4, 111–138.
- Rausser, D. E. *Side-Wall Gas “Creep” and Thermal Stress Convective Transport Experiments in Microgravity*. *Experiments on Film Growth by Vapor Transport*. *Phys. Fluids A* 1989, 1 (1), 1761–1763.
- Rausser, D. E. *Transport Processes in Chemically Reacting Flow Systems*, 2nd ed.; Butterworth-Heinemann: Stoneham, MA, 1996; 3rd printing 1990; 2nd edition; in preparation.
- Rausser, D. E.; Chung, H. M.; Feng, H. *Resistance Relaxation Studies of Gas/Metal Reactions Leading to Simultaneous Dissolution and Gasification*. *J. Chem. Soc., Faraday Trans. 1* 1976, 72, 842–857; 858–876.
- Rausser, D. E.; Mackowski, D. W.; Garcia-Ybarra, P. S.; Sato, A. *Structure Insensitivity of the Thermophoretic Transport of Aggregated “Soft” Particles in Gases*. *Combust. Sci. Technol.* 1991, 80 (1–3), 89–101.
- Rausser, D. E.; Mackowski, D. W.; Tsatsoulis, M.; Castellano, J. L.; Garcia-Ybarra, P. *Effect of Heat Transfer on the Dynamics and Transport of Small Particles in Gases*. *Ind. Eng. Chem. Res.* 1992, 31, 760–769.
- Rausser, D. E.; Park, H. *Thermophoretically Augmented Mass, Momentum and Energy Transfer Rates in High Particulate Mass Loaded Laminar Forced Convection Systems*. *Chem. Eng. Sci.* 1988, 43 (10), 2659–2704.
- Ruckenstein, E. *Can Planar Motions be Treated as Interfacial Tension Gradient Driven Phenomena?* *J. Colloid Interface Sci.* 1981, 83 (1), 77–81.
- Saxena, S. C.; Joshi, R. K. *Thermal Accommodation and Adsorption Coefficients of Gases*; Hemisphere: Washington, DC, 1989.
- Schaaf, S. A.; Chambre, P. L. *Flow of Rarefied Gases*. Section H of *Acoust. Velocity and Absorption in Cylindrical Tubes*. J. Acoust. Soc. America 1988, 73 (4), 724–729.
- Shindur, P. M.; Liu, G.; Gladstone, J. C. *Separation of Particles in Non-Aqueous Suspensions by Thermal Field-Flow Fractionation and Silver*. *J. Chem. Phys.* 1983, 78 (6), Part I, 3329–3333.
- Shields, F. D.; Lee, S. A.; Wiley, W. J. *Numerical Solution for Sound Velocity and Absorption in Cylindrical Tubes*. J. Acoust. Soc. America 1988, 73 (4), 724–729.
- Shields, F. D.; Liu, G.; Gladstone, J. C. *Separation of Particles in Non-Aqueous Suspensions by Thermal Field-Flow Fractionation*. *Anal. Chem.* 1995, 67 (15), 2705–2713.
- Somorjai, G. A. *Chemistry in Two Dimensions*; Cornell University Press: Ithaca, NY, 1981.
- Somorjai, G. A.; Lester, G. J. *Evaporation Mechanisms of Solids*. In *Progress in Solid State Chemistry*; Reihs, H., Ed.; Pergamon Press: Oxford, U.K., 1987; Chapter 1, Vol. 4, pp 1–52.
- Stander, G. *The Thermodynamic Significance of Danchenko's Boundary Conditions*. *Chem. Eng. Sci.* 1968, 23, 645–655.
- Stefanov, S.; Cercignani, C. *Monte-Carlo Simulation of the Taylor-Couette Flow of a Rarefied Gas*. *J. Fluid Mech.* 1985, 156, 189–199.
- Talbot, L. *Thermophoresis—A Review*. *Rarefied Gas Dynamics Prog. Astronaut. Astron. (AAIA) Part 1* 1981, 74, 487–488.
- Tandow, P.; Rausser, D. E. *Translational Brewnian Diffusion Coefficient of Large Multiparticle Suspended Aggregates*. *Ind. Eng. Chem.* 1985, 77, 3265–3277.

Tsien, H.-B. Supercadynamics; Mechanics of Rarefied Gases. *J. Aerosp. Sci.* 1948, 15, 653-664.  
 Vittimberga, A.; Savino, R. Recent Developments in Vapor Crystal Growth Fluid Dynamics. *J. Cryst. Growth* 1993, 132, 217-229.  
 See, also: Napolitano, L. G.; Vittimberga, A.; Savino, R. *Acta Astronaut.* 1992, 30, 187.  
 Widawski, D. Slip Effects in a Confined Rarefied Gas. I. Temperature Slip. *Phys. Fluids A* 1988, 5, 183-189.  
 Williams, K. L.; Honey, J. M.; Geysing, F. T. Thermodynamic Deposition of Small Particles in Laminar Tube Flow. *J. Colloid Interface Sci.* 1979, 71, 138-147.  
 Williams, M. M. R.; Loyalka, S. K. *Aerosol Science: Theory and Practice With Special Applications to the Nuclear Industry*; Pergamon: Oxford, U.K., 1991.  
 Xing, Y.; Koyanagi, U. O.; Rosner, D. E. Synthesis and Restructuring of Nanocrystalline in Counterflow Diffusion Flames. *Combust. Flame* 1996, in press.  
 Xing, Y.; Koyanagi, U. O.; Tandem, P.; Rosner, D. E. Measuring and Modelling the Synthesis and Morphological Evolution of Particles in Laminar Counterflow Diffusion Flumes. Proceedings of the 5th World Congress on Chemical Engineering, San Diego, CA, July 1996; Paper #88d, Vol. V, pp 43-48.

#### Footnotes

(1) However, mention should be made of low sublimation (or desublimation probability,  $\alpha_m$ ) when even single-component solid evapors (or are condensed). This causes sublimation rate based only on equilibrium vapor pressure data to be overpredicted (and also underpredicted) the sensitivity of the sublimation rate to surface temperature. Low and  $T$ -dependent  $\alpha_m$  values are associated with smooth solid surfaces in systems where the act of "physical" sublimation involves considerable atomic rearrangement (as in the sublimation of arsenic:  $As(Ag) = As(Ag)$ , for which  $\alpha_m = 0.10^{-3}$  (Rosenthal and Lee, 1986). A compilation of such evaporation coefficient data is given in, e.g., Sonogashira and Lester, 1987; Sonogashira, 1991). Of course, some chemical reaction probabilities are high ( $0.10^{-1}-10^0$ ), especially for systems (radical)void reactions forming volatile products (see, e.g., Rosner, 1973).

(2) Buchenau (1961) also established conditions under which such phenomena is analogous to the Marangoni motion of emulsion droplets (see, e.g., Peshkin, 1989; Edwards et al., 1991) in the sense that the corresponding phoretic velocity can be expressed as the product of the fluidity of the host solvent and the change in surface energy over one appropriate interfacial length (Debye length thickness, ...).

(3) When the Knudsen number is not negligible compared to the local radius of curvature of the condensed phase interface, we must account for the differences in area across the KEP. This is the case for the evaporation or growth of small droplets, i.e., at under conditions such that the mass-free-path is nonnegligible compared to the droplet radius (Pucci and Santagati, 1970; Pucci, 1984; Williams and Loyalka, 1991).

(4) Recall that if the KEP-condensed phase interface is itself the site of chemical and/or phase change, then  $\zeta'$  will generally not be continuous across it and there will be a net mass flux  $G$  passing through the interface. In such cases we can usually impose  $G = 0$  and  $G'(0) = -h_0'$ , where  $h_0$  is the "local" specific enthalpy (Rosner, 1986).

(5) When the Knudsen number is not negligible compared to the penetration depth of the gas in the porous medium (see, e.g., Tadros and Rosner, 1986). We do not consider such interfaces further here (see, also, section 6).

(6) For polyatomic gas molecule a reasonable approximation to the Prandtl number  $P_r$  (momentum/heat diffusivity ratio)

is  $[1 + (5/4)N_A - 1]^{1/2} - 1$  (Eucken); which reduces to  $1/6$  for the case of a monatomic gas without electronic excitation ( $\gamma = 5/3$ ). In this important limiting case,  $(\gamma + 1)/2P_r = 8/15 \approx 0.33$  so that  $Q_0$  (eqs 2-12) and  $Q_1$  (eq 2-14) are nearly equal.

(7) Two common examples of important jumps in a continuum ( $f_{in} \ll 1$ ) flow are the following cases: (a) Chemical nonequilibrium may be small enough to be well into the continuum range (say,  $10^{-3}$ ), the chemical reaction probability,  $\zeta_{ch}$  (often written  $\phi$ ), may itself be exceedingly small (Sonogashira, 1981),  $\epsilon \cdot 10^{-6}$ . (b) Poor energy accommodation, say, at a helium/tungsten (Aihara et al., 1987) or helium/platinum interface. In this case  $E_A$  can be as low as  $6 \times 10^{-5}$ . See section 4 for examples. For a compendium of experimental EAC-values, see Savenkov and Joshi (1989).

(8) Of course,  $A_3$  and  $A_1$  must also be  $\alpha_m$ -dependent. For example, when  $K_{eff} = \alpha_m$ ,  $C_{in} = 2/5e^{3/2}A_3 + A_1$ . Comparison of this result with Epstein's (1929) result for the free-molecule drag on a solid sphere gives  $A_3 + A_1 \approx 91 + 0.1/\alpha_m^{1/2}$ . For the mass-transfer analog of  $C_{in}$ , see, e.g., Li and Davis, 1986.

(9) Note that, even if  $K_{eff} \ll 1$ , the diameter dependence of  $\epsilon_p$  and  $D_p$  can depart noticeably from  $d_p^{1/2}$  and  $d_p^{-1/2}$ , respectively,

(10) A result of the importance of  $C_{in}$  ( $K_{eff}$ ,  $\alpha_m$ ,  $\epsilon$ ,  $\gamma$ ,  $\rho$ ,  $T$ ) was subsequently generalized by Brock (1962), Talbot (1961), and Loyalka (1986) to extend the domain of Knudsen number applicability, including the free-molecule limit for nonspherical particles (Garcia-Ybarra and Rosner, 1989).

(11) Experimentally, this effect is not so pronounced (see, e.g., Li and Davis, 1986). A comprehensive theory based on the linearized Boltzmann equation (moment method solution) covering the entire range of  $K_{eff}$  and  $k/k_{in}$  values has been given by Berezhnev and Chernyav (1985).

(12) An interesting and important corollary of the importance of particle thermoplasma to gaseous systems with appreciable temperature gradients ( $\epsilon_A$ ,  $\dot{m}$ ,  $c_{in}$ ) is that, in such systems, particles can be brought to rest ("trapped") at spatial positions systematically different from the position(s) at which the hot gas is brought to rest (Gomes and Rosner, 1983). In particle synthesis flames this "particle stearation point" phenomenon can be exploited to control particle morphology and chemistry (Gomes and Rosner, 1983; Majda, 1980), whereas in CVD reactors such locations may be prone to the growth of larger contaminant aggregates by localised condensation (Davis et al., 1983).

(13) As pointed out by P. J. W. Dohye some time ago, C. Ludwig (1986) appears to have discovered the "Soviet effect" some 23 years before Sorel!

(14) As pointed out by Kogan (1973, 1986) and Rosner (1988), thermal stresses (seesawed with Burnett terms) can drive nontrivial gas flows far from (convective) or piecewise isothermal wall. Continuum calculations of such flows are contained in Macztowski et al. (1996) and Vittimberga et al. (1993).

Received for review January 26, 1996  
 Revised manuscript received July 1, 1996  
 Accepted July 1, 1996  
 IEB9603651

• Abstract published in Advance ACS Abstracts, August 15, 1996.

# REPORT DOCUMENTATION PAGE

Form Approved  
OMB No. 0704-0188

Public reporting burden for this collection of information is estimated to average 1 hour per response, including the time for reviewing instructions, searching existing data sources, gathering and maintaining the data needed, and completing and reviewing the collection of information. Send comments regarding this burden estimate or any other aspect of the collection of information, including suggestions for reducing the burden, to Washington Headquarters Service, Directorate for Information Operations and Reports, 1215 Jefferson Davis Highway, Suite 1202, Arlington, VA 22202-4302, and to the Office of Management and Budget, Paperwork Reduction Project (0704-0188) Washington, DC 20585.

1. AGENCY USE ONLY (Leave blank)	2. REPORT DATE	3. REPORT TYPE AND DATES COVERED	
	1996	Reprint	
4. TITLE AND SUBTITLE			5. FUNDING NUMBERS
Erosion rate prediction and correlation technique for ceramic surfaces exposed to high speed flows of abrasive suspensions			PE - 61102F PR - 2308 SA - BS G - F49620-94-1-0143
6. AUTHOR(S)			
Yehia F. Khalil, Daniel E. Rosner			
7. PERFORMING ORGANIZATION NAME(S) AND ADDRESS(ES)			8. PERFORMING ORGANIZATION REPORT NUMBER
<b>Yale University</b> <i>High Temperature Chemical Reaction Engineering Laboratory</i> Department of Chemical Engineering PO Box 208286 YS, New Haven, CT 06520-8286 USA			
9. SPONSORING/MONITORING AGENCY NAME(S) AND ADDRESS(ES)			10. SPONSORING/MONITORING AGENCY REPORT NUMBER
AFOSR/NA 110 Duncan Avenue, Suite B115 Bolling AFB DC 20332-0001			
11. SUPPLEMENTARY NOTES			
Wear 201 (1996) 64-79			
12a. DISTRIBUTION/AVAILABILITY STATEMENT		12b. DISTRIBUTION CODE	
Approved for public release; distribution is unlimited			
13. ABSTRACT (Maximum 200 words)			
<p>We describe a simple method to predict (based on available erosion yield data) erosion rates for cylindrical ceramic targets (e.g. circular tube coatings, leading edges of turbine blades, or the ceramic-lined target zone inside CFBC-cyclones) exposed to high-speed abrasive particle-laden streams. Use is made of a convenient parameterization/extrapolation of published laboratory results giving, in effect, average erosion yields per particle impact (<math>\epsilon_p</math>) for particular planar ceramic target and projectile materials over a range of impact velocities, <math>V_p</math>, incidence angles, <math>\theta_i</math>, and particle sizes, <math>v_p</math>. For a given target/flow geometry we reduce the engineering problem of predicting absolute target erosion rates to that of multiplying a readily calculated characteristic erosion rate by the universal dimensionless erosion rate functions explicitly approximated here in the limit of impacts by particles large enough to be undeflected or slowed down by the local target gas flow. Our characteristic erosion rate is that which would be associated with the mainstream abrasive particle volume flux if all particles struck at normal incidence with the mainstream velocity, <math>U</math>. Dimensionless erosion rate results are cast in terms of the following four dimensionless parameters characterizing the erodent/ceramic target system of interest: sensitivity (exponent <math>n</math>) of erosion yield to projectile incident velocity; sensitivity (exponent <math>m</math> appearing in <math>(\cos^n(\theta_i))</math>) of erosion yield to angle of incidence <math>\theta_i</math>; sensitivity (exponent <math>l</math>) of erosion yield to projectile particle size (volume, <math>v_p</math>); and the reference erosion yield, <math>\epsilon_{p,ref}</math> (here, <math>\epsilon_p</math> is evaluated at <math>V_p = 100 \text{ m s}^{-1}</math>, <math>\theta_i = 0</math>, and <math>v_p</math> corresponding to <math>d_p = 100 \mu\text{m}</math>). Based on our preliminary survey of available erosion yield experimental data, we provide a table giving "best-fit" values of the four parameters: <math>l</math>, <math>m</math>, <math>n</math>, and <math>\epsilon_{p,ref}</math> required to complete a prediction of local and spatially-averaged erosion rates according to our present formalism. For the latter, useful closed-form approximations are provided for convex or concave cylindrical target geometries in the high Stokes number limit. Moreover, convenient correction factors are developed to account for a (Rosin-Rammler) particle size distribution in the erodent mainstream, and mainstreams not perpendicular to the cylinder axis. The more general case of arbitrary (finite) Stokes numbers is outlined. Using two numerical examples (convex leading edge coating on a turbine stator blade, and concave sector target zone in a CFBC-cyclone), we demonstrate that casting required erosion yield data in this suggested format greatly facilitates erosion design calculations for ceramic targets (or coatings) exposed to high-speed abrasive particle suspensions. Organizing empirical data in this manner will also facilitate the longer range goal of correlating each of the above-mentioned parameters with independently measurable physical properties of the participating materials.</p>			
14. SUBJECT TERMS		15. NUMBER OF PAGES	
erosion yield, impact erosion, ceramic targets, abrasive suspensions, turbine blades, cyclone wall erosion		16	
17. SECURITY CLASSIFICATION OF REPORT		18. SECURITY CLASSIFICATION OF THIS PAGE	
Unclassified		Unclassified	
19. SECURITY CLASSIFICATION OF ABSTRACT		20. LIMITATION OF ABSTRACT	
Unclassified		UL	

pendently measurable physical properties of the participating materials.

Of course, there are many useful applications of erosion by fine particles impinging on ceramic target surfaces [7–17]. For example, sand-blasting techniques are often used to mechanically clean solid surfaces [3]. Additional applications include the erosive cutting and drilling of hard materials [18]. Indeed, we believe that our present approach, with extensions as indicated in Section 4.4, will be able to predict/correlate attainable cutting and drilling rates.

### 1.2. Objectives

The principal objective of this work is to extend our novel reformulation of the metal erosion problem [19,29] and develop a rather simple method for predicting erosion rates for ceramic target surfaces exposed to high-speed abrasive particle-laden streams. Regarding ceramic targets, two geometrical configurations of special industrial interest (Fig. 1) are explicitly considered in this work: (1) cylindrical ceramic-coated targets in external cross-flow and (2) refractory lined target surfaces, such as those installed on the inner walls of CFBC cyclones.

To achieve our present objective, available experimental erosion yield data are re-examined, and cast into a useful format which provides, Table 1 for each target/erosion system four best-fit erosion parameters that can be used to predict ceramic cylinder erosion rates (see Section 4.1). However, as noted in Section 5, organizing available experimental data in this particular way will also facilitate the longer-range goal

We describe a simple method to predict (based on available erosion yield data) erosion rates for cylindrical ceramic targets (e.g. circular tube coatings, leading edges of turbine blades, or the ceramic-lined target zone inside CFBC-cyclones) exposed to high-speed abrasive particle-laden streams. Use is made of a convenient parameterization/extrapolation of published laboratory results giving, in effect, average erosion yields per particle impact,  $\phi_p$  for particular planar ceramic target and projectile materials over a range of impact velocities,  $V_p$ , incidence angles,  $\theta_i$ , and particle sizes,  $d_p$ . For a given target/flow geometry we reduce the engineering problem of predicting absolute target erosion rates to that of multiplying a readily calculated characteristic erosion rate by the universal dimensionless erosion rate functions explicitly approximated here in the limit of impacts by particles large enough to be undisturbed or slowed down by the local target gas flow. Our characteristic erosion rate is that which would be associated with the mainstream abrasive particle volume flux if all particles struck at normal incidence with the mainstream velocity,  $U$ . Dimensionless erosion rate results are cast in terms of the following four dimensionless parameters characterizing the end-of/ceramic target system of interest: sensitivity (exponent  $m$ ) of erosion yield to projectile incident velocity; sensitivity (exponent  $n$ ) of erosion yield to angle of incidence; sensitivity (exponent  $\beta$ ) of erosion yield to particle size; and sensitivity (exponent  $\alpha$ ) of erosion yield to projectile incident particle size (volume,  $V_p$ ). Based on our preliminary survey of available erosion yield experimental data, we provide a table giving "best-fit" values of the four parameters,  $l$ ,  $m$ ,  $n$ , and  $\alpha$  required to complete a prediction of local and spatially-averaged erosion rates according to our present formalism. For the latter, useful closed-form approximations are provided for convex or concave cylindrical target geometries in the high Stokes number limit. Moreover, convenient correction factors are developed to account for a (Rosin-Rammler) particle size distribution in the eroded mainstream, and mainstream not perpendicular to the cylinder axis. The more general case of arbitrary (finite) Stokes numbers is outlined. Using two numerical examples (convex leading edge coating on a turbine stator blade, and concave sector target zone in a CFBC-cyclone), we demonstrate that casting required erosion yield data in this suggested format greatly facilitates erosion design calculations for ceramic targets (or coatings) exposed to high-speed abrasive particle suspensions. Organizing empirical data in this manner will also facilitate the longer range goal of correlating each of the above-mentioned parameters with independently measurable physical properties of the participating materials.

**Keywords:** Erosion test; Ceramic targets; Abrasive suspensions; Inertial impaction; Tube coatings; CFBC-cyclone erosion; Turbine blade erosion

has been proposed as erosion-resistant protective coatings, often applied only locally. To design/optimize refractory-lined parts (such as the ceramic coating on turbine blades, the liner of a circulating fluidized bed combustor (CFBC) hot cyclone [6], or the refractory-lined solids return loop between cyclone and combustor), it is clearly necessary to anticipate the local and total erosion rates in the prevailing environment. The methods introduced and demonstrated here will not only permit this for systems which have been studied in laboratory erosion test-rigs, they will also facilitate the important task of correlating the experimental erosion yield parameters we introduce and tabulate (Table 1) with independent variables.

© Corresponding author.  
0031-6949/96/\$15.00 © 1996 Elsevier Science S.A. All rights reserved  
PII S0031-6949(96)07214-6

of correlating each of the above-mentioned parameters with independently measurable physical properties of the participating materials.

### 1.3. Approach

This paper is structured as follows. In Section 2, our principal underlying assumptions are presented. We include a discussion of the proposed erosion yield law and derive/present quadrature expressions for the above-mentioned dimensionless erosion rate functions of greatest practical interest. For simplicity, our emphasis here is on the "worst-case" situation, i.e. the limit of infinite Stokes number (rectilinear particle trajectories).

In Section 3, we present our methods to estimate erosion yield parameters from available erosion yield data and report these parameters for a set of 38 common ceramic target/erosion systems at near 300 K. In Section 4, we provide data for local, maximum, and average erosion rates and provide two numerical examples for calculating erosion of a ceramic target surface; the first example pertains to turbine blade (stator) leading edges, and the second deals with the refractory lining of a CFBC cyclone. Section 5 provides a summary of our principal findings and recommendations for future work.

**2. Mathematical model and outline of formulation**

**2.1. Basic assumptions:**

The following simplifying assumptions are exploited here to capture the essential phenomena encountered in ceramic material erosion:

1. Erosion yield data obtained on planar ceramic targets in test rigs can be self-consistently invoked locally at the surface of large curved ceramic targets (e.g. cylinders) since the target radius of curvature ( $d_t/2$ ) far exceeds the scale of the eroding particle radii (and target grain sizes) of interest here.
2. Rebounding particles do not appreciably influence incoming particles, nor cause significant downstream erosion upon re-impaction on the same target.
3. On the scale of the target radius of curvature, ( $d_t/2$  for a circular cylinder) the mainstream suspended particles are uniformly distributed in space and are individually negligible in size (cf. (1)).
4. While the particle mass loadings,  $\phi_p$ , in the mainstream may not be very small, the volume fraction,  $\phi_p$ , corresponding to the total particle number density  $N_p$  and mean particle volume  $\bar{V}_p$  (i.e.  $\phi_p = N_p \bar{V}_p$ ) is negligible compared with unity.
5. Target surface recession due to erosion is small on the scale of the initial target radius of curvature.

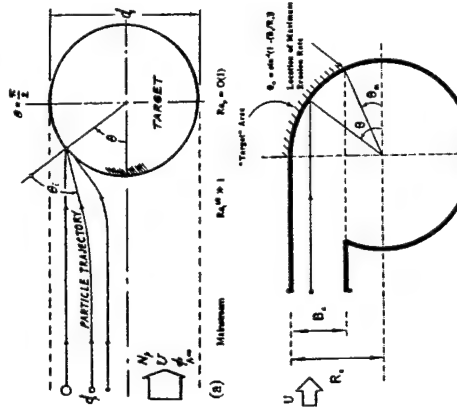


Fig. 1. (a) Circular cylinder in external cross-flow configuration and nomenclature. (b) Impingement (target) sector of cyclone inner walls configuration and nomenclature.

Table 1  
Ceramic targets and abrasive material combinations: Best-fit values of the erosion yield parameters  $\tau_1$ ,  $m$ ,  $n$ , and  $\sigma_{\text{yield}}$

Target material/ erosion system no.	Target material	Erosion type, particle size, and velocity			Erosion parameters			Erosion type, particle size, and velocity			Erosion parameters			Data source						
		Type	$d_p$ ( $\mu\text{m}$ )	$V_p$ ( $\text{m s}^{-1}$ )	$\tau_1$	$m$	$n$	$\sigma_{\text{yield}}$	Type	$d_p$ ( $\mu\text{m}$ )	$V_p$ ( $\text{m s}^{-1}$ )	$\tau_1$	$m$	$n$	$\sigma_{\text{yield}}$					
1	Castable A: 95% High-purity alumina castable Density: 2.70 $\text{g cm}^{-3}$	Dead-burned dolomite	450-680	10.1	1.3	3.0	9.6E-4	Kaiman et al. [1]	14	High strength refractory concrete:	Sand	Density: 2.4 $\text{g cm}^{-3}$	400	11.6	1.2	3.0	1.1E-3	Crowley [22]		
	Castable B: Alumina cement A and calcined fluxes Density: 2.90 $\text{g cm}^{-3}$	Type: 10 $\text{g cm}^{-3}$	450-950	12.2	1.3	3.0	9.6E-4			Alumina cement A and calcined fluxes Density: 2.05 $\text{g cm}^{-3}$										
2	Castable C: Chrome castable, $\text{Cr}_2\text{O}_3/\text{Al}_2\text{O}_3/\text{O}_2$ Density: 2.90 $\text{g cm}^{-3}$	Dead-burned dolomite	680	10.1	1.2	1.1	2.5	7.2E-5	Kaiman et al. [1]	15	Unannealed glass:	Cast iron	Density: 7.8 $\text{g cm}^{-3}$	580	13.0	1.2	2.5	2.3	1.4E-4	Flaake [3]
	Castable F: Light weight castable Density: 1.28 $\text{g cm}^{-3}$	Type: 10 $\text{g cm}^{-3}$	450-950	12.2	1.2	1.1	2.5	7.2E-5		Unannealed glass: Density: 2.47 $\text{g cm}^{-3}$										
3	Glass: Density: 2.47 $\text{g cm}^{-3}$	Dead-burned dolomite	500	14.3	1.2	1.2	2.5	7.2E-5	Kaiman et al. [1]	16	Annealed glass: Density: 2.47 $\text{g cm}^{-3}$	Cast iron	Density: 7.8 $\text{g cm}^{-3}$	580	30.5	1.2	2.7	2.3	1.1E-5	Flaake [3]
	Glass: Density: 2.47 $\text{g cm}^{-3}$	Type: 10 $\text{g cm}^{-3}$	500-950	10.1	1.0	1.0	2.9	7.4E-5		Annealed glass: Density: 2.47 $\text{g cm}^{-3}$										
4	Glass: Density: 2.47 $\text{g cm}^{-3}$	Silica flour: $\text{SiO}_2$ , Density: 2.65 $\text{g cm}^{-3}$	25	14.9	1.2	2.5	2.3	7.2E-1	Head and Harr [20]	18	Annealed glass: Density: 2.47 $\text{g cm}^{-3}$	Cast iron	Density: 7.8 $\text{g cm}^{-3}$	300	9.9	1.2	3.5	2.3	2.5E-4	Bitter [23]
5	Glass: Density: 2.47 $\text{g cm}^{-3}$	Cryotolon: SiC Density: 3.17 $\text{g cm}^{-3}$	39	14.0	1.2	1.8	2.3	2.3E-1	Head and Harr [20]	19	80% Alumina fiber, bonded ceramic: Density: 2.56 $\text{g cm}^{-3}$	Silicon carbide	Density: 3.122 $\text{g cm}^{-3}$	500	60.0	1.2	N/A	2.3	9.8E-5	Liebhard [24]
6	Glass: Density: 2.47 $\text{g cm}^{-3}$	Alumina: $\text{Al}_2\text{O}_3$ , Density: 4.00 $\text{g cm}^{-3}$	39	14.0	1.2	1.8	2.3	2.4E-1	Head and Harr [20]	20	Silicon nitride bonded SiC brick: Density: 2.61 $\text{g cm}^{-3}$	Silicon carbide	Density: 3.22 $\text{g cm}^{-3}$	500	60.0	1.2	N/A	2.3	1.2E-4	Liebhard [24]
7	Glass: Density: 2.47 $\text{g cm}^{-3}$	Glass beads Density: 2.47 $\text{g cm}^{-3}$	38	13.6	1.2	6.3	2.3	5.6E-2	Head and Harr [20]	21	Ultra low content castable: Density: 2.23 $\text{g cm}^{-3}$	Silicon carbide	Density: 3.22 $\text{g cm}^{-3}$	500	60.0	1.2	N/A	2.3	1.8E-4	Liebhard [24]
8	High purity refractory: 95% $\text{Al}_2\text{O}_3$ castable refractory bonded with calcium aluminate cement	Silicon carbide Density: 3.17 $\text{g cm}^{-3}$	150	55	1.2	0.6	2.8	7.5B-7	Wiederhorn and Roberts [21]	22	60% Alumina brick: Density: 2.52 $\text{g cm}^{-3}$	Silicon carbide	Density: 3.22 $\text{g cm}^{-3}$	500	60.0	1.2	N/A	2.3	2.0E-4	Liebhard [24]
9	Insulating refractory concrete: Aluminous cement A and perlite Density: 0.90 $\text{g cm}^{-3}$	Sand Density: 2.4 $\text{g cm}^{-3}$	400	11.6	1.2	0.5	2.3	1.5B-3	Crowley [22]	23	Plat. bonded plastic, fine grain: Density: 2.43 $\text{g cm}^{-3}$	Silicon carbide	Density: 3.22 $\text{g cm}^{-3}$	500	60.0	1.2	N/A	2.3	2.2E-4	Liebhard [24]
10	Insulating refractory concrete: Aluminous cement A and perlite Density: 0.90 $\text{g cm}^{-3}$	Blasting grit Density: 2.65 $\text{g cm}^{-3}$	1760	11.6	1.2	1.4	2.3	1.4B-5	Crowley [22]	24	Plat. bonded plastic, regular grain: Density: 2.44 $\text{g cm}^{-3}$	Silicon carbide	Density: 3.22 $\text{g cm}^{-3}$	500	60.0	1.2	N/A	2.3	2.4E-4	Liebhard [24]
11	Abrasion resistant refractory concrete C: Aluminous cement B and chrome ore aggregate Density: 2.31 $\text{g cm}^{-3}$	Blasting grit Density: 2.65 $\text{g cm}^{-3}$	1760	11.6	1.2	1.6	2.3	1.6B-7	Crowley [22]	25	Low content castable: Density: 2.32 $\text{g cm}^{-3}$	Silicon carbide	Density: 3.22 $\text{g cm}^{-3}$	500	60.0	1.2	N/A	2.3	2.5E-4	Liebhard [24]
12	Abrasion resistant refractory concrete C: Aluminous cement B and chrome ore aggregate Density: 2.31 $\text{g cm}^{-3}$	Sand Density: 2.4 $\text{g cm}^{-3}$	400	11.6	1.2	4.4	2.3	8.9B-6	Crowley [22]	26	60% Alumina brick (maillite based): Density: 2.54 $\text{g cm}^{-3}$	Silicon carbide	Density: 3.22 $\text{g cm}^{-3}$	500	60.0	1.2	N/A	2.3	2.4E-4	Liebhard [24]
13	High strength refractory concrete: Aluminous cement A and calcinated fluxes Density: 2.05 $\text{g cm}^{-3}$	Blasting grit Density: 2.65 $\text{g cm}^{-3}$	1760	11.6	1.2	3.6	2.3	2.0B-6	Crowley [22]	27	Fused silica castable: Density: 2.02 $\text{g cm}^{-3}$	Silicon carbide	Density: 3.22 $\text{g cm}^{-3}$	500	60.0	1.2	N/A	2.3	4.0E-4	Liebhard [24]
									28	Alumina resistant fireclay brick: Density: 2.21 $\text{g cm}^{-3}$	Silicon carbide	Density: 3.22 $\text{g cm}^{-3}$	500	60.0	1.2	N/A	2.3	4.0E-4	Liebhard [24]	
									29	Regular cement castable: Density: 2.07 $\text{g cm}^{-3}$	Silicon carbide	Density: 3.22 $\text{g cm}^{-3}$	500	60.0	1.2	N/A	2.3	4.0E-4	Liebhard [24]	
									30	Super-duty fireclay brick: Density: 2.26 $\text{g cm}^{-3}$	Silicon carbide	Density: 3.22 $\text{g cm}^{-3}$	500	60.0	1.2	N/A	2.3	4.1E-4	Liebhard [24]	
									31	Thermal shock resistant ceramic: Density: 1.81 $\text{g cm}^{-3}$	Silicon carbide	Density: 3.22 $\text{g cm}^{-3}$	500	60.0	1.2	N/A	2.3	4.0E-4	Liebhard [24]	

(continued)

(continued)

Table 1 (continued)

Target material	Target material	Erosion type, particle size, and velocity	Erosion parameters				Data source		
			$d_p$ ( $\mu\text{m}$ )	$V_p$ ( $\text{m s}^{-1}$ )	$I$	$m$	$n$		
32	Abrasion resistance carbide: Density: 2.08 $\text{g cm}^{-3}$	Silicon carbide: Density: 3.22 $\text{g cm}^{-3}$	500	60.0	1.2	N/A	2.3	5.0E-4	Liebhard [24]
33	Pretreated SiC ceramic: Density: 2.98 $\text{g cm}^{-3}$	Silicon carbide: Density: 3.22 $\text{g cm}^{-3}$	274	35–90	1.3	0.8	2.8	8.3E-5	Wang et al. [25]
34	Hot-pressed SiC ceramic: Density: 3.16 $\text{g cm}^{-3}$	Silicon carbide: Density: 3.22 $\text{g cm}^{-3}$	274	35–90	1.3	1.5	2.8	4.0E-5	Wang et al. [25]
35	Hot isostatically pressed ceramic: Density: 3.14 $\text{g cm}^{-3}$	Silicon carbide: Density: 3.22 $\text{g cm}^{-3}$	274	35–90	1.3	0.9	2.8	1.4E-5	Wang et al. [25]
36	Hot-pressed Si <sub>3</sub> N <sub>4</sub> ceramic:	Silicon carbide: Density: 3.22 $\text{g cm}^{-3}$	305	117	1.3	N/A	4.0	4.6E-6	Gulden [26]
37	Reaction-bonded Si <sub>3</sub> N <sub>4</sub> ceramic:	Quartz: Density: 2.65 $\text{g cm}^{-3}$	273	130	1.3	N/A	4.0	3.3E-6	Gulden [26]
38	Hot-pressed Si <sub>3</sub> N <sub>4</sub> ceramic:	Quartz: Density: 2.65 $\text{g cm}^{-3}$	304	285	1.0	N/A	1.0	4.3E-7	Gulden [26]

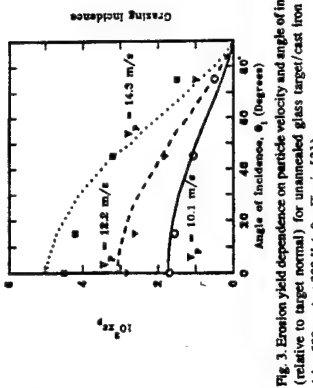
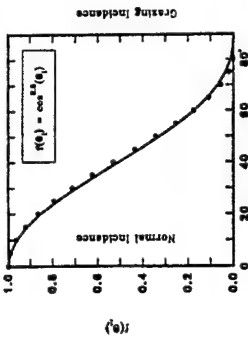
\* All erosion yield data reported here correspond to room temperature. For systems #19 to #32 and #36 to #38, the erosion yield data were provided only at normal incidence ( $\theta = 0^\circ$ ). Therefore, values of the erosion parameter  $m$  (Eq. (2)) cannot be provided here. The values of  $I$  and  $n$  shown here for systems #19 to #32 were provisionally taken from the experimental results for systems #1 to #18.

6. The ceramic target material is either intrinsically isotropic, or if anisotropic (as for pyrolytic  $\text{B}(s)$ ) conformal to the smooth cylindrical substrate. Subject to these assumptions, some of which are critically discussed in Sections 4.3 and 4.4, we show that actual local erosion rates (say, in the units of mm recession per year of continuous exposure) at an orientation  $\theta$  (Fig. 1) can be expressed as the product of an easily calculated characteristic erosion rate ( $ER$ ), and a universal dimensionless function  $E(\theta, \dots)$  calculated and plotted here for two important geometries: the external upwind-facing surface of a circular cylinder in cross-flow (Fig. 1(a)), and the internal (concave) target area (sector) in a cyclone particle separator (Fig. 1(b)). The characteristic erosion rate is thus which would be expected in the prevailing environment if all mainstream particles had the mean size and struck a unit area of targets with undiminished speed and at normal incidence, i.e. in the units of linear recession rate:

$$(ER)_e = s_p (U/\bar{v}_{p,\infty}) \cdot (\bar{v}_p N_p U)_e \quad (1)$$

## 2.2. Erosion yield law: Parameterization

It is not our purpose here to develop further the still incomplete micromechanical theory of erosion yield  $s_p$  when particular projectile materials (erodents) of a particular volume,  $v_p$ , are directed at particular planar ceramic target materials at a known velocity  $V_p$  and angle of incidence  $\theta$  (cf. the outward normal). Instead, we simply make use of the main features of such experimental results [1,3,22,30], viz. the observed functional dependence of specific erosion yield  $s_p$

Fig. 3. Erosion yield dependence on particle velocity and angle of incidence (relative to target normal) for unannealed glass target/cast iron erodent ( $d_p = 580 \mu\text{m}$ ) at 300 K (after Finnie [3]).Fig. 4. Erosion yield dependence on particle velocity and angle of incidence (relative to target normal) for unannealed glass target/cast iron erodent ( $d_p = 580 \mu\text{m}$ ) at 300 K (after Finnie [3]).

where  $s_p = s_p(\theta, V_p)$  (i.e. the value of  $s_p$  at  $V_p = V_{p,\text{ew}}$  and  $\theta = 0^\circ$ , and  $t_p = t_p(V_p) = (\pi/6)(V_p)^3/(100)^3 \mu\text{m}^3$  is specific to the projectile/ceramic target system, and the exponent  $n$  on the particle velocity ( $n = d(\ln s_p)/d(\ln V_p)$ ), a value frequently near 2.3) is chosen to fit experimental results, especially in the vicinity of normal incidence,  $\theta = 0^\circ$ . Similarly, the exponent  $l$  on particle volume ( $l = d(\ln s_p)/d(\ln t_p)$ , a value frequently near 1.2) is chosen to best describe available experimental results as a function of erodent particle size  $t_p$ . Note that the indicated dependence on angle of incidence,  $\cos^n(\theta)$ , is already normalized since  $\cos^n(0) = 1$  for any  $n$  (typical values of the exponent  $n$ , not necessarily an integer, will be seen to range between 0.5 and 3.5; see, for example, Fig. 2 and Table 1).

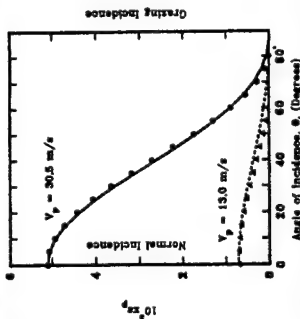
Regarding the  $\theta$ -dependence of erosion yields, the behavior and success of the simple but realistic function  $\cos^n(\theta)$  is shown in Fig. 2. This functional form is seen to fit room temperature erosion rate data obtained from laboratory experiments for a wide variety of combinations of ceramic target material and projectile materials [23,22,31] and will be shown to facilitate the calculation of total erosion rates (Section 2.3, Figs. 3 and 4), especially in the high Stokes number limit. Note that in all cases considered here we assume that no erosion occurs for projectile particles which strike the target surface at grazing incidence ( $\theta = \pi/2 \text{ rad}$ ). Conversely, the most vulnerable angle of incidence ( $\theta = 0^\circ$  radians (*i.e.* normal incidence)) is zero radians (Rosner et al. [29] and Kho et al. [19]) is zero radians (*i.e.* normal incidence). Some best-fit values of the four parameters  $l$ ,  $m$ ,  $n$ , and  $s_{p,\text{ew}}$  which we extracted from available erosion yield measurements for a variety of ceramic targets and erodents (see Section 3), are given in Table 1.

In what follows, cylindrical ceramic target results will be shown for the following representative range of the above-mentioned erosion yield parameter  $m$ :  $0.5 \leq m \leq 3.0$ . These graphs together with our table giving the four parameters  $l$ ,  $m$ ,  $n$ , and  $s_{p,\text{ew}}$  summarizing available ceramic planar target erosion rate data (Table 1), will permit rapid engineering estimates of convex or concave cylinder target erosion rates for preliminary design/optimization purposes for many combinations of particle velocity and angle of incidence.

An attractive feature of this formulation is that the above-mentioned non-dimensional functions  $E$  (Eq. (7)), and  $E$  (Eq. (9)) can be calculated "once-and-for-all" for each target geometry via numerical quadrature. Moreover, these quadratures become particularly straightforward in the important limit of high Stokes number (or  $(\bar{v}_p u_{\text{ew}})^{1/3} \gg 1$ ) (Section 2.4), to which we confine ourselves later in this paper (27–29). The availability of these results will be seen to simplify dramatically the engineering task of predicting local and total erosion rates for, say, ceramic-coated heat exchanger tubes in the cross-flow of ash-laden combustion products, leading edge regions of turbine blades, or target regions of cyclone separators. Illustrative numerical calculations in the high Stokes number limit are given in Section 4.1.

## 2.3. Local and total erosion rate quadrature expressions

Consider first the task of predicting the local erosion rate at some arbitrary angular position  $\theta$  on, say, a convex cylindrical ceramic target (measured from the forward stagnation line, see Fig. 1(a)). The mainstream, of velocity  $U$ , contains the number density  $N_p$  of abrasive particles distributed in size (particle volume) with the normalized size distribution func-

Fig. 2. Dependence of the normalized erosion yield ( $s_p/s_p(\theta=90^\circ)$ ) on angle of incidence (relative to target normal) for unannealed glass target/cast iron erodent ( $d_p = 580 \mu\text{m}$  and  $V_p = 30.5 \text{ m s}^{-1}$ ) at 300 K (after Finnie [3]).

tion  $C_\infty(v)$ . We write the local impingement flux of particles of volume  $\Delta v \pm dv/2$  as  $\eta_{\text{local}}(v, \theta) \cdot UN_p C_\infty(v) dv$ , which corresponds to a volume flux  $v \eta_{\text{local}}(v, \theta) \cdot UN_p C_\infty(v) dv$ .

According to the erosion yield law (Section 2.2), the corresponding contribution to the local erosion rate will be:

$$\epsilon_p(V_p(v, \theta), \beta(v, \theta), v) \eta_{\text{local}}(v, \theta) \cdot UN_p C_\infty(v) dv \quad (3)$$

and the total local erosion rate will therefore be given by the integral of Eq. (3) over the entire particle volume range  $0 \rightarrow \infty$ . Keeping in mind that, for inertial impaction, the integrand (because of  $\eta_{\text{local}}(v, \theta)$ ) is essentially zero below some threshold volume  $V_{\text{crit}}$  corresponding to a critical Stokes number,  $Sk_{\text{crit}} = 1/8$  [31,32], we can write:

$$ER = \int_0^{\bar{V}_p} (V_p(v, \theta), \beta(v, \theta), v) \eta_{\text{local}}(v, \theta) \cdot UN_p C_\infty(v) dv \quad (4)$$

A suitable system-specific characteristic erosion rate will clearly be:

$$(ER)_c = \epsilon_p(U(0, \bar{V}_{\text{crit}}), (\bar{U} V_p U)_\infty) \quad (5)$$

where the product  $(\bar{U} V_p U)_\infty$  will be recognized as the mainstream particle volume fraction  $\phi_{\text{part}}^\infty$ . This implies that it will always be possible to calculate actual target erosion rates from the product relation:

$$ER = (ER)_c \cdot E(\theta, \dots) \quad (6)$$

where, in view of Eqs. (3)–(5), the dimensionless local erosion rate function  $E(\theta, l/m)$  is explicitly given by:

$$E(\theta, \dots) = \int_0^{\bar{V}_p} \frac{\epsilon_p(V_p(v, \theta), \beta(v, \theta), v)}{\epsilon_p(U(0, \bar{V}_{\text{crit}}))} \left[ \frac{v}{\bar{U}} \cdot \eta_{\text{local}}(v, \theta) \cdot C_\infty(v) dv \right] \quad (7)$$

This is an important general result, simplified below for particles large enough to follow straight line trajectories in the vicinity of the ceramic (coated) target.

We now introduce the separable erosion yield law Eq. (2) and note that the first (bracketed) erosion term in the integrand can then be simplified to the product of three dimensionless functions:

$$\left[ \frac{\epsilon_p(V_p(v, \theta), \beta(v, \theta), v)}{\epsilon_p(U(0, \bar{V}_{\text{crit}}))} \right] \cdot \left( \frac{V_p(v, \theta)}{U} \right)^n \cdot \cos^m(\beta(v, \theta)) \cdot \left( \frac{v}{\bar{U}} \right)^l \quad (8)$$

It will be recalled that the shape function  $\cos^m(\beta)$  describing the dependence of erosion yield on angle-of-incident is already normalized. Generally, to complete the calculation of the dimensionless local erosion rate  $E(\theta, \dots)$ , it remains to specify (besides the erosion yield parameters of Table 1) the three inertial impact function:  $V_p(v, \theta)/U$ ,  $\beta(v, \theta)/(m/2)$  and  $\eta_{\text{local}}(v, \theta)$  for the flow geometry at hand.

obtained by using the known exact results of this integral for  $m = 0, 1, 3$  as anchor points in a quadratic interpolation formula (cf. Fig. 6).

### 2.5. Concave target sector of cyclone particle separator

Despite possible complications of re-impingement or “blanketing” (local shielding) (Section 4.3 and Assumption (1)), it is interesting that our present formulation, with only minor modifications, can be used to estimate local and total erosion rates for the concave target area of a cyclone particle separator (Fig. 1(b)). Apart from the fact that direct impingement now only occurs between the angles  $\theta_m$  and  $\pi/2$  (where  $\theta_m = \sin^{-1}[1 - (R_x/R_z)]$ ) in the (worst case) limit of rectilinear particle paths our previous results for  $E(\theta, m)$  still apply, but now the average erosion rate will be  $(ER)_c = \mu_{l+1} \cdot \bar{F}_{\text{lim}}(m; \theta_m)$ , where:

$$\bar{F}_{\text{lim}}(\theta_m; m) = ((\pi/2) - \theta_m)^{-1} \cdot \int_0^{(\pi/2)-\theta_m} \cos^{m+l}(\theta) \cdot d\theta \quad (16)$$

and it will be noted that  $\bar{F}_{\text{lim}}(0; m) = \bar{E}_{\text{lim}}(m)$  (Eq. (15)). Values of  $\bar{F}_{\text{lim}}(\theta_m; m)$  via numerical integration are shown in Fig. 8 for two relevant values of the cyclone geometry parameter  $\theta_m$ . Again, using exact values for the particular cases  $m = 0, 1$ , and 3 as anchor points in a quadratic interpolation formula, we derive the approximate formula:

$$\bar{F}_{\text{lim}}(\theta_m; m) \approx C_0 + C_1 \cdot m + C_2 \cdot m^2 \quad (17)$$

where:

$$C_0 = (1 - \sin(\theta_m)) / ((\pi/2) - \theta_m) \quad (18)$$

$$C_1 = (11/16) - (3/4) \sin(\theta_m) \cos(\theta_m) / ((\pi/2) - \theta_m) \quad (19)$$

$$- (3/4) (1 - \sin(\theta_m)) / ((\pi/2) - \theta_m) \quad (20)$$

$$+ (\sin(4\theta_m) / (24((\pi/2) - \theta_m))) \quad (21)$$

$$+ \sin(4\theta_m) / (192((\pi/2) - \theta_m)) \quad (22)$$

$$C_2 = (1/3) (1 - \sin(\theta_m)) / ((\pi/2) - \theta_m) + (1/4) \quad (23)$$

$$+ \sin(\theta_m) \cos(\theta_m) / ((\pi/2) - \theta_m) \quad (24)$$

$$- \sin(2\theta_m) / (24((\pi/2) - \theta_m)) \quad (25)$$

$$- \sin(4\theta_m) / (192((\pi/2) - \theta_m)) - (3/16) \quad (26)$$

Eq. (17) is plotted in Figs. 7 and 8 (for  $\theta_m$  equal to 0.25/27 and 0.5/236 rad, respectively) and compared with the corresponding numerical integrations of Eq. (16). However, since, often,  $\theta_m \ll 1$ , we can also use the convenient alternative:

$$\bar{F}_{\text{lim}}(\theta_m; m) \approx \bar{E}_{\text{lim}}(m) - (2/\pi) \cdot [1 - \bar{E}_{\text{lim}}(m)] \cdot \theta_m \quad (27)$$

$$- (2/2\pi)^2 \cdot [1 - \bar{E}_{\text{lim}}(m)] \cdot \theta_m^2 \quad (28)$$

where  $\bar{E}_{\text{lim}}(m)$  is the corresponding complete upwind cylinder surface erosion rate function.

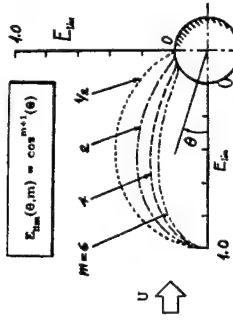


Fig. 6. Dependence of the function  $\bar{E}_{\text{lim}}(m)$  on the erosion parameter  $m$ : windward surface of a circular cylinder in crossflow.

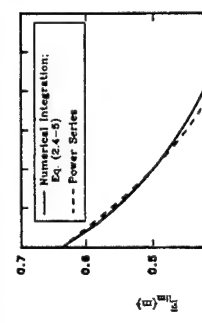


Fig. 7. Polar plot of normalized local erosion rates,  $E_m(m)$ , on upwind surface of ceramic (coated) circular cylinders in crossflow.

Fig. 8. Polar plot of normalized local erosion rates,  $E_m(m)$ , on upwind surface of ceramic (coated) circular cylinders in crossflow.

Fig. 8. Dependence of the function  $\bar{E}_{\text{lim}}(m)$  on the erosion parameter  $m$ : windward surface of a circular cylinder in crossflow.

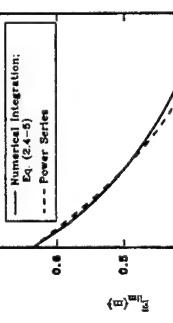


Fig. 8. Dependence of the function  $\bar{E}_{\text{lim}}(m)$  on the erosion parameter  $m$ : windward surface of a circular cylinder in crossflow.

### 2.4. Inertial impaction for a cylindrical target in cross-flow: Limiting case of very large Stokes numbers ( $Sk \gg 1$ )

For the general case [28,29], we need to invoke inertial impaction correlations of individual particle trajectory calculations to estimate impinging particle frequencies, impact velocities and angles [33,34]. But, in the limit where most particles in the mainstream population are so large that they follow nearly straight line paths (for Stokes numbers based on a particle of volume  $v$ , satisfying the inequality:  $Sk_v \gg 1$ , the special case to which we restrict ourselves here), all particles will impact the circular cylinder at the velocity  $V_p \approx U$  with local incidence angle  $\theta_l \approx \theta$ . In this limit, the general relations for local impingement efficiency,  $\eta_{\text{local}}$ , and maximum angle,  $\theta_{\text{max}}$ , experiencing impaction on a circular cylinder reduce to:

$$\eta_{\text{local}}(v, \theta) \rightarrow \cos(\theta) \quad (10)$$

$$\theta_{\text{max}} \rightarrow \pi/2 \quad (11)$$

Inspection of the general quadrature expression  $E(\theta, \dots)$  (Eq. (6)) reveals that when  $(\bar{U} V_p U)_\infty \gg 1$  then:

$$\lim E(\theta, m, l) = E_{\text{lim}}(\theta, m, l) = \mu_{l+1} \cdot \cos^{m+l}(\theta) \quad (12)$$

Here

$$\mu_{l+1} = \left\{ \int_0^{\pi/2} v^{l+1} \cdot C_\infty(v) dv \right\}^{1/(l+1)} \quad (13)$$

where the factor  $\{ \}$  will be recognized as  $\bar{E}_{\text{lim}}(m)$  for the special case when all particles in the mainstream have the same size,  $\bar{U}_m$ . This function can be obtained by carrying out the indicated numerical integration, with results (for  $0 < m < 3.0$ ) given in Fig. 6. As a useful approximate formula for making future calculations we suggest the power series:

$$\begin{aligned} \bar{E}_{\text{lim}} \approx & (2/\pi) + [(11/16) - (8/(3\pi))] \cdot m \\ & + [(2/(3\pi)) - (3/16)] \cdot m^2 \end{aligned} \quad (15)$$

normalized erosion yield,  $f(\theta)$ , is calculated by dividing the erosion yield,  $\epsilon_p$ , by the erosion yield at normal incidence (i.e. at  $\theta = 0^\circ$ ), all necessary quantities being held constant. When erosion yield data at normal incidence were not available (as in Kairns et al. [1]), data extrapolation was utilized to estimate  $\epsilon_p$  at  $\theta = 0^\circ$ .

Table 1 summarizes the results of our analysis of available erosion yield data for a variety of ceramic target material/erodent systems near 300 K; best-fit values of the four erosion parameters,  $l$ ,  $m$ ,  $n$ , and  $\epsilon_{p,\text{ref}}$  are provided. Note that our reported values of  $\epsilon_{p,\text{ref}}$  (cf. Eq. (2)) pertain to particle reference velocity,  $V_{\text{ref}} = 100 \text{ m s}^{-1}$ , a reference particle size,  $d_{p,\text{ref}} = 100 \mu\text{m}$ , and normal incidence.

Fig. 2 shows the dependence of erosion yield  $\epsilon_p$  on particle velocity  $V_p$  and angle of incidence  $\theta_p$  (relative to target normal) for the system: unannealed glass target/cast iron erodent ( $d_p = 580 \mu\text{m}$ ) at 300 K. It is clear from this figure that our results (using Eq. (2) and Table 1) are in excellent agreement with the corresponding experimental results generated by Frinnie [3]. Similarly, Fig. 3 shows the experimental erosion yield data for "dead-burned" dolomite particles impacting on a 96% high-purity alumina castable target at various angles of incidence and mainstream velocities [1]. Also shown are the erosion yields calculated using the chosen erosion yield law (Eq. (2)) and the four parameters reported in Table 1. Note that the erosion yield increases noticeably as the particle velocity increases from  $10.1 \text{ m s}^{-1}$  to  $14.3 \text{ m s}^{-1}$ . Furthermore, the experimental data and our simple four-parameter model representation are in acceptable agreement. For example, the absolute deviation between the experimental and predicted erosion yield for incidence angles bounded between  $\theta = 0^\circ$  and  $\theta = 45^\circ$  is  $\leq 10\%$  (at  $\theta = 75^\circ$ , where much less erosion is expected, the absolute deviation is about 40%). Additional satisfactory results were obtained for the older types of castable target/erodent systems tested by Kairns et al. [1].

Our analysis of these cases and similar erosion data presented in Table 1 demonstrates the engineering utility of our proposed erosion data representation technique. Combined with local impaction frequency calculations (Section 3.2), these erosion yield parameters will be seen to simplify dramatically the engineering prediction of local and total erosion rates.

### 3.2. Enlargement of Table 1 based on available relative erosion rate data

#### 3.1. Use of erosion test rig data for planar targets with known impingement conditions

To utilize this simplified formulation (see Section 2) and conveniently summarize experimental erosion yield data provided in the literature, a practical procedure is required to determine best-fit values of the erosion yield parameters:  $l$ ,  $m$ ,  $n$ , and  $\epsilon_{p,\text{ref}}$  associated with any given set of ceramic erosion yield data (e.g. iso-velocity  $\epsilon_p$  vs. angle-of-incidence data). In this work, the dimensionless absolute erosion yield,  $\epsilon_p$ , is defined as the average volume of ceramic target removed per unit volume of impacting erodent particle. The

where  $\lambda$  is the complement of the angle between the flow direction and the cylinder axis. Therefore, all previous calculations apply if we merely introduce the additional spanwise-flow correction factor:  $\cos^m(\lambda)$ .

#### 2.7. Correction factor for mainstream erodent particles distributed in size according to the Rosin-Rammler function

For suspended particles in the size range capable of impact and erosion damage, a common form of size distribution function  $C_\infty(v)$  has the property:

$$\left\{ \int_v^\infty C_\infty(v) dv \right\} / (\bar{v}_\infty) = \exp \left[ (v/v_{\text{ref}})^n \right] \quad (21)$$

where the (Rosin-Rammler) exponent  $n$  is an important "monodispersity" (inverse-spread) parameter for the population and  $v_{\text{ref}}$  is any convenient reference particle volume (including  $v_{\text{ref}} = 1$ ). For the moment of the normalized size distribution function  $C_\infty(v)$ , the useful result [29]:

$$\mu_{l+1} = (v_{\text{ref}}/v_{\text{ref}})^l \cdot \Gamma(1 + (l/n)) \quad (22)$$

where  $\Gamma(1 + (l/n))$  is the gamma function of the indicated argument  $1 + (l/n)$ , which can also be written  $(l/n)!$ , in terms of the factorial function. However, when the spread parameter  $n$  is less than unity, as has been reported for the impacting portion of many abrasive powder populations, this result must be increased because of the required introduction of a small-size (volume) "cut-off". As an example, for pulverized coal a typical  $n$  value is 0.4 (i.e. 1.2/3). Thus, if  $l = 1.2$  (Table 1)  $(l/n)! = 3! = 6$ . With the above-mentioned "cut-off correction", this leads to  $\mu_{l+1} = 9.6$ , corresponding to almost a one-decade erosion rate increase due to mainstream polydispersity (for the particular case:  $l = 1.2$ ,  $\nu = 0.4$ ).

#### 3. Procedure to determine best-fit values of the erosion parameters $l$ , $m$ , $n$ , and $\epsilon_{p,\text{ref}}$ from available erosion yield data

The present reformulation of the canonical erosion problem, together with our tabulations of parameters based on available experimental data (Section 3.1), lends itself to augmentation based on the existence of relative erosion rate data also in the literature. As an interesting example, Hansen [35] reported the relative erosion rates of some 80 target materials exposed at normal incidence, and at two temperature levels: 298 K and 973 K, to  $27 \mu\text{m}$  diameter alumina particles at a velocity of  $170 \text{ m s}^{-1}$ . Hansen chose Stellite 6B

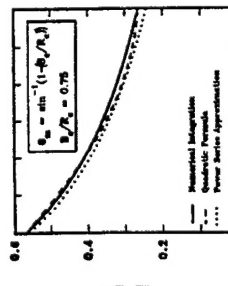


Fig. 7. Dependence of the cyclone target erosion function on the erosion parameter  $m$  for a cyclone geometry with  $B_r/R_c = 0.75$ ; impingement sector of cyclone inner walls (Figs. 7 and 1(b)).

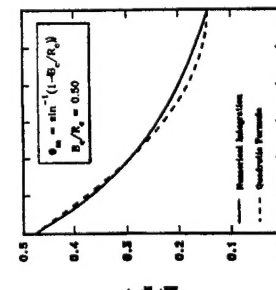


Fig. 8. Dependence of the cyclone target erosion function on the erosion parameter  $m$  for a cyclone geometry with  $B_r/R_c = 0.50$ ; impingement sector of cyclone inner walls (Fig. 1(b)).

Fig. 7 also shows a comparison between the series approximation given by Eq. (19) and the numerical integration using Eq. (16) for the case  $\theta_p = 0.2572 \text{ rad}$ . Since Eq. (19) becomes less accurate when  $\theta_p$  does not satisfy the inequality  $\theta_p < 1$ , Eq. (17) would be more appropriate to use.

This concludes our derivation of the formulae needed to predict all ceramic cylinder target erosion rates of interest in this paper. Use of these dimensionless functions to estimate local and total cyclone target section absolute erosion rates (e.g. mm per year recession) is illustrated in Section 4.1.

#### 2.6. Correction factor for departures from pure crossflow

It is possible to include commonly encountered cases in which the configuration departs from "pure crossflow", i.e. the erodent-containing stream direction and target cylinder axis are not perpendicular. Then, in the worst-case limit of rectilinear particle trajectories:

$$\cos(\theta) = \cos(\lambda)\cos(\theta)$$

normalization yield,  $f(\theta)$ , is calculated by dividing the erosion yield,  $\epsilon_p$ , by the erosion yield at normal incidence (i.e. at  $\theta = 0^\circ$ ), all necessary quantities being held constant. When erosion yield data at normal incidence were not available (as in Kairns et al. [1]), data extrapolation was utilized to estimate  $\epsilon_p$  at  $\theta = 0^\circ$ .

Table 1 summarizes the results of our analysis of available erosion yield data for a variety of ceramic target material/erodent systems near 300 K; best-fit values of the four erosion parameters,  $l$ ,  $m$ ,  $n$ , and  $\epsilon_{p,\text{ref}}$  are provided. Note that our reported values of  $\epsilon_{p,\text{ref}}$  (cf. Eq. (2)) pertain to particle reference velocity,  $V_{\text{ref}} = 100 \text{ m s}^{-1}$ , a reference particle size,  $d_{p,\text{ref}} = 100 \mu\text{m}$ , and normal incidence.

Fig. 2 shows the dependence of erosion yield  $\epsilon_p$  on particle velocity  $V_p$  and angle of incidence  $\theta_p$  (relative to target normal) for the system: unannealed glass target/cast iron erodent ( $d_p = 580 \mu\text{m}$ ) at 300 K. It is clear from this figure that our results (using Eq. (2) and Table 1) are in excellent agreement with the corresponding experimental results generated by Frinnie [3]. Similarly, Fig. 3 shows the experimental erosion yield data for "dead-burned" dolomite particles impacting on a 96% high-purity alumina castable target at various angles of incidence and mainstream velocities [1]. Also shown are the erosion yields calculated using the chosen erosion yield law (Eq. (2)) and the four parameters reported in Table 1. Note that the erosion yield increases noticeably as the particle velocity increases from  $10.1 \text{ m s}^{-1}$  to  $14.3 \text{ m s}^{-1}$ . Furthermore, the experimental data and our simple four-parameter model representation are in acceptable agreement. For example, the absolute deviation between the experimental and predicted erosion yield for incidence angles bounded between  $\theta = 0^\circ$  and  $\theta = 45^\circ$  is  $\leq 10\%$  (at  $\theta = 75^\circ$ , where much less erosion is expected, the absolute deviation is about 40%). Additional satisfactory results were obtained for the older types of castable target/erodent systems tested by Kairns et al. [1].

Our analysis of these cases and similar erosion data presented in Table 1 demonstrates the engineering utility of our proposed erosion data representation technique. Combined with local impaction frequency calculations (Section 3.2), these erosion yield parameters will be seen to simplify dramatically the engineering prediction of local and total erosion rates.

### 3.2. Enlargement of Table 1 based on available relative erosion rate data

The present reformulation of the canonical erosion problem, together with our tabulations of parameters based on available experimental data (Section 3.1), lends itself to augmentation based on the existence of relative erosion rate data also in the literature. As an interesting example, Hansen [35] reported the relative erosion rates of some 80 target materials exposed at normal incidence, and at two temperature levels: 298 K and 973 K, to  $27 \mu\text{m}$  diameter alumina particles at a velocity of  $170 \text{ m s}^{-1}$ . Hansen chose Stellite 6B

#### 4. Implications, applications, and generalizations

##### 4.1. Direct use to predict erosion rate behavior

The following two numerical examples illustrate the utility of our reformulation of the problem of predicting erosion

<sup>1</sup>In light of the more direct  $\epsilon_{p,\text{ref}}$  estimates included in our Table 1, these tentative estimates for hot-pressed  $\text{Si}_3\text{N}_4$  and SIC must be viewed with caution because of a possible (uncorrected) erodent particle size effect for the 27  $\mu\text{m}$  diam  $\text{Al}_2\text{O}_3$  erodent/ $\#304$  SS planar target in Hansen's (incompletely documented/characterized) test rig.

rates for the canonical geometry of a circular cylinder (sector).

#### 4.1.1. Example 1: Leading edge of a gas-turbine stator blade

We calculate here the erosion rate (units: mm per year) of an initially 0.25 mm thick protective ceramic coating on the leading edge of a gas-turbine stator blade in a pressurized fluidized bed combustor (PFBC) combined cycle unit. Suppose that the gas turbine blades are subjected to a hot gas stream containing suspended ash at operating temperature and pressure of about 1000 K and 1 atm, respectively. Assume, further, that the ash particles have a mean particle diameter  $d_p$  of, say, 40  $\mu\text{m}$ , the mainstream gas velocity is about 300 m  $\text{s}^{-1}$ , and the particle loading is 35 ppm (mass of eroded/mass of gas). Let the four erosion yield parameters describing the blade's protective ceramic coating be:  $I = 1.2$ ,  $m = 0.6$ ,  $n = 2.8$ , and  $\epsilon_{p,\text{ref}} = 7.5 \times 10^{-7}$ . If the intrinsic density of each eroded particle is  $3.17 \times 10^3 \text{ kg m}^{-3}$  and that of the hot gas stream is  $3.44 \text{ kg m}^{-3}$  (at 1000 K and 1 atm), then the mainstream volume fraction,  $\phi_{p,\text{m}}$ , of eroded particles will be  $(3.44)(35 \times 10^{-6})/(3.17 \times 10^3) = 3.8 \times 10^{-8}$  (i.e. about 0.04 ppm). Also, the value of the erosion parameter corrected to actual gas turbine operating conditions,  $\epsilon_c(U(0,d_p))$ , will be  $(7.5 \times 10^{-7})(300/100)^{2.8} \cdot (40/100)^{3/12} = 6.0 \times 10^{-7}$ .

The characteristic erosion rate,  $(ER)_c$ , can then be calculated from the product  $\epsilon_c(U(0,d_p))$  (mainstream volume fraction), (mainstream velocity)  $= (6.0 \times 10^{-7})(3.8 \times 10^{-8})(300)/(8760)(3600) = 0.22 \text{ mm y}^{-1}$ . The local erosion rate can be calculated by multiplying  $(ER)_c$  by  $E_{\text{loc}}(\theta; m)$ , i.e. by  $\cos^{n+1}(\theta)$ , and the maximum local erosion rate (here at  $\theta = 0$ ) would be 0.22 mm  $\text{y}^{-1}$ . Finally, the mean erosion rate can be calculated by multiplying  $(ER)_c$  by the value of  $\bar{E}_{\text{loc}}(m)$ , estimated at  $m = 0.6$  using Eq. (6) or Eq. (15). Therefore, the mean erosion rate of the turbine blade's leading edge would be  $(0.22)(0.55) = 0.12 \text{ mm y}^{-1}$ . Based on these estimated erosion rates, one can, for example, decide on the necessary replacement frequency of the ceramic protective coating system (e.g. in this example about every 2 years of continuous operation).

#### 4.1.2. Example 2: Refactory-lined cyclone

Consider a refractory-lined cyclone separator such as that used with a CFBC unit operating at a pressure near 1 atm. Assume that the cylinder concave target liner is aluminum cement and pellet insulating refractory concrete (density  $0.80 \text{ g cm}^{-3}$ ). Consider a CFBC cyclone operated at an inlet gas velocity of approximately  $30 \text{ m s}^{-1}$  and a gas temperature of 1270 K. Therefore, for this numerical example, we assume that the cyclone liner is exposed to  $30 \text{ m s}^{-1}$  solid/gas stream of density  $1.18 \text{ kg m}^{-3}$  containing sand particles ( $\text{SiO}_2$ ) with an average diameter of  $150 \mu\text{m}$  and intrinsic erodent density  $2.4 \text{ g cm}^{-3}$ . Sand is chosen to represent the main erodent since it is the hardest material found among the minerals in a CFBC cyclone. Furthermore, assume that the solids-containing gas stream has a particle ( $\text{SiO}_2$ ) mass loading

of 200 ppm. Our objective (in this example) is to predict the maximum local ceramic liner erosion rate (mm  $\text{y}^{-1}$ ), as well as the mean erosion rate over the target area bounded between  $\theta = 30^\circ$  and  $\theta = 90^\circ$  (Fig. 1(b) and Fig. 8).

The first step is to calculate the characteristic erosion rate ( $ER$ ). For this purpose, the value of the erosion yield  $\epsilon_p(U(0,d_p))$  at  $V_p = U = 30 \text{ m s}^{-1}$  and  $d_p = 150 \mu\text{m}$  can be calculated as follows. The erosion parameters ( $I$ ,  $m$ ,  $n$ , and  $\epsilon_{p,\text{ref}}$ ) for the insulating refractory/concrete/sand particle system can be estimated using the 300 K erosion yield data summarized in Table 1. Pertinent values of the erosion yield parameters are seen to be  $I = 1.2$ ,  $m = 0.5$ ,  $n = 2.5$ , and  $\epsilon_{p,\text{ref}} = 1.45 \times 10^{-3}$  (evaluated at  $d_p = 100 \mu\text{m}$  and  $V_p = 100 \text{ m s}^{-1}$ ). Then,  $\epsilon_c(U(0,d_p))$  for this application  $= (1.45 \times 10^{-3})(150/100)^{3/12}(30/100)^{2.5} = 3.91 \times 10^{-4}$ . The mainstream volume fraction of the sand particles will be  $(1.18)(2 \times 10^{-4})/(2400) = 0.98 \times 10^{-7}$  (i.e.  $\approx 0.1$  ppm) and  $(ER)_c = \epsilon_c(U(0,d_p))$  (mainstream volume fraction) (mainstream velocity)  $= (3.91 \times 10^{-4})(0.98 \times 10^{-7})(30)(10^3)/(8760)(3600) \approx 36 \text{ mm y}^{-1}$ . The maximum local erosion rate can be calculated using the dimensionless local erosion rate function  $E_{\text{loc}}(m)$  evaluated at  $\theta = \theta_m$  and, therefore,  $E_{\text{loc}}(\theta_m) = \cos^{n+1}(\theta_m) = \cos^{1.5}(30^\circ) = 0.806$ . Thus, the maximum local erosion rate is  $(36)(0.806) = 29 \text{ mm y}^{-1}$ . Furthermore, the mean erosion rate can then be calculated from  $(ER)_c$  and the function  $\bar{E}_{\text{loc}}(\theta_m; m)$  evaluated at  $\theta_m = 30^\circ$  and  $m = 0.50$  using Fig. 8 or Eq. (17). The value of  $\bar{E}_{\text{loc}}(\theta_m; m)$  can be found from Fig. 8 to be equal to 0.368 and, therefore, the mean erosion rate under these conditions would be  $(36)(0.368) = 13 \text{ mm y}^{-1}$  (evaluated over the target area bounded between  $\theta = 30^\circ$  and  $\theta = 90^\circ$ ).

Note that in these numerical examples we evaluated target erosion rates at room temperature (for which the necessary data were available) rather than at actual operating temperatures. Often, this assumption is conservative since, for many refractories, material loss decreases as temperature increases (Liebhärd [24]; see also Section 4.4). This was true for nearly 2/3 of the ceramic target/erodent systems examined at 298 K and 973 K by Hansen [35]. However, a notable exception was hot-pressed (Norton) SiC exposed to alumina dust (which at 973 K eroded 3.7 times as fast as at 298 K).

#### 4.2. Indirect use to infer parameters in the erosion yield law

Inspection of our universal results (Section 2, Figs. 4 and 5) reveals that  $(ER)_c$ , and/or the calculated quantities  $\bar{E}_{\text{loc}}$ ,  $E_{\text{loc}}$ , and/or  $\epsilon_{p,\text{ref}}$  appearing in the erosion yield law. In these regimes an observation of these quantities for a cylinder in a known test environment could clearly be used to extract rational estimates of those parameters least well known—perhaps  $m$  for a ceramic never previously studied in a well-characterized erosion test rig. This might be a reasonable

provisional method for making extrapolations to related environmental conditions, including ultimately predicting erosion damage on yet more complex ceramic shapes (e.g. a ceramic coated turbine stator blade) via particle trajectory analysis.

#### 4.3. Examination of approximations

Confidence in the validity of most, if not all, of our underlying assumptions can be generated based on the observations collected in Rosner et al. [28-29]. In some cases we are led to interesting questions which appear to remain open, and warrant further examination. For the present, we briefly highlight the following underlying assumptions:

##### 4.3.1. Locally planar target erosion behavior

The essential validity of Assumption (1) was experimentally demonstrated by carefully measuring the shape change of initially circular cylinder metal targets [37]. Because of the indicated radius of curvature disparity, this assumption can only be invalidated by large effects of stress, or anisotropy (see Assumption (6) and Section 4.4), both of which are not considered here.

#### 4.3.2. Engineering applicability of available erosion yield data

Most erosion rate predictions for, say, combustion turbine or boiler applications have been based on the premise that erosion yield data can be invoked in situations where particles actually arrive simultaneously over a wide band of velocities and angles of incidence. Indeed, this premise underlies the development/use of such erosion test rigs. However, if the erosion mass loss process is not simply a single impact phenomenon this (usually implicit) additivity or uncoupling assumption should probably be examined more critically, perhaps based on the erosion rate experiments involving e.g. pairs of incidence angles. We are presently unaware of such experimental tests of additivity in erosion situations.

Another important coupling phenomenon, which apparently has not been systematically studied, is the possible protective effect of the simultaneous acquisition of much smaller particles (or even condensed vapor) on the component whose erosion is of concern (see, for example, Rosner et al. [27-30]).

#### 4.3.3. Neglect of particle-particle interactions and rebound phenomena

In most of the applications of concern here, the volume fraction of suspended particles,  $\phi_{p,\text{m}}$ , is small enough (often of order  $10^{-6}$ ) to render particle-particle interaction effects in the vicinity of a convex target negligible. Indeed, if one views the particle flow field as if there were no carrier gas (e.g. consider the limit  $Sik \rightarrow \infty$ , with elastic rebound from the target surface) this particle gas flow would correspond to a Knudsen number (ratio of mean-free-path to target transverse dimension  $L$ ) of the order of  $(2/3)(\phi_p)^{-1} \cdot (d_p/L)$ , which, if  $L \approx 1 \text{ cm}$ , is about  $1.4 \times 10^3$  for our present numer-

ical example (Section 4.1). For convex targets, this value is certainly large enough to justify the assumption of free-particle flow, even if every eroded particle rebounds. We are also neglecting erosion caused by particles that re-impinge on the same target after at least one previous impact event. The situation is less clear for concave targets, including our example of the target zone of a cyclone separator (Fig. 1(b)). In such cases, particle-particle interaction effects near the target would be expected to set in at much lower  $\phi_{p,\text{m}}$  values.

#### 4.3.4. Roughness and target shape evolution

We have explicitly considered cases in which the asymptotic roughness associated with (quasi) steady state erosion is small on the scale of the overall body dimension (for a circular cylinder, say,  $d_s/2$ ), as must be the cumulative surface recession (cf. the numerical example in Section 4.1). Indeed, this is fully compatible with the erosion yield data being used, which is itself averaged over long times (many impacts during the constant erosion rate period). However, it is also possible to extract from the polar plots of  $E(\theta, m)$  what might be called the "shape evolution tendency" of the target. In contrast to the case of metal target erosion, which revealed an interesting tendency to make an initially circular cylindrical leading edge (nose-region) wedge-shaped (sharp) as time proceeds, Fig. 4 reveals that ceramic (coated) cylinders will tend to become blunter with time. Examples of shape evolution (in which Assumption (5) is relaxed) are contained in Rosner et al. [39].

#### 4.4. Generalizations

It is useful to comment upon some valuable generalizations of our results in order to find ways to deal with more complex situations than those described in Section 2.1.

#### 4.4.1. Arbitrary Stokes numbers

If the mean particle size,  $d_{p,\text{m}}$ , of the mainstream erodent particle population is not much greater than the critical size,  $d_{p,\text{c}}$ , for the onset of inertial impact in the prevailing aerodynamic environment then the rectilinear trajectory simplification breaks down. However, these cases are still tractable by making use of the correlated results of particle trajectory calculations for the geometry in question [28, 29, 32, 38, 40].

#### 4.4.2. Abrasive particle blends

It is tempting to conjecture that if, as common, the suspended particle population is actually a blend of several populations of rather different erosion propensity, the total erosion rate can be simply estimated as the sum of contributions from each sub-population. We are unaware of this plausible approach to estimate the erosion of ceramic targets in mixed erodent streams has yet been put to an adequate experimental test.

#### 4.4.3. Quasi-steady application of steady-state results

In applications where the dust loading and gas stream conditions are not constant but, yet, change sufficiently slowly on the time scale  $(d_p/2)/U$  one can justifiably treat the total surface recession as the result of target exposure to a sequence of steady environments and summing their effects. In such cases (EZR),  $E_{\text{lim}}(\theta, m)$ , and  $\bar{E}_{\text{lim}}(m)$  provided here will be slowly varying, but the functions  $\cos^n(\theta)$  will not quite be the same at all impact velocities, another complexity that could be straightforwardly introduced into our general quadrature procedure.

#### 4.4.8. Cylindrical targets machined from anisotropic monoliths

In such cases, the four above-mentioned erosion yield parameters  $l$ ,  $m$ ,  $n$ , and  $\epsilon_{p,\text{ref}}$  will generally exhibit a non-negligible dependence on the angle between the principal axes intrinsic to the material anisotropy and the local target surface outward normal.

#### 4.4.5. Quasi-steady shape evolution

The present approach can clearly be applied to other simple target shapes, including spheres, cones, nozzle entrances, pipe elbows, etc. As shown above (Section 2.6), it is also possible to correct for departures from the pure crossflow configuration, irrespective of  $Sik$ .

#### 4.4.6. Implicit effects (temperature, reducing environments, stress, etc.)

The framework provided by the present analysis may allow

several environmental effects (e.g. effects of temperature

level to implicitly included in the appropriate values of

the four erosion yield parameters  $l$ ,  $m$ ,  $n$ , and  $\epsilon_{p,\text{ref}} = \epsilon_p(V_p, \theta, d_p, \rho)$  where, say,  $V_p = 100 \text{ m s}^{-1}$  and

$d_p = 100 \mu\text{m}$ ) for particular combinations of projectile/

ceramic target materials (irrespective of whether an adequate

theory is yet available to anticipate or extrapolate such

effects). Another potentially important variable (evidently

not adequately considered in previous erosion rate measure-

ments) is the state of stress in the target material surface. For

example, one would expect pre-existing tensile stresses to

influence measured erosion yields, and hence the above-men-

tioned four parameters. However, we anticipate erosion/cor-

rosion situations which will require more fundamental

generalizations of the present approach, e.g. when the

$\cos^n(\theta)$  law becomes qualitatively incorrect at sufficiently

high target temperatures.

#### 4.4.7. Velocity exponent insensitivity to angle-of-incidence and erodent particle size

The separability of  $V_p$ ,  $\theta$ , and  $d_p$  effects in the erosion

yield law  $\epsilon_p(V_p, \theta, d_p, \rho)$  (Eq. (2)) significantly reduces the

<sup>3</sup> For the upwind portion of a stationary ceramic (coated) sphere, it is easy to show that (when  $\kappa_{r+1} = 1$ )  $E_{\text{lim}}(\theta, m) = \cos^{n-1}(\theta)$  and hence  $\bar{E}_{\text{lim}} = (m+2)^{-1}$ . Similarly, our present results

#### Appendix A. Nomenclature

$A$	width of cyclone inlet (Fig. 1 (b))
$B_n$	normalized mainstream particle size distribution function
$C_m(v)$	particle diameter
$d_p$	target diameter (Fig. 1) (a)
$d_p$	characteristic erosion rate associated with mainstream abrasive particle volume flux if all particles struck the ceramic solid target at normal incidence with (mainstream) velocity $U$
$E(\theta, \dots)$	dimensionless local erosion rate function (Eq. (7))
$E_{\text{lim}}$	maximum (peak) local erosion rate; occurring at angular position $\theta = 0^\circ$ (Fig. 1(a)) or $\theta_m$ (Fig. 1(b))
$E_{\text{max}}$	average dimensionless erosion rate function; Eq. (9) where $Sik \rightarrow \infty$
$F_{\text{lim}}(\theta, m)$	normalized erosion yield: $= \epsilon_p / (\epsilon_p$ evaluated at $\theta = 0^\circ$ ) (Fig. 4)
$F_{\text{lim}}(\theta_m, m)$	cyclone target dimensionless erosion function; Eq. (16)
$f(\theta)$	transverse reference length for target (4 for circular cylinder, Fig. 1 (a))
$L$	dimensionless exponent which describes the sensitivity of erosion yield to projectile particle size (volume, $v_p$ )
$m$	dimensionless exponent appearing in $\cos^n(\theta)$ representing sensitivity of erosion yield to angle of incidence $\theta$ , (measured with respect to the local target normal)
$n$	dimensionless exponent representing sensitivity of erosion yield to projectile incident velocity $V_p$
$N_p$	number density of abrasive particles
$R_c$	cyclone separator inner wall radius (Fig. 1 (b))
$Sik$	particle Stokes number; $f_p / (d_p/2/U)$ [31,32]
$t_p$	particle stopping time
$U$	mainstream velocity
$v_p$	particle volume $= (\pi/6) \cdot d_p^3$
$w_p$	reference particle volume $= (\pi/6) \cdot d_p^3$ ; with $d_p = 100 \mu\text{m}$
$\bar{v}_w$	mean particle size (volume) in mainstream
$\bar{V}_p$	particle impact velocity
$V_{p,\text{ref}}$	reference particle impact velocity ( $\approx 100 \text{ m s}^{-1}$ here)
$\epsilon_p$	dimensionless erosion yield per particle impact (defined as average volume of ceramic target removed per unit volume of impacting erodent particle)
$\epsilon_p$	evaluated at $V_p = 100 \text{ m s}^{-1}$ , $\theta = 0^\circ$ , and $v_p$ corresponding to $d_p = 100 \mu\text{m}$
$\omega_p$	particle mass loading in mainstream ( $\approx \text{kg erodent/kg gas when } \omega_0 \ll 1$ )

#### Acknowledgements

This research was supported, in part, by AFOSR (Grant 94-1-0143) and DOE/PETC (Grant DE-FG-2290PC90099), as well as the Yale HTCRE Laboratory Industrial Affiliates (ALCOA, Dupont, Shell and Union Carbide/Prairair Corporations). It is also a pleasure to acknowledge helpful discussions and/or correspondence with J. Fernandez de la Mora, M.J. Labowsky, P. Tandon, R.C. Tucker, Jr., and A.G. Konstandopoulos.

mainstream particle volume fraction:  $(\bar{v}/V_p)_e$ .

particle incidence angle:  $\theta = 0^\circ$  refers to normal incidence, and  $\theta = 90^\circ$  refers to grazing incidence (see Fig. 1(a))

angular position on target measured from the stagnation line (Fig. 1) minimum angle (Fig. 1(b)) experiencing cyclone inlet particle erosion (in the large Stokes number limit)

local impingement efficiency (Section 2.3) complement of the angle between the flow direction and the cylinder axis

$\theta_m$  gamma function of the indicated argument Eq. (21)

$\mu + 1$  Rosin-Rammler exponent shown in Eq. (21)

moment function defined by Eq. (13) circulating fluidized bed combustor limit

PFBC pressurized fluidized bed combustor relative erosion factor (Section 3.2 and Hansen [35])

O() order of magnitude operator factorial function

$9.6 \times 10^{-4}$ , etc. (see Table 1)

## References

- [1] D.L. Kealim, W.C. Yang and W.G. Vaux, Design of refractories for coal gasification and combustion systems, *EPRI AF-151*, Electric Power Research Institute, Palo Alto, CA, July 1979.
- [2] D.R. Reid and E. Ruth, Abrasion resistance of refractories, *Ceramic Bulletin*, 40 (7) (1961) 452-455.
- [3] I. Finnie, Erosion of surfaces by solid particles, *Wear*, 3 (1950) 87-103.
- [4] C.R. Venable, Erosion resistance of ceramic materials for petroleum refinery applications, *Ceramic Bulletin*, 38 (7) (1959) 365-368.
- [5] S.T. Wood, Erosion resistance coatings for steam turbines, *EPRI CS-54/1*, Electric Power Research Institute, Palo Alto, CA, 1987.
- [6] T. Bellizzi, Shoot for more durable, less costly refractory in CFB units, *Power* (February 1994) 69-71.
- [7] G.L. Barnes and R.R. Riley, Abrasion test for refractories, *Ceramic Bulletin*, 46 (9) (1967) 824-826.
- [8] R.E. Dial, Refractories for coal gasification and liquefaction, *Ceramic Bulletin*, 54 (7) (1975) 640-643.
- [9] P.A. Engel, *Impact Wear of Materials*, Tribology Series 2, Elsevier, Amsterdam, 1978.
- [10] R.G. Houde, Consider advanced ceramics for valve seats, *Chemical Engineering Progress*, (May 1994) 64-67.
- [11] S.S. MacAdam and J. Struttier, Particle impact and impact distribution within a fluidized bed combustor environment, *Wear*, 141 (1991) 373-394.
- [12] J.H. Nelson and A. Gilchrist, Erosion by a stream of solid particles, *Wear*, 11 (1968) 111-122.
- [13] J.H. Nelson and A. Gilchrist, An experimental investigation into aspects of erosion in rock motor tail nozzles, *Wear*, 11 (1968) 123-143.
- [14] D.E. Rosner, *Transport Processes in Chemically Reacting Flow Systems*, Butterworth-Heinemann, Stoneham, MA, 1986.

$\phi_{\theta} = \theta_i - \theta$  mainstream particle volume fraction;  $(\bar{v}/V_p)_e$  particle incidence angle;  $\theta = 0^\circ$  refers to normal incidence, and  $\theta = 90^\circ$  refers to grazing incidence (see Fig. 1(a))

$\theta$  angular position on target measured from the stagnation line (Fig. 1) minimum angle (Fig. 1(b)) experiencing cyclone inlet particle erosion (in the large Stokes number limit)

$\theta_m$  local impingement efficiency (Section 2.3) complement of the angle between the flow direction and the cylinder axis

$\Gamma$  gamma function of the indicated argument Eq. (21)

$v$  Rosin-Rammler exponent shown in Eq. (21)

$\mu + 1$  moment function defined by Eq. (13) circulating fluidized bed combustor limit

PFBC pressurized fluidized bed combustor relative erosion factor (Section 3.2 and Hansen [35])

O() order of magnitude operator factorial function

$9.6 \times 10^{-4}$ , etc. (see Table 1)

attended the MIT School of Chemical Engineering. Practice coatings and superalloys in high-velocity hot gases, in W.F. Adler (ed.), *Erosion: Prevention and Useful Applications*, ASTM Special Technical Publication 666, 1979.

[37] R.H. Barklow, J.A. Gobbel and F.S. Pettit, Erosion-corrosion of coatings and superalloys in high-velocity hot gases, in W.F. Adler (ed.), *Erosion: Prevention and Useful Applications*, ASTM Special Technical Publication 664, 1979.

[38] D.E. Rosner, S.A. Gobbel and R. Israel, Inertial engineering correlations of diffusional and inertial particle deposition behavior in non-isothermal forced convection environments, in R. Royer (ed.), *Fouling and Heat Exchanger Surfaces*, Eng. Foundation, New York, 1983, pp. 235-256.

[39] D.E. Rosner, Y.F. Khalil and P. Tandon, Prediction/correlation of erosion peaks and shape evolution for ceramic surfaces exposed to flows of abrasive suspensions, *Proc. 5th World Congress of Chemical Engineering*, AIChE, Vol IV, 1996, pp. 1013-1018.

[40] A.G. Konstantopoulos, M.J. Labowky and D.E. Rosner, Inertial deposition of particles from potential flows past cylinder arrays, *J. Aerosol Sci.*, 24 (2) (1993) 471-483.

[41] S.M. Wiedenbeck and D.E. Roberts, A technique to investigate high temperature erosion of refractories, *Ceramic Bulletin*, 55 (2) (1976) 185-189.

[42] M.S. Crowley, Influence of particle size on erosion resistance of refractory concrete, *Ceramic Bulletin*, 46 (7) (1969) 707-710.

[43] I.G.A. Butler, A study of erosion phenomena, Parts I and II, *Wear*, 6 (1963) 5-21 and 169-190.

[44] M.K. Liebrand, Erosion and corrosion of refractories in circulating fluidized combustors, *EPRI TR-10439*, Electric Power Research Institute, Palo Alto, CA, July 1994.

[45] D.F. Wang, J.H. She and Z.Y. Ma, Effect of microstructure on erosive wear behavior of SiC ceramics, *Wear*, 180 (1995) 35-41.

[46] M.E. Gildner, Solid-particle erosion of high-technology ceramics ( $Si_3N_4$ , glass-bonded Al<sub>2</sub>O<sub>3</sub>, and Mg<sub>2</sub>Si), in W.F. Adler (ed.), *Erosion: Prevention and Useful Applications*, ASTM Special Technical Publication 664, 1979.

[47] D.E. Rosner, P. Tandon, A.G. Konstantopoulos and M. Tasopoulos, Prediction/correlation of particle deposition rates from polydispersed flowing suspensions and the nature/properties of resulting deposits, *Proc. Int'l. Particle Technology Forum*, AIChE, Denver, CO, 1994, pp. 374-381.

[48] D.E. Rosner and P. Tandon, Rational prediction of inertially induced particle deposition rates on a cylindrical target in dust-laden streams, *Chem. Eng. Sci.*, 50 (21) (1995) 3409-3431.

[49] D.E. Rosner, P. Tandon and M.J. Labowky, Rapid estimation of cylinder erosion rates in abrasive dust-laden streams, *AIChE J.*, 41 (5) (1995) 1081-1098.

[50] M.S. Crowley, Refractory problems in coal gasification reactors, *Ceramic Bulletin*, 54 (12) (1975) 1072-1074.

[51] G.L. Friedlander, *Smoke, Dust and Haze—Fundamentals of Aerodynamics*, Wiley, New York, 1977.

[52] R. Israel and D.E. Rosner, Use of generalized Stokes number to determine the aerodynamic capture efficiency of non-Newtonian particles from compressible gas flow, *Aerosol Sci. Technol.*, 2 (1983) 43-51.

[53] F. de la Mora and D.E. Rosner, Inertial deposition of particles revisited and extended: Eulerian approach to a traditionally Lagrangian problem, *J. Physico-Chemical Hydrodynamics*, 2 (1981) 1-21.

[54] R.A. Weisel and J. Righi, Generalized correlations for inertial impaction of particles on a circular cylinder, *Aerosol Sci. Technol.*, 9 (1988) 26-60.

[55] J.S. Hansen, Relative erosion resistance of several materials, in W.F. Adler (ed.), *Erosion: Prevention and Useful Applications*, ASTM Special Technical Publication 664, 1979.

[56] W. Tabakoff, R. Kowal and A. Hamod, Erosion study of different materials affected by coal ash particles, *Wear*, 52 (1979) 161-173.

attended the MIT School of Chemical Engineering. Practice coatings and superalloys in high-velocity hot gases, in W.F. Adler (ed.), *Erosion: Prevention and Useful Applications*, ASTM Special Technical Publication 666, 1979.

[37] R.H. Barklow, J.A. Gobbel and F.S. Pettit, Erosion-corrosion of coatings and superalloys in high-velocity hot gases, in W.F. Adler (ed.), *Erosion: Prevention and Useful Applications*, ASTM Special Technical Publication 664, 1979.

[38] D.E. Rosner, S.A. Gobbel and R. Israel, Inertial engineering correlations of diffusional and inertial particle deposition behavior in non-isothermal forced convection environments, in R. Royer (ed.), *Fouling and Heat Exchanger Surfaces*, Eng. Foundation, New York, 1983, pp. 235-256.

[39] D.E. Rosner, Y.F. Khalil and P. Tandon, Prediction/correlation of erosion peaks and shape evolution for ceramic surfaces exposed to flows of abrasive suspensions, *Proc. 5th World Congress of Chemical Engineering*, AIChE, Vol IV, 1996, pp. 1013-1018.

[40] A.G. Konstantopoulos, M.J. Labowky and D.E. Rosner, Inertial deposition of particles from potential flows past cylinder arrays, *J. Aerosol Sci.*, 24 (2) (1993) 471-483.

[41] S.M. Wiedenbeck and D.E. Roberts, A technique to investigate high temperature erosion of refractories, *Ceramic Bulletin*, 55 (2) (1976) 185-189.

[42] M.S. Crowley, Influence of particle size on erosion resistance of refractory concrete, *Ceramic Bulletin*, 46 (7) (1969) 707-710.

[43] I.G.A. Butler, A study of erosion phenomena, Parts I and II, *Wear*, 6 (1963) 5-21 and 169-190.

[44] M.K. Liebrand, Erosion and corrosion of refractories in circulating fluidized combustors, *EPRI TR-10439*, Electric Power Research Institute, Palo Alto, CA, July 1994.

[45] D.F. Wang, J.H. She and Z.Y. Ma, Effect of microstructure on erosive wear behavior of SiC ceramics, *Wear*, 180 (1995) 35-41.

[46] M.E. Gildner, Solid-particle erosion of high-technology ceramics ( $Si_3N_4$ , glass-bonded Al<sub>2</sub>O<sub>3</sub>, and Mg<sub>2</sub>Si), in W.F. Adler (ed.), *Erosion: Prevention and Useful Applications*, ASTM Special Technical Publication 664, 1979.

[47] D.E. Rosner, Y.F. Khalil and P. Tandon, Prediction/correlation of erosion peaks and shape evolution for ceramic surfaces exposed to flows of abrasive suspensions, *Proc. 5th World Congress of Chemical Engineering*, AIChE, Vol IV, 1996, pp. 1013-1018.

[48] A.G. Konstantopoulos, M.J. Labowky and D.E. Rosner, Inertial deposition of particles from potential flows past cylinder arrays, *J. Aerosol Sci.*, 24 (2) (1993) 471-483.

[49] D.E. Rosner, Y.F. Khalil and P. Tandon, Prediction/correlation of erosion peaks and shape evolution for ceramic surfaces exposed to flows of abrasive suspensions, *Proc. 5th World Congress of Chemical Engineering*, AIChE, Vol IV, 1996, pp. 1013-1018.

[50] A.G. Konstantopoulos, M.J. Labowky and D.E. Rosner, Inertial deposition of particles from potential flows past cylinder arrays, *J. Aerosol Sci.*, 24 (2) (1993) 471-483.

[51] D.E. Rosner, Y.F. Khalil and P. Tandon, Prediction/correlation of erosion peaks and shape evolution for ceramic surfaces exposed to flows of abrasive suspensions, *Proc. 5th World Congress of Chemical Engineering*, AIChE, Vol IV, 1996, pp. 1013-1018.

[52] D.E. Rosner, Y.F. Khalil and P. Tandon, Prediction/correlation of erosion peaks and shape evolution for ceramic surfaces exposed to flows of abrasive suspensions, *Proc. 5th World Congress of Chemical Engineering*, AIChE, Vol IV, 1996, pp. 1013-1018.

[53] D.E. Rosner, Y.F. Khalil and P. Tandon, Prediction/correlation of erosion peaks and shape evolution for ceramic surfaces exposed to flows of abrasive suspensions, *Proc. 5th World Congress of Chemical Engineering*, AIChE, Vol IV, 1996, pp. 1013-1018.

[54] D.E. Rosner, Y.F. Khalil and P. Tandon, Prediction/correlation of erosion peaks and shape evolution for ceramic surfaces exposed to flows of abrasive suspensions, *Proc. 5th World Congress of Chemical Engineering*, AIChE, Vol IV, 1996, pp. 1013-1018.

[55] D.E. Rosner, Y.F. Khalil and P. Tandon, Prediction/correlation of erosion peaks and shape evolution for ceramic surfaces exposed to flows of abrasive suspensions, *Proc. 5th World Congress of Chemical Engineering*, AIChE, Vol IV, 1996, pp. 1013-1018.

[56] D.E. Rosner, Y.F. Khalil and P. Tandon, Prediction/correlation of erosion peaks and shape evolution for ceramic surfaces exposed to flows of abrasive suspensions, *Proc. 5th World Congress of Chemical Engineering*, AIChE, Vol IV, 1996, pp. 1013-1018.

[57] D.E. Rosner, Y.F. Khalil and P. Tandon, Prediction/correlation of erosion peaks and shape evolution for ceramic surfaces exposed to flows of abrasive suspensions, *Proc. 5th World Congress of Chemical Engineering*, AIChE, Vol IV, 1996, pp. 1013-1018.

[58] D.E. Rosner, Y.F. Khalil and P. Tandon, Prediction/correlation of erosion peaks and shape evolution for ceramic surfaces exposed to flows of abrasive suspensions, *Proc. 5th World Congress of Chemical Engineering*, AIChE, Vol IV, 1996, pp. 1013-1018.

[59] D.E. Rosner, Y.F. Khalil and P. Tandon, Prediction/correlation of erosion peaks and shape evolution for ceramic surfaces exposed to flows of abrasive suspensions, *Proc. 5th World Congress of Chemical Engineering*, AIChE, Vol IV, 1996, pp. 1013-1018.

[60] D.E. Rosner, Y.F. Khalil and P. Tandon, Prediction/correlation of erosion peaks and shape evolution for ceramic surfaces exposed to flows of abrasive suspensions, *Proc. 5th World Congress of Chemical Engineering*, AIChE, Vol IV, 1996, pp. 1013-1018.

[61] D.E. Rosner, Y.F. Khalil and P. Tandon, Prediction/correlation of erosion peaks and shape evolution for ceramic surfaces exposed to flows of abrasive suspensions, *Proc. 5th World Congress of Chemical Engineering*, AIChE, Vol IV, 1996, pp. 1013-1018.

[62] D.E. Rosner, Y.F. Khalil and P. Tandon, Prediction/correlation of erosion peaks and shape evolution for ceramic surfaces exposed to flows of abrasive suspensions, *Proc. 5th World Congress of Chemical Engineering*, AIChE, Vol IV, 1996, pp. 1013-1018.

[63] D.E. Rosner, Y.F. Khalil and P. Tandon, Prediction/correlation of erosion peaks and shape evolution for ceramic surfaces exposed to flows of abrasive suspensions, *Proc. 5th World Congress of Chemical Engineering*, AIChE, Vol IV, 1996, pp. 1013-1018.

[64] D.E. Rosner, Y.F. Khalil and P. Tandon, Prediction/correlation of erosion peaks and shape evolution for ceramic surfaces exposed to flows of abrasive suspensions, *Proc. 5th World Congress of Chemical Engineering*, AIChE, Vol IV, 1996, pp. 1013-1018.

[65] D.E. Rosner, Y.F. Khalil and P. Tandon, Prediction/correlation of erosion peaks and shape evolution for ceramic surfaces exposed to flows of abrasive suspensions, *Proc. 5th World Congress of Chemical Engineering*, AIChE, Vol IV, 1996, pp. 1013-1018.

[66] D.E. Rosner, Y.F. Khalil and P. Tandon, Prediction/correlation of erosion peaks and shape evolution for ceramic surfaces exposed to flows of abrasive suspensions, *Proc. 5th World Congress of Chemical Engineering*, AIChE, Vol IV, 1996, pp. 1013-1018.

[67] D.E. Rosner, Y.F. Khalil and P. Tandon, Prediction/correlation of erosion peaks and shape evolution for ceramic surfaces exposed to flows of abrasive suspensions, *Proc. 5th World Congress of Chemical Engineering*, AIChE, Vol IV, 1996, pp. 1013-1018.

[68] D.E. Rosner, Y.F. Khalil and P. Tandon, Prediction/correlation of erosion peaks and shape evolution for ceramic surfaces exposed to flows of abrasive suspensions, *Proc. 5th World Congress of Chemical Engineering*, AIChE, Vol IV, 1996, pp. 1013-1018.

[69] D.E. Rosner, Y.F. Khalil and P. Tandon, Prediction/correlation of erosion peaks and shape evolution for ceramic surfaces exposed to flows of abrasive suspensions, *Proc. 5th World Congress of Chemical Engineering*, AIChE, Vol IV, 1996, pp. 1013-1018.

[70] D.E. Rosner, Y.F. Khalil and P. Tandon, Prediction/correlation of erosion peaks and shape evolution for ceramic surfaces exposed to flows of abrasive suspensions, *Proc. 5th World Congress of Chemical Engineering*, AIChE, Vol IV, 1996, pp. 1013-1018.

[71] D.E. Rosner, Y.F. Khalil and P. Tandon, Prediction/correlation of erosion peaks and shape evolution for ceramic surfaces exposed to flows of abrasive suspensions, *Proc. 5th World Congress of Chemical Engineering*, AIChE, Vol IV, 1996, pp. 1013-1018.

[72] D.E. Rosner, Y.F. Khalil and P. Tandon, Prediction/correlation of erosion peaks and shape evolution for ceramic surfaces exposed to flows of abrasive suspensions, *Proc. 5th World Congress of Chemical Engineering*, AIChE, Vol IV, 1996, pp. 1013-1018.

[73] D.E. Rosner, Y.F. Khalil and P. Tandon, Prediction/correlation of erosion peaks and shape evolution for ceramic surfaces exposed to flows of abrasive suspensions, *Proc. 5th World Congress of Chemical Engineering*, AIChE, Vol IV, 1996, pp. 1013-1018.

[74] D.E. Rosner, Y.F. Khalil and P. Tandon, Prediction/correlation of erosion peaks and shape evolution for ceramic surfaces exposed to flows of abrasive suspensions, *Proc. 5th World Congress of Chemical Engineering*, AIChE, Vol IV, 1996, pp. 1013-1018.

[75] D.E. Rosner, Y.F. Khalil and P. Tandon, Prediction/correlation of erosion peaks and shape evolution for ceramic surfaces exposed to flows of abrasive suspensions, *Proc. 5th World Congress of Chemical Engineering*, AIChE, Vol IV, 1996, pp. 1013-1018.

[76] D.E. Rosner, Y.F. Khalil and P. Tandon, Prediction/correlation of erosion peaks and shape evolution for ceramic surfaces exposed to flows of abrasive suspensions, *Proc. 5th World Congress of Chemical Engineering*, AIChE, Vol IV, 1996, pp. 1013-1018.

[77] D.E. Rosner, Y.F. Khalil and P. Tandon, Prediction/correlation of erosion peaks and shape evolution for ceramic surfaces exposed to flows of abrasive suspensions, *Proc. 5th World Congress of Chemical Engineering*, AIChE, Vol IV, 1996, pp. 1013-1018.

[78] D.E. Rosner, Y.F. Khalil and P. Tandon, Prediction/correlation of erosion peaks and shape evolution for ceramic surfaces exposed to flows of abrasive suspensions, *Proc. 5th World Congress of Chemical Engineering*, AIChE, Vol IV, 1996, pp. 1013-1018.

[79] D.E. Rosner, Y.F. Khalil and P. Tandon, Prediction/correlation of erosion peaks and shape evolution for ceramic surfaces exposed to flows of abrasive suspensions, *Proc. 5th World Congress of Chemical Engineering*, AIChE, Vol IV, 1996, pp. 1013-1018.

[80] D.E. Rosner, Y.F. Khalil and P. Tandon, Prediction/correlation of erosion peaks and shape evolution for ceramic surfaces exposed to flows of abrasive suspensions, *Proc. 5th World Congress of Chemical Engineering*, AIChE, Vol IV, 1996, pp. 1013-1018.

[81] D.E. Rosner, Y.F. Khalil and P. Tandon, Prediction/correlation of erosion peaks and shape evolution for ceramic surfaces exposed to flows of abrasive suspensions, *Proc. 5th World Congress of Chemical Engineering*, AIChE, Vol IV, 1996, pp. 1013-1018.

[82] D.E. Rosner, Y.F. Khalil and P. Tandon, Prediction/correlation of erosion peaks and shape evolution for ceramic surfaces exposed to flows of abrasive suspensions, *Proc. 5th World Congress of Chemical Engineering*, AIChE, Vol IV, 1996, pp. 1013-1018.

[83] D.E. Rosner, Y.F. Khalil and P. Tandon, Prediction/correlation of erosion peaks and shape evolution for ceramic surfaces exposed to flows of abrasive suspensions, *Proc. 5th World Congress of Chemical Engineering*, AIChE, Vol IV, 1996, pp. 1013-1018.

[84] D.E. Rosner, Y.F. Khalil and P. Tandon, Prediction/correlation of erosion peaks and shape evolution for ceramic surfaces exposed to flows of abrasive suspensions, *Proc. 5th World Congress of Chemical Engineering*, AIChE, Vol IV, 1996, pp. 1013-1018.

[85] D.E. Rosner, Y.F. Khalil and P. Tandon, Prediction/correlation of erosion peaks and shape evolution for ceramic surfaces exposed to flows of abrasive suspensions, *Proc. 5th World Congress of Chemical Engineering*, AIChE, Vol IV, 1996, pp. 1013-1018.

[86] D.E. Rosner, Y.F. Khalil and P. Tandon, Prediction/correlation of erosion peaks and shape evolution for ceramic surfaces exposed to flows of abrasive suspensions, *Proc. 5th World Congress of Chemical Engineering*, AIChE, Vol IV, 1996, pp. 1013-1018.

[87] D.E. Rosner, Y.F. Khalil and P. Tandon, Prediction/correlation of erosion peaks and shape evolution for ceramic surfaces exposed to flows of abrasive suspensions, *Proc. 5th World Congress of Chemical Engineering*, AIChE, Vol IV, 1996, pp. 1013-1018.

[88] D.E. Rosner, Y.F. Khalil and P. Tandon, Prediction/correlation of erosion peaks and shape evolution for ceramic surfaces exposed to flows of abrasive suspensions, *Proc. 5th World Congress of Chemical Engineering*, AIChE, Vol IV, 1996, pp. 1013-1018.

[89] D.E. Rosner, Y.F. Khalil and P. Tandon, Prediction/correlation of erosion peaks and shape evolution for ceramic surfaces exposed to flows of abrasive suspensions, *Proc. 5th World Congress of Chemical Engineering*, AIChE, Vol IV, 1996, pp. 1013-1018.

[90] D.E. Rosner, Y.F. Khalil and P. Tandon, Prediction/correlation of erosion peaks and shape evolution for ceramic surfaces exposed to flows of abrasive suspensions, *Proc. 5th World Congress of Chemical Engineering*, AIChE, Vol IV, 1996, pp. 1013-1018.

[91] D.E. Rosner, Y.F. Khalil and P. Tandon, Prediction/correlation of erosion peaks and shape evolution for ceramic surfaces exposed to flows of abrasive suspensions, *Proc. 5th World Congress of Chemical Engineering*, AIChE, Vol IV, 1996, pp. 1013-1018.

[92] D.E. Rosner, Y.F. Khalil and P. Tandon, Prediction/correlation of erosion peaks and shape evolution for ceramic surfaces exposed to flows of abrasive suspensions, *Proc. 5th World Congress of Chemical Engineering*, AIChE, Vol IV, 1996, pp. 1013-1018.

[93] D.E. Rosner, Y.F. Khalil and P. Tandon, Prediction/correlation of erosion peaks and shape evolution for ceramic surfaces exposed to flows of abrasive suspensions, *Proc. 5th World Congress of Chemical Engineering*, AIChE, Vol IV, 1996, pp. 1013-1018.

[94] D.E. Rosner, Y.F. Khalil and P. Tandon, Prediction/correlation of erosion peaks and shape evolution for ceramic surfaces exposed to flows of abrasive suspensions, *Proc. 5th World Congress of Chemical Engineering*, AIChE, Vol IV, 1996, pp. 1013-1018.

[95] D.E. Rosner, Y.F. Khalil and P. Tandon, Prediction/correlation of erosion peaks and shape evolution for ceramic surfaces exposed to flows of abrasive suspensions, *Proc. 5th World Congress of Chemical Engineering*, AIChE, Vol IV, 1996, pp. 1013-1018.

[96] D.E. Rosner, Y.F. Khalil and P. Tandon, Prediction/correlation of erosion peaks and shape evolution for ceramic surfaces exposed to flows of abrasive suspensions, *Proc. 5th World Congress of Chemical Engineering*, AIChE, Vol IV, 1996, pp. 1013-1018.

[97] D.E. Rosner, Y.F. Khalil and P. Tandon, Prediction/correlation of erosion peaks and shape evolution for ceramic surfaces exposed to flows of abrasive suspensions, *Proc. 5th World Congress of Chemical Engineering*, AIChE, Vol IV, 1996, pp. 1013-1018.

[98] D.E. Rosner, Y.F. Khalil and P. Tandon, Prediction/correlation of erosion peaks and shape evolution for ceramic surfaces exposed to flows of abrasive suspensions, *Proc. 5th World Congress of Chemical Engineering*, AIChE, Vol IV, 1996, pp. 1013-1018.

[99] D.E. Rosner, Y.F. Khalil and P. Tandon, Prediction/correlation of erosion peaks and shape evolution for ceramic surfaces exposed to flows of abrasive suspensions, *Proc. 5th World Congress of Chemical Engineering*, AIChE, Vol IV, 1996, pp. 1013-1018.

[100] D.E. Rosner, Y.F. Khalil and P. Tandon, Prediction/correlation of erosion peaks and shape evolution for ceramic surfaces exposed to flows of abrasive suspensions, *Proc. 5th World Congress of Chemical Engineering*, AIChE, Vol IV, 1996, pp. 1013-1018.

[101] D.E. Rosner, Y.F. Khalil and P. Tandon, Prediction/correlation of erosion peaks and shape evolution for ceramic surfaces exposed to flows of abrasive suspensions, *Proc. 5th World Congress of Chemical Engineering*, AIChE, Vol IV, 1996, pp. 1013-1018.

[102] D.E. Rosner, Y.F. Khalil and P. Tandon, Prediction/correlation of erosion peaks and shape evolution for ceramic surfaces exposed to flows of abrasive suspensions, *Proc. 5th World Congress of Chemical Engineering*, AIChE, Vol IV, 1996, pp. 1013-1018.

[103] D.E. Rosner, Y.F. Khalil and P. Tandon, Prediction/correlation of erosion peaks and shape evolution for ceramic surfaces exposed to flows of abrasive suspensions, *Proc. 5th World Congress of Chemical Engineering*, AIChE, Vol IV, 1996, pp. 1013-1018.

[104] D.E. Rosner, Y.F. Khalil and P. Tandon, Prediction/correlation of erosion peaks and shape evolution for ceramic surfaces exposed to flows of abrasive suspensions, *Proc. 5th World Congress of Chemical Engineering*, AIChE, Vol IV, 1996, pp. 1013-1018.

[105] D.E. Rosner, Y.F. Khalil and P. Tandon, Prediction/correlation of erosion peaks and shape evolution for ceramic surfaces exposed to flows of abrasive suspensions, *Proc. 5th World Congress of Chemical Engineering*, AIChE, Vol IV, 1996, pp. 1013-1018.

[106] D.E. Rosner, Y.F. Khalil and P. Tandon, Prediction/correlation of erosion peaks and shape evolution for ceramic surfaces exposed to flows of abrasive suspensions, *Proc. 5th World Congress of Chemical Engineering*, AIChE, Vol IV, 1996, pp. 1013-1018.

[107] D.E. Rosner, Y.F. Khalil and P. Tandon, Prediction/correlation of erosion peaks and shape evolution for ceramic surfaces exposed to flows of abrasive suspensions, *Proc. 5th World Congress of Chemical Engineering*, AIChE, Vol IV, 1996, pp. 1013-1018.

[108] D.E. Rosner, Y.F. Khalil and P. Tandon, Prediction/correlation of erosion peaks and shape evolution for ceramic surfaces exposed to flows of abrasive suspensions, *Proc. 5th World Congress of Chemical Engineering*, AIChE, Vol IV, 1996, pp. 1013-1018.

[109] D.E. Rosner, Y.F. Khalil and P. Tandon, Prediction/correlation of erosion peaks and shape evolution for ceramic surfaces exposed to flows of abrasive suspensions, *Proc. 5th World Congress of Chemical Engineering*, AIChE, Vol IV, 1996, pp. 1013-1018.

[110] D.E. Rosner, Y.F. Khalil and P. Tandon, Prediction/correlation of erosion peaks and shape evolution for ceramic surfaces exposed to flows of abrasive suspensions, *Proc. 5th World Congress of Chemical Engineering*, AIChE, Vol IV, 1996, pp. 1013-1018.

[111] D.E. Rosner, Y.F. Khalil and P. Tandon, Prediction/correlation of erosion peaks and shape evolution for ceramic surfaces exposed to flows of abrasive suspensions, *Proc. 5th World Congress of Chemical Engineering*, AIChE, Vol IV, 1996, pp. 1013-1018.

[112] D.E. Rosner, Y.F. Khalil and P. Tandon, Prediction/correlation of erosion peaks and shape evolution for ceramic surfaces exposed to flows of abrasive suspensions, *Proc. 5th World Congress of Chemical Engineering*, AIChE, Vol IV, 1996, pp. 1013-1018.

[113] D.E. Rosner, Y.F. Khalil and P. Tandon, Prediction/correlation of erosion peaks and shape evolution for ceramic surfaces exposed to flows of abrasive suspensions, *Proc. 5th World Congress of Chemical Engineering*, AIChE, Vol IV, 1996, pp. 1013-1018.

[114] D.E. Rosner, Y.F. Khalil and P. Tandon, Prediction/correlation of erosion peaks and shape evolution for ceramic surfaces exposed to flows of abrasive suspensions, *Proc. 5th World Congress of Chemical Engineering*, AIChE, Vol IV, 1996, pp. 1013-1018.

[115] D.E. Rosner, Y.F. Khalil and P. Tandon, Prediction/correlation of erosion peaks and shape evolution for ceramic surfaces exposed to flows of abrasive suspensions, *Proc. 5th World Congress of Chemical Engineering*, AIChE, Vol IV, 1996, pp. 1013-1018.

[116] D.E. Rosner, Y.F. Khalil and P. Tandon, Prediction/correlation of erosion peaks and shape evolution for ceramic surfaces exposed to flows of abrasive suspensions, *Proc. 5th World Congress of Chemical Engineering*, AIChE, Vol IV, 1996, pp. 1013-1018.

[117] D.E. Rosner, Y.F. Khalil and P. Tandon, Prediction/correlation of erosion peaks and shape evolution for ceramic surfaces exposed to flows of abrasive suspensions, *Proc. 5th World Congress of Chemical Engineering*, AIChE, Vol IV, 1996, pp. 1013-1018.

[118] D.E. Rosner, Y.F. Khalil and P. Tandon, Prediction/correlation of erosion peaks and shape evolution for ceramic surfaces exposed to flows of abrasive suspensions, *Proc. 5th World Congress of Chemical Engineering*, AIChE, Vol IV, 1996, pp. 1013-1018.

[119] D.E. Rosner, Y.F. Khalil and P. Tandon, Prediction/correlation of erosion peaks and shape evolution for ceramic surfaces exposed to flows of abrasive suspensions, *Proc. 5th World Congress of Chemical Engineering*, AIChE, Vol IV, 1996, pp. 1013-1018.

[120] D.E. Rosner, Y.F. Khalil and P. Tandon, Prediction/correlation of erosion peaks and shape evolution for ceramic surfaces exposed to flows of abrasive suspensions, *Proc. 5th World Congress of Chemical Engineering*, AIChE, Vol IV, 1996, pp. 1013-1018.

[121] D.E. Rosner, Y.F. Khalil and P. Tandon, Prediction/correlation of erosion peaks and shape evolution for ceramic surfaces exposed to flows of abrasive suspensions, *Proc. 5th World Congress of Chemical Engineering*, AIChE, Vol IV, 1996, pp. 1013-1018.

[122] D.E. Rosner, Y.F. Khalil and P. Tandon, Prediction/correlation of erosion peaks and shape evolution for ceramic surfaces exposed to flows of abrasive suspensions, *Proc. 5th World Congress of Chemical Engineering*, AIChE, Vol IV, 1996, pp. 1013-1018.

[123] D.E. Rosner, Y.F. Khalil and P. Tandon, Prediction/correlation of erosion peaks and shape evolution for ceramic surfaces exposed to flows of abrasive suspensions, *Proc. 5th World Congress of Chemical Engineering*, AIChE, Vol IV, 1996, pp. 1013-1018.

[124] D.E. Rosner, Y.F. Khalil and P. Tandon, Prediction/correlation of erosion peaks and shape evolution for ceramic surfaces exposed to flows of abrasive suspensions, *Proc. 5th World Congress of Chemical Engineering*, AIChE, Vol IV, 1996, pp. 1013-1018.

[125] D.E. Rosner, Y.F. Khalil and P. Tandon, Prediction/correlation of erosion peaks and shape evolution for ceramic surfaces exposed to flows of abrasive suspensions, *Proc. 5th World Congress of Chemical Engineering*, AIChE, Vol IV